

DASA 2426

PIFR-106-2

RPN 43

DYNAMIC EFFECTS OF HIGH ν/γ BEAM PLASMA INTERACTIONS

August 1969

by

Gerold Yonas, Philip Spence,
Bruce Ecker, and John Rander

Prepared for

Defense Atomic Support Agency
Washington, D. C. 20305

This research was sponsored by
the Defense Atomic Support Agency

under Contract
DASA-01-68-C-0096

Physics International Company
2700 Merced Street
San Leandro, California 94577

This research has been sponsored by
the Defense Atomic Support Agency
under NWER Subtask LA013
Contract DASA 01-68-C-0096.

ABSTRACT

Generation and propagation characteristics of high v/γ electron streams have been investigated using diode voltage and current diagnostics, net and primary beam current monitors, graphite calorimeters and thin foil depth dosimeters, and scintillator-photodiode detectors. The effects of beam-plasma interactions of the time and spatial dependence of beam current have been measured and correlated with a diffusion dominated model of current neutralization. Important parameters in this model are primary current risetime, avalanche breakdown time of the background gas, and the plasma conductivity after breakdown. The existence of large primary electron transverse energy components was consistent with a magnetic pressure balance calculation indicating a dependence on $(v/\gamma)_{\text{net}}$ and the degree of current neutralization. Beam energy loss mechanisms are discussed and compared with observed beam energy loss. Results of this work indicate that efficient propagation, guiding, and control of high v/γ beams can be accomplished only over relatively short distances, less than one meter, even at optimum transport pressures. Suggestions for more efficient beam propagation are pre-ionization of the background gas and the use of trapped magnetic fields to contain the beam. Preliminary experiments investigating production of energetic ions by the beam-plasma interaction, and demonstrating the feasibility of multiple cathode geometries, are also reported.

FOREWORD

This report summarizes high v/γ beam research carried out from February 1968 to August 1969. This program was funded by the Defense Atomic Support Agency under Contract DASA-01-68-C-0096 which supported the work from February to August 1968 and from November 1968 to August 1969. Project monitors were Lt. J. M. Wachtel and, after June 1969, Major S. V. Gates. Work from the initial phases of the program is discussed in detail in reports DASA 2175 and DASA 2296. The work for this phase of the program was conducted in Physics International's Nuclear Radiation Effects Department (under the supervision of Dr. Alan Klein) by members of the Intense Beams and Applications Group (managed by Dr. Gerold Yonas). Principal investigators were Dr. Gerold Yonas, project manager; Dr. Philip Spence, project physicist and co-manager; Bruce Ecker, Donald Pellinen, and John Rander, project physicists.

We acknowledge the assistance of Sidney Putnam, who participated in helpful discussions throughout the course of the program. We also would like to thank Ian Smith and Charles Martin, AWRE, for suggestions in regard to multiple cathode geometries and to Professor Darrell Drickey, UCLA, for his participation in the ion detection experiment.

CONTENTS

	<u>Page</u>
I. INTRODUCTION	1
II. EXPERIMENTAL FACILITY AND DIAGNOSTICS	5
III. BEAM BEHAVIOR	9
A. Current Neutralization, Breakdown, and Plasma Conductivity	9
B. Radial Structure of Net Current and Magnetic Diffusion	20
C. Relation of Net Current to Beam Transverse Energy Components	25
D. Beam Energy Loss	40
E. New Data and Interpretation	58
IV. ION ACCELERATION STUDY	73
A. General Discussion	73
B. Experimental Arrangement	74
C. Results and Comments	77
V. MULTIPLE CATHODE FEASIBILITY STUDY	81
VI. CONCLUSION	89
REFERENCES	93
DISTRIBUTION	95

ILLUSTRATIONS

<u>Figure</u>		<u>Page</u>
1	Diode and Drift Chamber Region with Diagnostics	6
2	Primary, Plasma, and Net Current Waveforms	13
3	Air Breakdown Data	14
4	Argon Breakdown Data	15
5	Helium Breakdown Data	16
6	Net Current Decay Time Versus Pressure in Air	18
7	Schematic Radial Structure of Primary, Plasma, and Net Current Densities	21
8	Azimuthal Magnetic Field Versus Radius for Current Configuration of Figure 7 C	23
9	Calculated and Measured Electron Deposition Profiles in Aluminum, Mean Electron Energy = 234 keV	33
10	Calculated and Measured Electron Deposition Profiles in Aluminum, Mean Electron Energy = 479 keV	34
11	Beam Time of Flight Data	35
12	Electron Number Deposition in Aluminum	36
13	Electron Transmission Data in Aluminum, $\langle E \rangle \approx 250$ keV	38
14	Total Calories Versus Path Length in 1-1/4-in. Pipe (0.5 and 0.3 Torr ~ 350 keV)	47
15	Total Calories Versus Path Length in 1-1/4-in. Pipe (0.75 and 1.0 Torr ~ 250 keV)	48
16	Primary Electron Beam Current Waveforms Measured with Faraday Cup 14 cm from Anode	51

<u>Figure</u>		<u>Page</u>
17	I_{net} Versus Time at Various Distances in 1-1/4-in. Guide Pipe 0.5 Torr, $\langle E \rangle = 321$ keV Simultaneously Monitored Waveforms	52
18	I_{net} Versus Time at Various Distances in 1-1/4-in. Guide Pipe 0.5 Torr, $\langle E \rangle = 266$ keV Simultaneously Monitored Waveforms	53
19	I_{net} Versus Time at Various Distances in 1-1/4-in. Guide Pipe 0.5 Torr, $\langle E \rangle = 221$ keV Simultaneously Monitored Waveforms	54
20	I_{net} Versus Time at Various Distances in 1-1/4-in. Guide Pipe 1.0 Torr, $\langle E \rangle = 243$ keV Simultaneously Monitored Waveforms	55
21	I_{net} Versus Time at Various Distances in 1-1/4-in. Guide Pipe 1.85 Torr, $\langle E \rangle = 217$ keV Simultaneously Monitored Waveforms	56
22	Net and Primary Current Waveforms	59
23	Net and Primary Current Waveforms	61
24	Breakdown Data at Different Lengths 0.75 Torr	62
25	Beam Front Distance Versus Time, 0.31 Torr	64
26	Beam Front Distance Versus Time, 0.5 Torr	64
27	Beam Front Distance Versus Time, 0.755 Torr	65
28	Beam Front Distance Versus Time, 1.0 Torr	65
29	Beam Front Distance Versus Time	66
30	Beam Front Distance Versus Time	67
31	Beam Front Distance Versus Time	68
32	Beam Front Distance Versus Time	69
33	Primary Electron Beam Current Waveform, 120 kA/cm, 20 nsec/cm	76

ILLUSTRATIONS (cont.)

<u>Figure</u>		<u>Page</u>
34	Open-Shutter Photograph of Electron Beam Entering Ion Detection Apparatus	76
35	Positive Ion Current Waveforms	78
36	Multiple Cathode Configuration	83
37	Multiple Cathodes and Anode Holder with Magnetic Isolation	84
38	Anode Used with Multiple Cathodes	86
39	Open-Shutter Photograph of Seven Converging Beams	87

SECTION I

INTRODUCTION

Possibilities for using high current pulsed electron accelerators have increased dramatically in the past two years with applications including bremsstrahlung production, high energy density material response studies, plasma heating, and ion acceleration. Since utilizing the full range of pulser capabilities requires understanding the fundamental physical principles which underlie beam generation and propagation processes, DASA has supported experimental and analytical research into high v/γ diode behavior and beam-plasma interactions which has been carried out at Physics International over the last 18 months. Relevant parameters in our study have included beam energy and current, drift chamber geometry and dimensions, and background gas constituents and pressure. This work has increased understanding of the critical phenomena pertinent to high v/γ beams and has led to the evolution of an operational facility using fully diagnosed beams of $v/\gamma \sim 10$ on a routine basis. Results have been presented in two complete and fully documented DASA reports (References 1 and 2), and also in four papers: JOWOG VI Conference Albuquerque, N. M., January 1969; Conference on Relativistic Electron Beams, Cornell University, Ithaca, N. Y., January 1969; DASA Simulation Meeting, April, 1969; and the 10th Symposium on Electron, Ion, & Laser Beam Technology, May, 1969. Techniques and diagnostics developed under DASA support have also been described in several reports in support of programs for DASA, other defense agencies, and their contractors, namely: DASA 01-69-C-0065, Air Force F 29601-68-C008 and AF04 (694)-901, Army Subcontract 601936, AEC Subcontracts 20-6202, 18-115, 18-1738, and 16-8515, and programs for other contractors including AVCO, G. E., Philco-Ford, McDonnell-Douglas, and TRW.

Major accomplishments of the DASA work are:

1. Generation, diagnosis, propagation, and control of beams with $(v/\gamma) \sim 10$
 - a. Development of a cathode-anode configuration and operational techniques to provide reproducible and efficient high v/γ operation
 - b. Development and use of subnanosecond diagnostics to measure accelerating voltage, diode current, net and primary beam currents
 - c. Shaping and guiding of beams to provide reproducible ultra high, uniform fluences over several square cm--an essential requirement in material response experiments
2. Investigations into the fundamental energy loss mechanisms, and factors affecting efficient and stable propagation of high v/γ beams
 - a. Documentation of the essential nature of current neutralization and the development of a dynamic model to explain the features of this process
 - b. Measurements of beam transverse energy and development of models to explain its role in propagation and energy deposition
 - c. Investigations of propagation characteristics of beams in air, argon, and helium, and determination of fundamental properties of background gases that govern beam behavior
3. Demonstrations of techniques for manipulation of such beams using image currents in conductors
 - a. Propagation of beams through arbitrary paths through the use of curved conducting guide pipes
 - b. Beam splitting and combining using divided guides

4. Detection of energetic ions produced by the beam-plasma interaction in helium and air.

This report will briefly summarize and in some areas clarify results of work already reported, and present work completed since the writing of PITR-106-1. Current neutralization, energetic ion detection, and multiple cathode studies are described in Sections III, IV, and V, respectively.

The most important conclusions of PITR-106-1 relate to the extent and time dependence of current neutralization and the role of this process in beam propagation. Experimental results concern beams of primary beam current, I_{pr} , which exceeds 200,000 A at mean electron energies of 200 keV ($v/\gamma \sim 10$). Based on the primary electron beam current, beams with values of $(v/\gamma)_{pr} > 1$, can propagate; but only if current neutralization (a result of back streaming plasma electron current, I_{pl}) can occur such that

$$(v/\gamma)_{net} = \frac{(\dot{I}_{pr} + \dot{I}_{pl})/Z}{17,000 \beta \gamma} \leq 1 \quad (1)$$

For such beams $(v/\gamma)_{net}$ is approximately equal to 1.0 and can exceed 1.0 over short distances. Interpreting such a beam in terms of a plasma stream yields the prediction that for $v/\gamma \approx 1$, the kinetic energy of the primary electrons would be partitioned equally between longitudinal and transverse modes. Three independent measurements are reported that demonstrate this effect.

The next section discusses the experimental facility and diagnostics used in the beam studies.

SECTION II

EXPERIMENTAL FACILITY AND DIAGNOSTICS

Although detailed description of the design, calibration, and use of the 730 Pulserad has already been presented (References 1,2), a brief summary is given here for clarity.

The Pulser (Figure 1) consists of a Marx generator used to pulse-charge an 8.5- Ω , oil-filled coax which is switched into a field emission diode load. The load impedance is variable in the 1- to 9- Ω range by adjusting the gap between a 2-1/2 in. diameter, 600-needle cathode, and a 0.00025-in. aluminized Mylar transmission anode. Typical operation at pulse charge voltages of 3.5 MV yields beams with mean electron energies from 180 keV to 1 MeV, at mean current levels of 200 kA and 100 kA respectively, and with a 50-nsec pulse duration (FWHM).

Considerable emphasis has been placed on developing low-inductance diode drift chamber diagnostics. Diode accelerating voltage and current probes, as well as net and primary current probes, have been used to instrument the pulser. A resistive voltage divider, consisting of a capacitively and resistively graded column of copper sulfate solution, was used to monitor the cathode voltage directly, and the diode current was monitored by a self-integrating magnetic fluxmeter. Calibration was performed under machine operating conditions by comparing the monitor output to the current measured in a Faraday cup placed at the anode. The electron energy deposition-versus-depth profile was calculated from voltage and current data with a Monte Carlo electron transport code. These calculations were compared with measurements of dose versus depth profile in a stack of thin foil calorimeters. In addition, totally absorbing carbon calorimetry measured transported beam energy and fluence distributions.

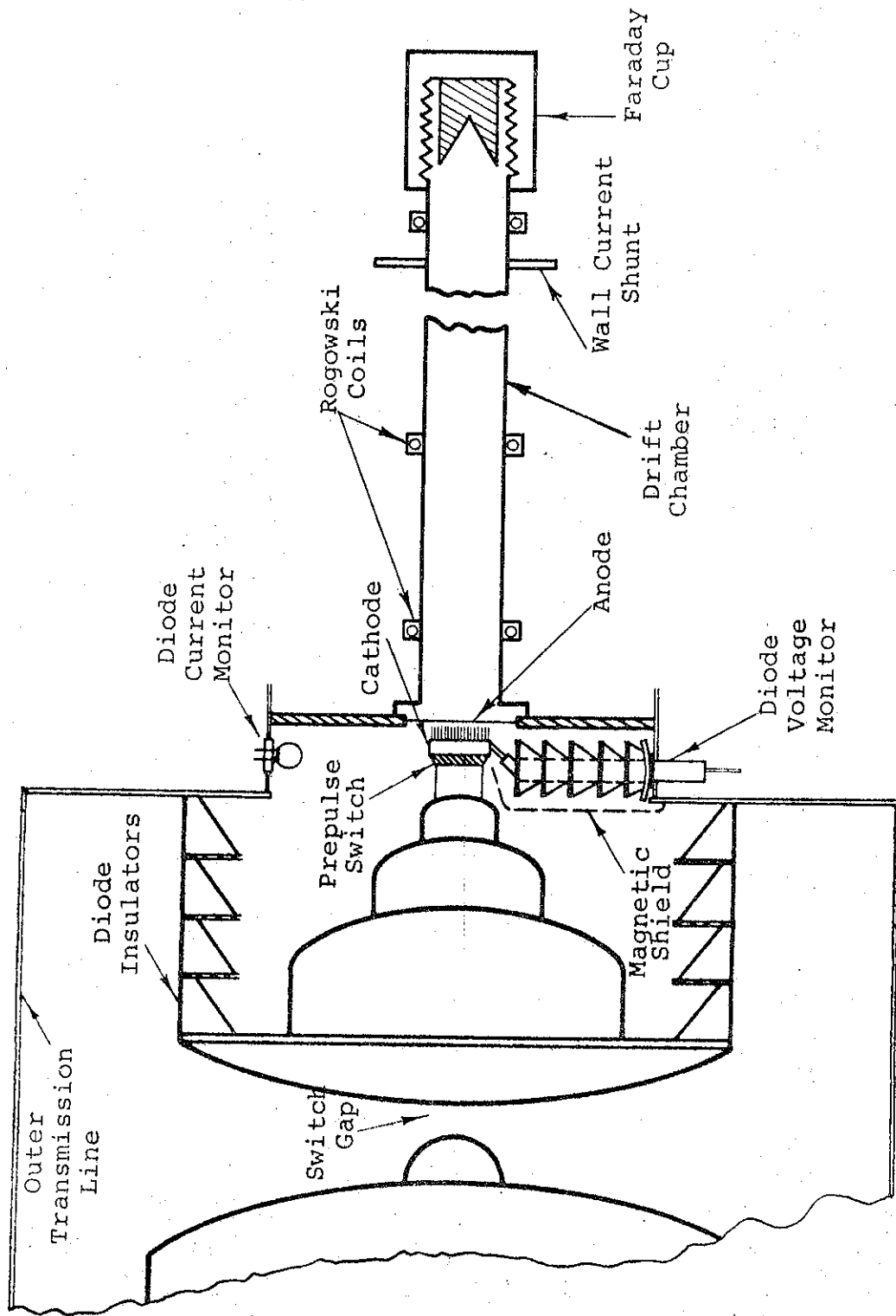


FIGURE 1. DIODE AND DRIFT CHAMBER REGION WITH DIAGNOSTICS

Rogowski coils and low-inductance wall current shunts measured the net current flowing through the area enclosed by the guide pipe, typically 1-1/4-in. diameter. Time dependence of the primary current at the end of the drift region was measured with a Faraday cup designed specifically to collect low-energy, high-current electron beams. Electron beam time-of-flight measurements were made using both the Rogowski coils and a scintillator-photodiode combination to detect the bremsstrahlung produced in thin tantalum foils at various distances from the anode. Oscillations inherent in the voltage and current waveforms produced oscillations in the bremsstrahlung output, allowing arrival time measurements for various portions of the beam pulse.

The apparatus used in ion detection experiments will be discussed for the first time in Section IV, with the results of other experiments performed since the last report. The next section will expand previous comments on current neutralization and beam transverse energy.

SECTION III

BEAM BEHAVIOR

A. CURRENT NEUTRALIZATION, BREAKDOWN, AND PLASMA CONDUCTIVITY

The importance of current neutralization in describing high v/γ electron beams has been confirmed by experimental measurement of primary and net current waveforms (Reference 2). Many papers discuss relativistic electron beam transport, but only a few consider current neutralization. Table I presents a list of electron beam models representing various theoretical descriptions, and a model based on the experimental observations of this work. Basic elements of the present model include Creedon's ideas about background gas breakdown (Reference 3), Zwick's suggestion of the importance of magnetic diffusion (Reference 4), and a magnetic pressure balance relation resulting in the containment of large transverse energy components in the beam.

When the beam is injected into the drift region, an azimuthal magnetic field and a longitudinal electric field are generated by the rising current, and a radial electric field is generated by the space charge. The first process to occur is ionization of the background gas. Consideration of collisional ionization and creation of ions by the intense electric fields at the beam front yields the following expression for the secondary electron density, n , (Reference 3)

$$\frac{dn}{dt} = (v_i - v_a) n + Kj + \nabla \cdot \Gamma$$

where v_i and v_a are the ionization and attachment frequencies, Γ is the particle flow,

$$K = \frac{N\sigma_h}{q}, \quad N = \text{gas number density}$$

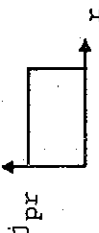
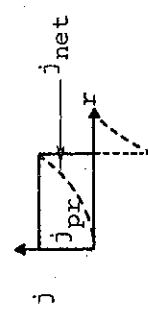

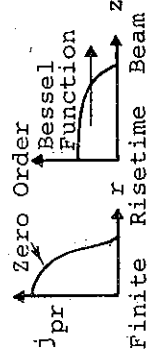
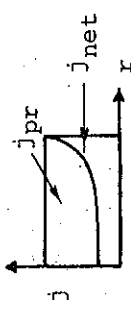
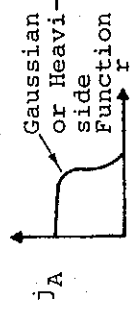
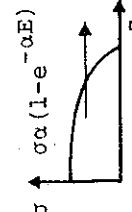
σ_h = collisional ionization cross section

and q = electron charge

TABLE I

RELATIVISTIC ELECTRON BEAM MODELS

ASSUMPTIONS

Author	Space Charge Neutralization	Current Neutralization	Radial Dependence of Current	Plasma Conductivity	Comments
Lawson Ref. 5 (1956)	Yes; f_e variable from 0 to 1	No; $f_m = 0$			Steady state trajectory model. Valid for $v/\gamma \ll 1$.
Creedon Ref. 3 (1967)	$f_e=0$ to 1 from primary collisions and avalanche processes	Yes, after gas breakdown			Discussion of beam-induced breakdown of background gas.
Zwick Ref. 4 (1967)	Rapid neutralization to $f_e = 1$	Yes		$\sigma = \text{Constant}$	Time dependent calculation (no boundary conditions) of magnetic diffusion and radial dependence of I_{net} .
Rostoker Ref. 6 (1968)	Charge neutralization dependent only on collisional processes	No		$\sigma = \text{Constant}$	Self-consistent equilibrium solution for primary current flow restricted to a hollow cylindrical sheath.
Putnam Ref. 7 (1969)	$f_e(t)$ depending on ionization rate	Yes		$\sigma = \text{Constant}$	Calculation of EM fields in the beam channel for cylindrical metallic guide boundary condition.
Yonas, et al. (1969)	Rapid neutralization to $f_e = 1$	Yes, after gas breakdown		$\sigma=0$ $t < \text{breakdown}$ $\sigma=\text{Constant}$ after breakdown	Empirical model to explain observed net current wave forms, including magnetic diffusion.
Putnam Ref. 8 (1969)	$f_e(t)$ dependent on ionization rate	Yes		$\sigma \propto (1-e^{-\alpha E})$	Calculation of EM fields. Finite cylindrical guide with end plates. Finite rise and decay of beam current.

If one assumes that the avalanche term $(v_i - v_a) n$ is small compared to the collisional ionization term for times less than the charge neutralization time t_e (justified because of the rapid loss of mobile secondary electrons from the beam channel which continues until the space charge fields are neutralized), we find the following values of t_e (Reference 8):

TABLE II
SPACE CHARGE NEUTRALIZATION TIMES

Pressure (Torr)	t_e (nsec)
0.1	12.0
0.3	4.0
0.5	2.4

$$j_{pr} = 1.6 \times 10^4 \text{ amp/cm}^2$$

$$t_r = 20 \text{ nsec}$$

$$\gamma = 1.5$$

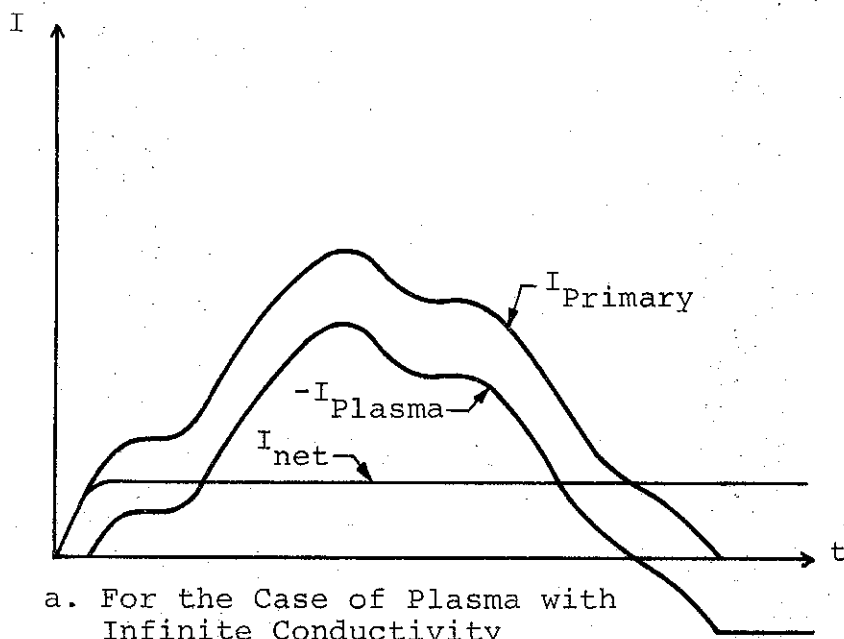
$$E_z = 10^3 \text{ V/cm}$$

$$\sigma_h = 2.62 \times 10^{-18} \text{ cm}^2$$

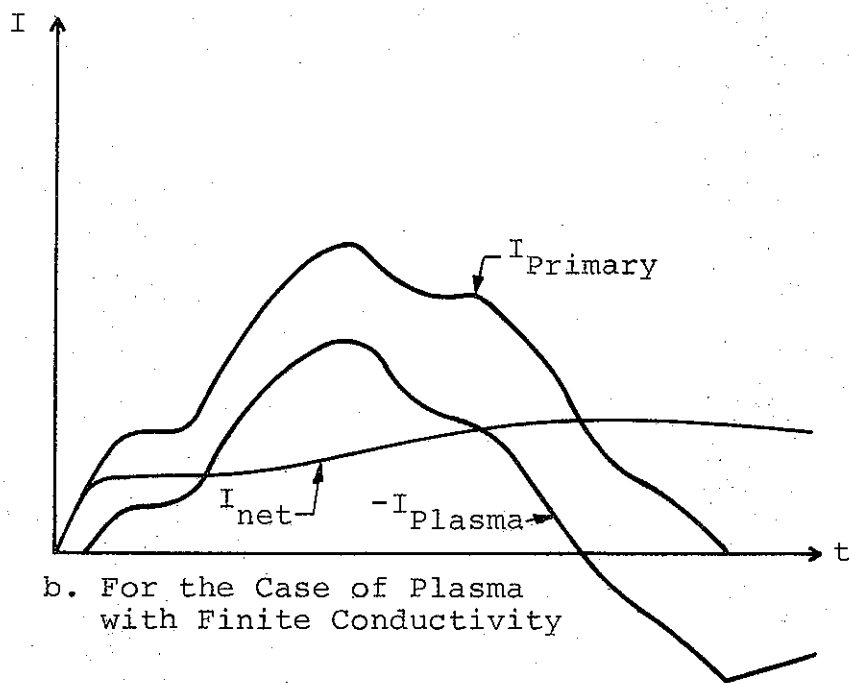
These calculations must be considered upper estimates of charge neutralization times since other ionization mechanisms would serve to enhance the buildup of ionization. Prior to space charge neutralization the radial electric forces dominate and the beam front expands rapidly. After charge neutralization, magnetic forces are dominant and subsequent beam behavior is determined by the degree of current neutralization. However, a time delay, t_b , is required for buildup of a secondary electron density high enough to produce substantial current neutralization. This time

delay can be interpreted as the breakdown time of the background gas in a longitudinal electric field. As a first approximation, any increase in primary current after breakdown is cancelled completely by the induced back-streaming secondary current and the net current remains equal to the value of the primary current at breakdown (see Figure 2a). In reality, though, the plasma conductivity is finite and the plasma current diffuses out of the beam channel, resulting in an increase of the net current throughout the duration of the beam pulse, and an exponential decay of I_{net} for times longer than the beam pulse duration (Figure 2b).

Extensive net current data generated during the present program substantially confirms this qualitative picture of breakdown and current neutralization. Figures 3 to 5 present experimental measurements of breakdown time and longitudinal electric field [$E_z \equiv 10^{-7} dI/dt$ (mks)] ~ 10 cm from the anode and compare the results to those of Felsenthal and Proud (Reference 9). The breakdown time was defined as the time when the net current abruptly ceased its sharp increase while the primary current continued to rise. Recently S. Putnam has suggested that this measured breakdown time is the sum of t_e and t_b , if one assumes that beam propagation can occur before charge neutralization is achieved, Reference 10. The truth lies somewhere between these two extremes, i.e., a small degree of beam propagation can occur before $t = t_e$ and the breakdown process depends on both the primary ionization rate and avalanche rate such that a direct comparison with pulsed-dc breakdown (avalanche) is not strictly justified. However, agreement of the data in Figures 3 to 5 over a wide range of pressures with the pulsed-dc breakdown data of Felsenthal and Proud for air, argon, and helium points strongly to avalanche gas breakdown as the dominant ionization mechanism during the net current risetime.



a. For the Case of Plasma with Infinite Conductivity



b. For the Case of Plasma with Finite Conductivity

FIGURE 2. PRIMARY, PLASMA, AND NET CURRENT WAVEFORMS

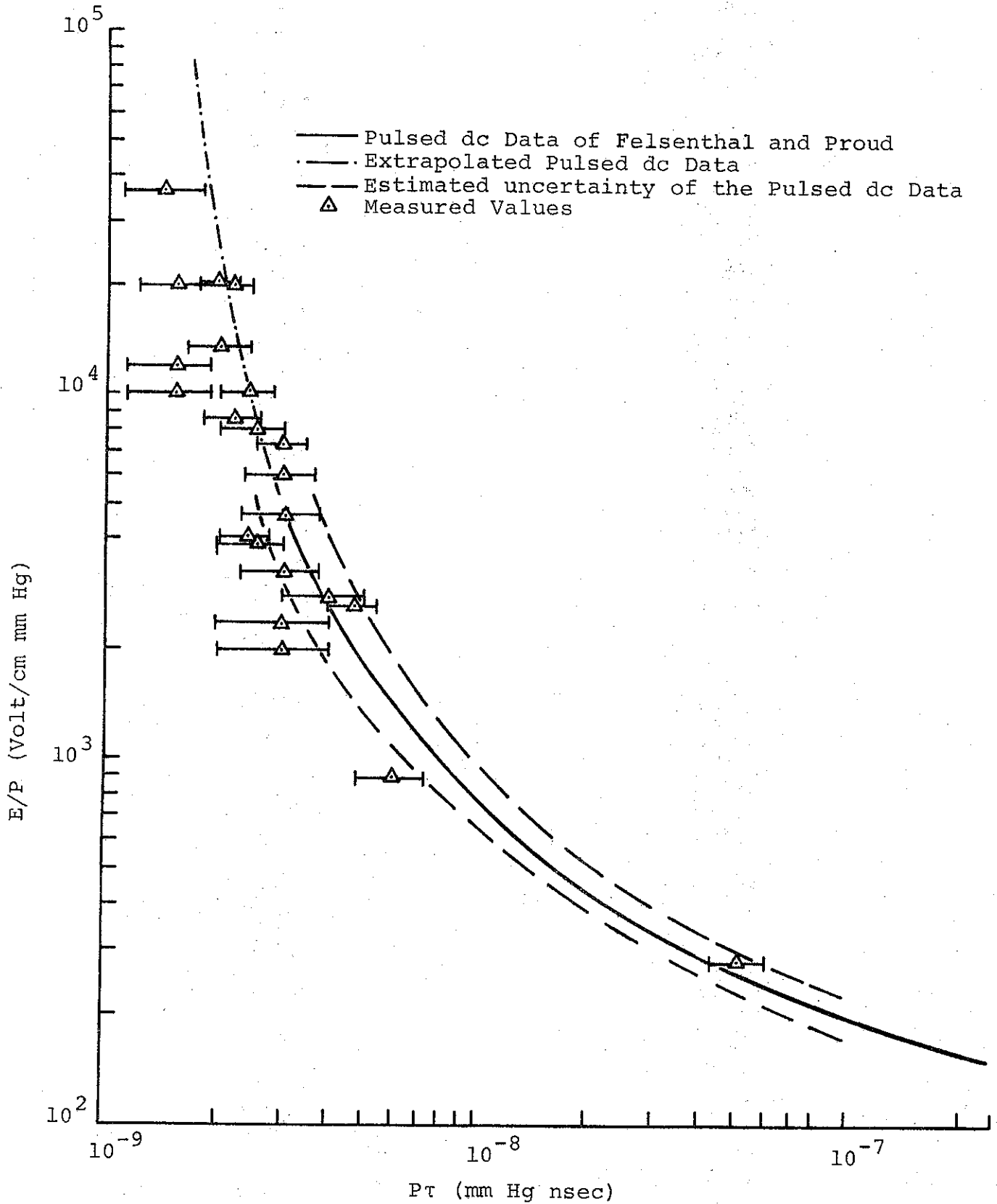


FIGURE 3. AIR BREAKDOWN DATA

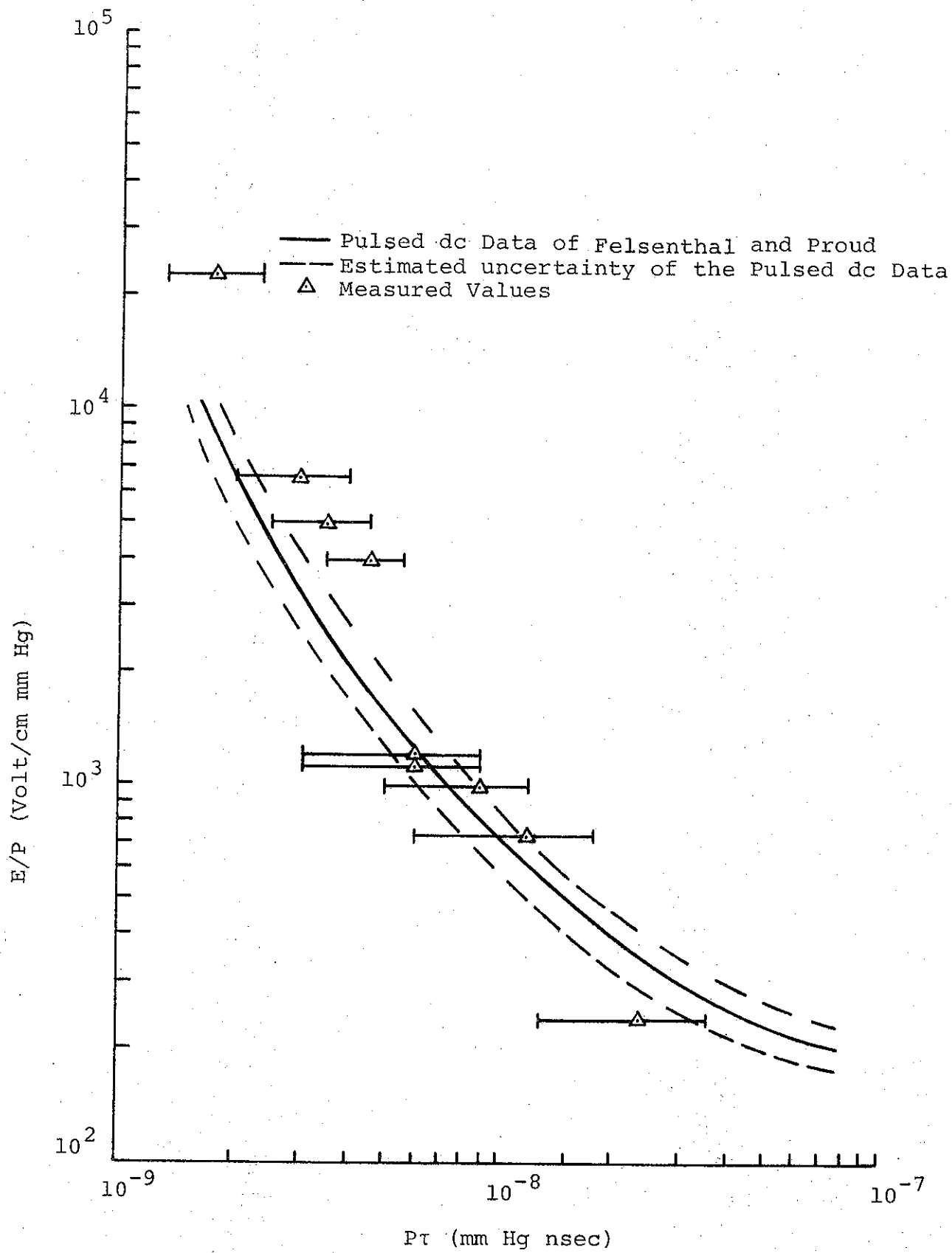


FIGURE 4. ARGON BREAKDOWN DATA

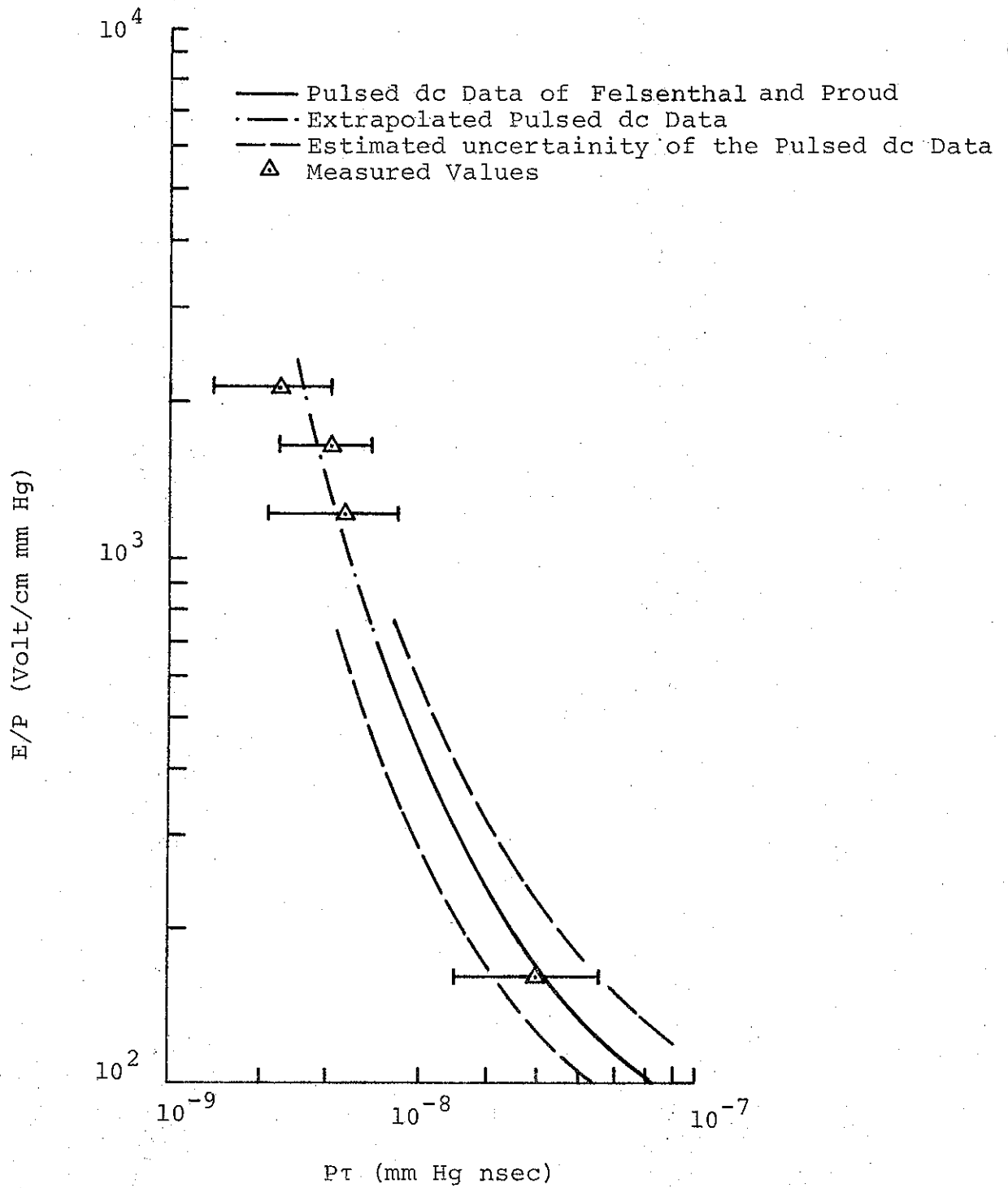
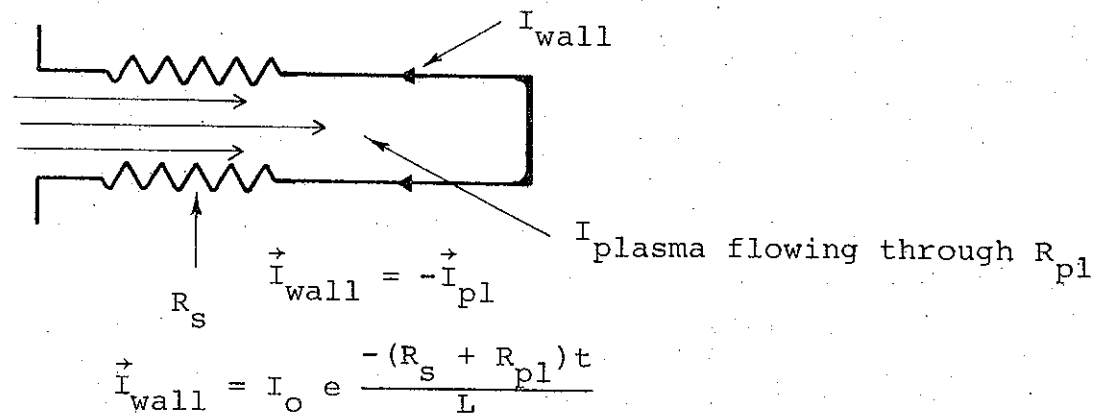


FIGURE 5. HELIUM BREAKDOWN DATA

Plasma conductivity, σ , was determined at various pressures from the observed decay of plasma current following the primary beam pulse. Data is presented in Figure 6 as current diffusion time versus pressure. The quoted decay items are those associated with the current decay in the following circuit:



where L is the self-inductance of the circuit. For uniform plasma current density in a 1-1/4 in. guide pipe L is calculated to be 10^{-7} henry/meter. Typical wall shunt resistance was $5 \times 10^{-3} \Omega$, giving a decay time contribution from the shunt of 20 msec. Thus the measured decay times (350 nsec maximum) are the current diffusion times in the conductive plasma, to good approximation.

Measurements indicate higher plasma conductivity at low pressures and a marked decrease in conductivity at pressures greater than 1.0 Torr. This is consistent with the greater deviation of the net current waveform (at higher pressures) from the idealized case of $\sigma = \infty$ (Figure 2a). That is, the net current waveform shows more rapid decay of plasma current.

The gross behavior of high v/γ beams in a large drift chamber throughout a wide range of background gas pressures can be explained in terms of the above beam-plasma interactions: space charge

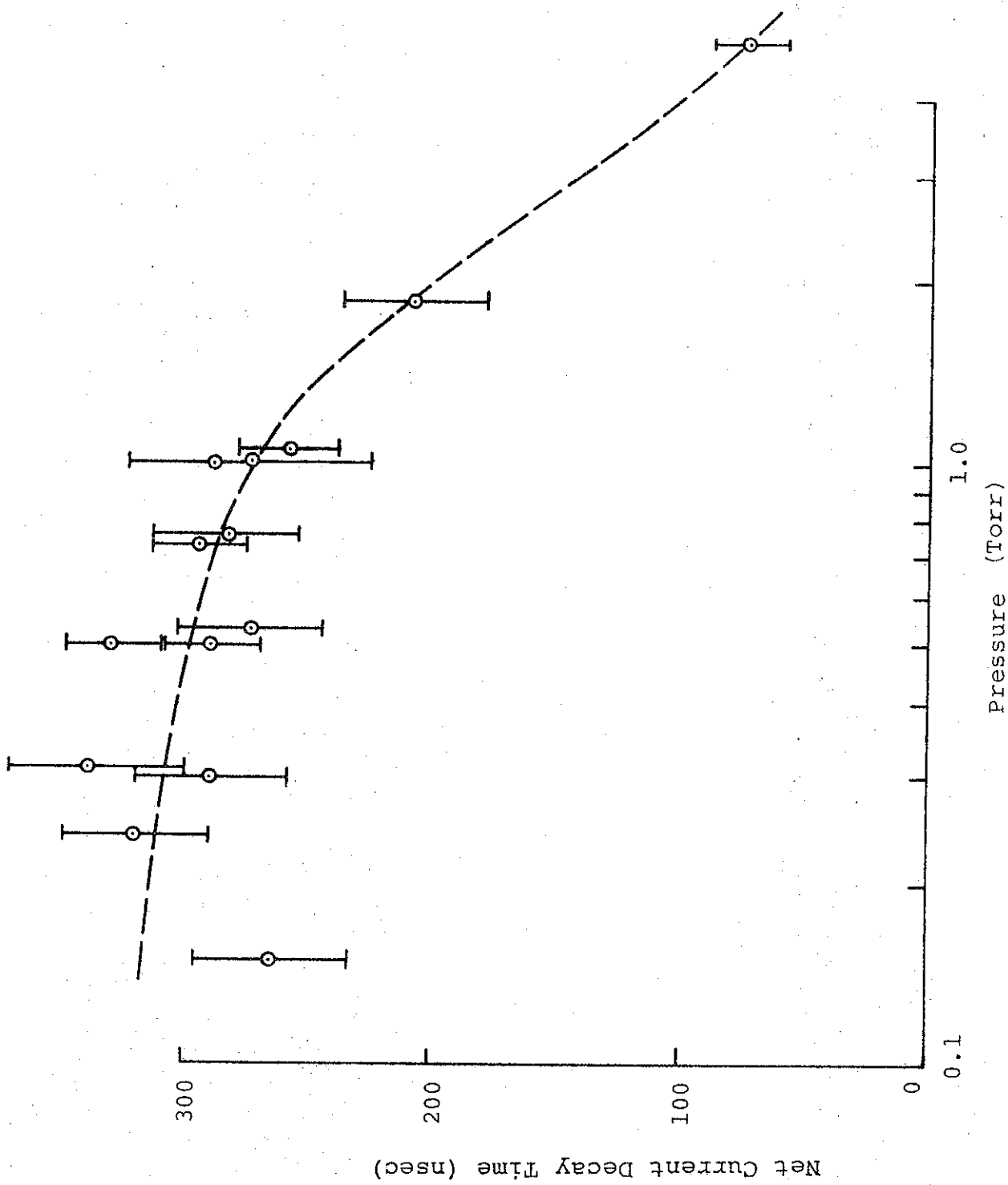


FIGURE 6. NET CURRENT DECAY TIME VERSUS PRESSURE IN AIR

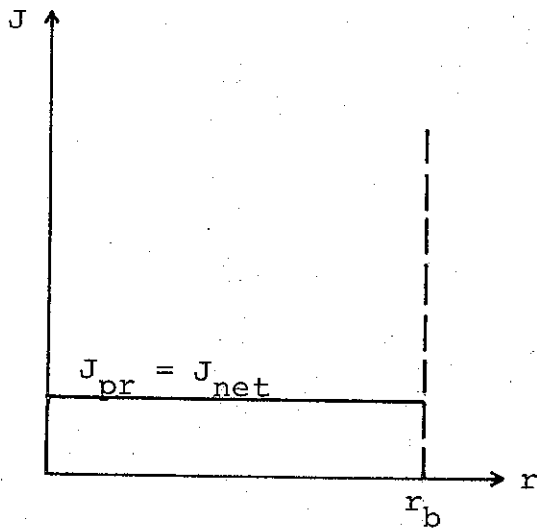
neutralization, current neutralization, and plasma conductivity. At low pressures (in these experiments $\lesssim 50 \mu$) there is insufficient time to produce space charge neutralization and the beam diverges rapidly. At pressures in the range 50 to 500 μ range, space charge neutralization occurs during the beam pulse, allowing self-pinching of the beam from magnetic compression. From 500 to 1.0 Torr the appearance of rapid current neutralization limits the degree to which the beams can pinch. In the range 1.0 to 5.0 Torr the beams become relatively force free at early times, because of rapid charge and current neutralization, and are free to diverge at a rate determined by the injection conditions (cathode-anode geometry). However, because of the rapid decrease in plasma conductivity in this pressure range, current neutralization cannot be sustained throughout the beam pulse, and pinching eventually occurs. Beams in this pressure range exhibit a varying degree of filamentary structure, indicating that pinching occurs over small isolated segments rather than uniformly over the entire beam. No firm explanation of the filamentary pinch behavior has as yet been established. It is likely, however, that any nonuniformity in current density of the divergent beam would result in filamentary pinch structure, since the magnetic attraction of electrons to a nearby local maximum in current density would be stronger than magnetic attraction to other local maxima at greater radial distances. At higher pressures, the plasma conductivity continues to drop, resulting first in a tighter filamentary structure at ~ 30 Torr, and finally a collapse into a concentrated "ball" extending only a few tens of centimeters from the anode at 300 to 760 Torr.

This model is consistent with the observed maximum transport efficiency at 750 μ where charge and current neutralization times are short (a few nsec) and plasma conductivity is high enough to sustain a low net current throughout the beam pulse.

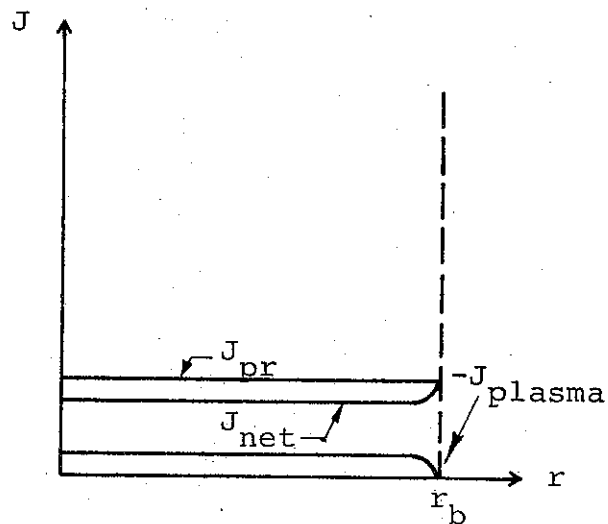
B. RADIAL STRUCTURE OF NET CURRENT AND MAGNETIC DIFFUSION

As previously shown, the existence of current neutralization phenomena in high v/γ beams strongly affects beam behavior. A description of the radial dependence of the plasma currents and the resulting effect on the structure of net currents in a metallic beam guide pipe is now in order.

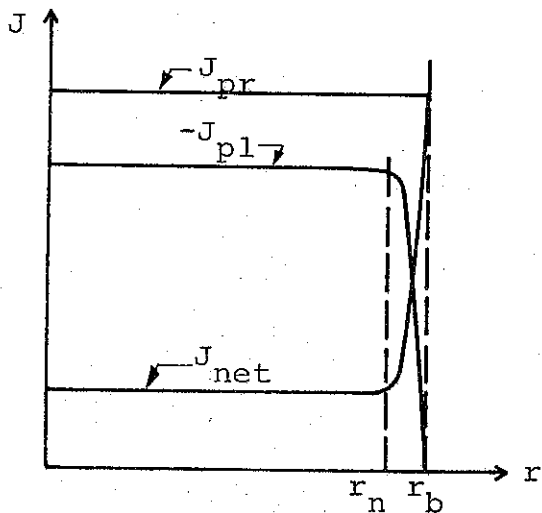
The abundance of secondary electrons and high plasma conductivity which follow avalanche breakdown of the background gas have a dramatic effect on the radial dependence of the net current and its time development. This is apparent immediately when considering a primary beam current which fills its metal guide tube. The longitudinal electric field E_z must vanish at the guide tube wall, $r = r_b$, since it is tangential to the metal surface. Consequently, no secondary electrons can flow at $r = r_b$ and the plasma current density soon after breakdown is as shown in Figure 7b. For simplicity it is assumed that the primary current is independent of radius, though increasing in time. In Figure 7b the plasma electrons have responded to longitudinal electric fields over most of the tube radius to neutralize the primary current increase after breakdown. The result is that the net current density retains the value it had at breakdown. Near the wall, however, $J_{pl}(r) \rightarrow 0$ as $r \rightarrow r_b$, and the primary current increase near $r = r_b$ is not completely neutralized. Thus the net current density increases near the guide tube wall, and is equal to the primary current density at $r = r_b$. This constitutes a net current sheath, as in Figure 7c, in the annulus $r_n \leq r \leq r_b$, where r_n is the sheath inner radius.



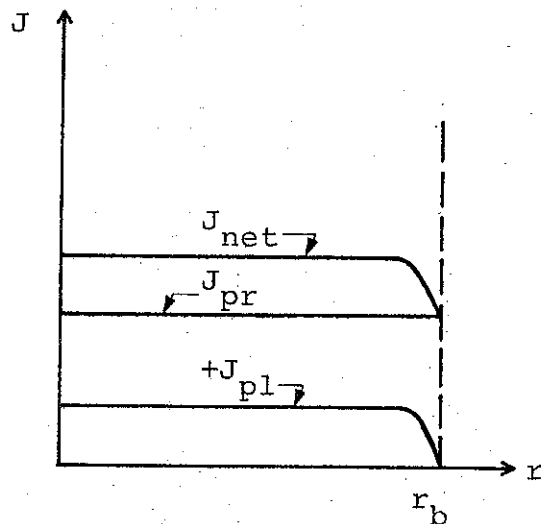
a. As Breakdown is about to occur



b. Shortly After Breakdown



c. At Peak Primary Current



d. As Primary Current Falls. Uniform Primary Current is Assumed for Simplicity

FIGURE 7. SCHEMATIC RADIAL STRUCTURE OF PRIMARY, PLASMA, AND NET CURRENT DENSITIES

The azimuthal magnetic field due to the net current configuration of Figure 7c is shown in Figure 8. Since the net current density is changing rapidly only in the sheath $r_n \leq r \leq r_b$, B_θ changes rapidly only in this region also. This gives rise, however, to an induced longitudinal electric field in the beam drives the plasma current $(J_{pl})_z = \sigma E_z$. We shall discuss this induced field quantitatively in a subsequent section on beam energy loss.

The great increase in conductivity due to breakdown has the important effect of changing the beam's magnetic field equation from wave-like to diffusion-like. From Ampere's law we obtain:

$$\vec{\nabla} \times \vec{B} = \mu_0 (\vec{J}_{pr} + \sigma \vec{E}) + \mu_0 \epsilon_0 \frac{\partial \vec{E}}{\partial t} \quad (2)$$

where we have substituted

$$\vec{J}_{pr} + \sigma \vec{E} = \vec{J}_{pr} + \vec{J}_{pl} = \vec{J}$$

By taking the curl of both sides of Equation (2), and by then substituting $\vec{\nabla} \times \vec{E} = -\partial \vec{B} / \partial t$, we get (after rearranging)

$$\nabla^2 \vec{B} - \mu_0 \sigma \left(\frac{\partial \vec{B}}{\partial t} + \frac{\epsilon_0}{\sigma} \frac{\partial^2 \vec{B}}{\partial t^2} \right) = \mu_0 \vec{\nabla} \times \vec{J}_{pr} \quad (3)$$

The relative importance of the two terms in parentheses can be seen in the following way. We can Fourier analyze the magnetic field, giving

$$B(\vec{x}, t) = \iint f(\vec{k}) F(\omega) e^{i(\vec{k} \cdot \vec{x} - \omega t)} d\omega d^3k$$

This yields

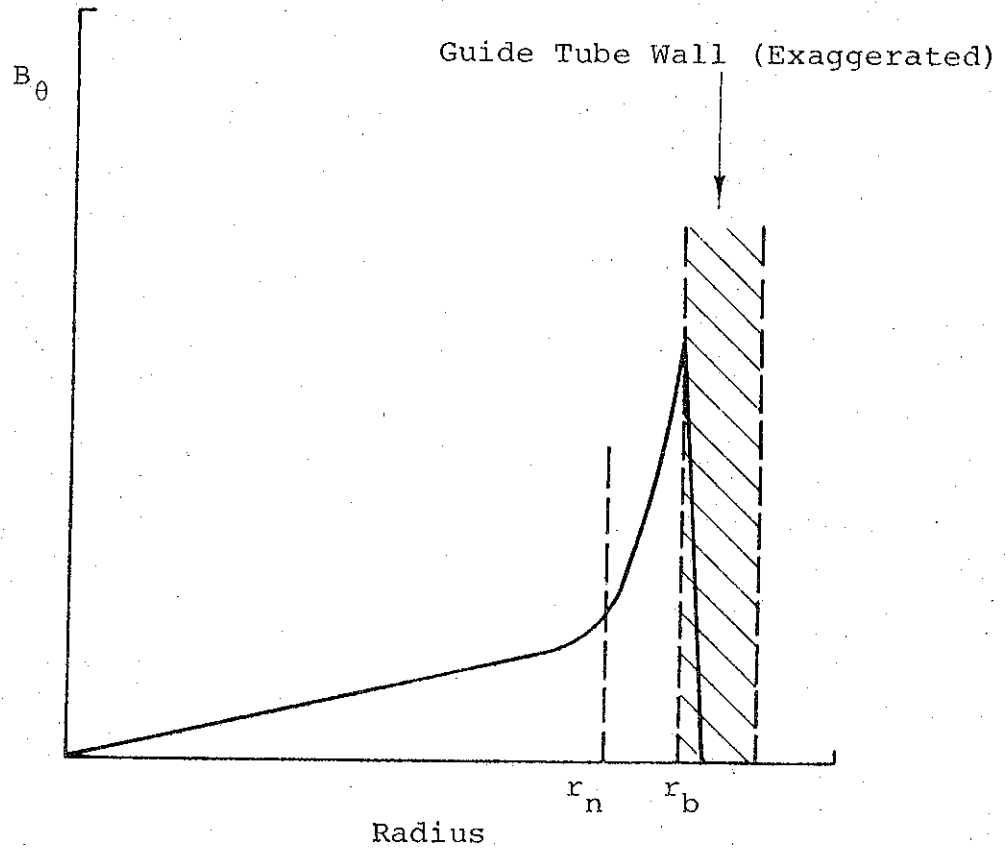


FIGURE 8. AZIMUTHAL MAGNETIC FIELD VERSUS RADIUS FOR CURRENT CONFIGURATION OF FIGURE 7 C

$$\frac{\partial \vec{B}}{\partial t} + \frac{\epsilon_0}{\sigma} \frac{\partial^2 \vec{B}}{\partial t^2} = - \iint f(\vec{k}) F(\omega) \omega \left(i + \frac{\epsilon_0}{\sigma} \omega \right) e^{i(\vec{k} \cdot \vec{x} - \omega t)} d\omega d^3k$$

Thus we can compare $\partial \vec{B} / \partial t$ with $(\epsilon_0 / \sigma) \partial^2 \vec{B} / \partial t^2$ by comparing 1 with $(\epsilon_0 / \sigma) \omega_0$, where ω_0 is the frequency at which $F(\omega)$ peaks. Since these events take place on a nanosecond time scale, $\omega_0 \approx 10^9 \text{ sec}^{-1}$, so that $(\epsilon_0 / \sigma) \omega_0 \approx 1$ before breakdown, while $(\epsilon_0 / \sigma) \omega_0 \approx 10^{-4}$ after breakdown. After breakdown the second derivative with respect to time term (which stems from the displacement current) can be neglected, leaving

$$\nabla^2 \vec{B} - \mu_0 \sigma \frac{\partial \vec{B}}{\partial t} \equiv \mu_0 \vec{\nabla} \times \vec{J}_{pr} \quad (4)$$

This is a diffusion equation for the magnetic field. We have already seen how the azimuthal magnetic field can become relatively large soon after breakdown only in a thin sheath at the guide tube wall. The diffusion nature of the \vec{B} equation indicates that this restriction can relax in time, that is, the net current sheath broadens as the lack of plasma current near the wall diffuses radially inward, at a rate determined by the conductivity (diffusion rate increasing with decreasing σ).

This process is accentuated by the finite fall-off of the primary beam current, which is counteracted (Lenz's law) by an acceleration of plasma electrons in the direction of beam propagation. Late in the beam pulse the net current actually exceeds the primary current and fills the guide pipe, as in Figure 7d.

Zwick (Reference 4) has used a Green's function technique to exactly solve Equation (3) under certain simplifying assumptions. He found the plasma current density, $J_{p1}(r, z, t)$ for a cylindrical beam of finite length, propagating at relativistic velocity in an ionized gas of conductivity σ . Zwick's model does not include avalanche breakdown or finite boundary conditions, but his quantitative findings strongly substantiate our qualitative arguments. The principal asymptotic plasma current terms he obtains are (in cgs units)

$$\left(\frac{J_{pl}}{J_{pr}}\right)_r \sim \frac{J_{pr}}{2} \left(\frac{c}{v}\right) \sqrt{\frac{\tau}{\pi t}} \exp \left\{ -\frac{(r - r_b)^2}{4c^2 \tau t} \right\} \quad (5)$$

$$\left(\frac{J_{pl}}{J_{pr}}\right)_z \sim \frac{J_{pr}}{2} \operatorname{erfc} \left(\frac{r - r_b}{2c \sqrt{\tau t}} \right)$$

when $t \gg \tau = 1/4\pi\sigma \approx 3 \times 10^{-15}$ sec*. Here v is the primary electron velocity and $\operatorname{erfc}(x)$ is the complementary error function

$$\operatorname{erfc}(x) = \frac{2}{\sqrt{\pi}} \int_x^{\infty} e^{-s^2} ds$$

Equations (5) show that the region carrying a finite net current in Zwick's model is confined to points near the surface of the beam. Because $\operatorname{erfc}(x) < 1/2$ for $x > 1/2$, the thickness of this sheath is

$$\Delta r \approx c \sqrt{\tau t} \approx \sqrt{2.7 \times 10^6 t}$$

valid when $\Delta r \ll r_b$.

Using $t = 0$ as the breakdown time in our more recent model, we find that $\Delta r \approx 2.4$ mm, 20 nsec after breakdown. (This agrees with order-of-magnitude estimates made later in the section on energy loss due to induced electric fields.) Zwick's complete solutions predict the late-time behavior discussed previously.

C. RELATION OF NET CURRENT TO BEAM TRANSVERSE ENERGY COMPONENTS

Since net current magnitudes reported previously (Reference 2) imply that $(v/\gamma)_{\text{net}}$ can be > 1 , these beams should be classed as plasma streams, and are expected to have large transverse

* We have measured typically $\sigma = 25$ mho/cm by observation of plasma current decay times following primary current termination. (See Reference 2).

energy components. Table III presents results of various calculations relating transverse energy to v/γ . Lawson's calculation is valid only for $v/\gamma \ll 1$, considerably outside the range of present interest. No previous calculations allow for current neutralization (arising from backstreaming plasma electrons) in arriving at a balance equation between the transverse kinetic pressure and the $\vec{j} \times \vec{B}$ magnetic pressure. In the present calculation a three component plasma stream is considered, i.e., primary electrons, plasma electrons, and ions. Space charge neutralization, $\rho = \rho_{pr} + \rho_{pl} + \rho_i = 0$, is assumed throughout the beam channel.

The transverse energy of the system can be expressed as a two dimensional (transverse) temperature. Depending on the number density of particles, n , this temperature exerts a radial pressure which must be balanced by the $\vec{j} \times \vec{B}$ body force in order to obtain beam containment. In the transverse plane the radial pressure is written

$$P \equiv P_{\perp} = n_{pr} \left(\frac{1}{2} \gamma m \bar{v}_{\perp}^2 \right)_{pr}$$

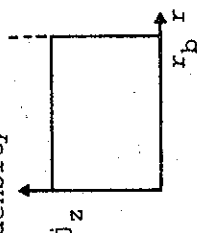
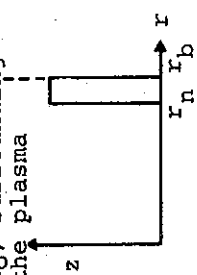
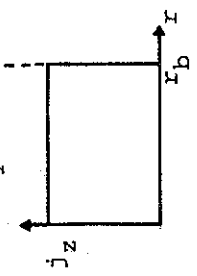
where (\bar{v}_{\perp}^2) for the plasma electrons and positive ions is assumed negligible.

The pressure gradient must equal the body force $\vec{\nabla} p = \vec{j} \times \vec{B}$ and if B_{θ} is the only nonvanishing component of magnetic field:

$$\frac{dp}{dr} = - j_z B_{\theta}$$

TABLE III

CALCULATIONS OF BEAM TRANSVERSE ENERGY

Author	Lawson (Reference 11) (Trajectory calculation)	Post (Reference 12) (Magnetic pressure balance)	Spitzer (Reference 13) (Generalization of Bennett pinch relation from magnetic pressure balance)	Present Report (Magnetic pressure balance including current neutralization)
Assumptions	<ol style="list-style-type: none"> $v/\gamma \ll 1$ Space charged neutralized beam Uniform current density 	<ol style="list-style-type: none"> v/γ unrestricted Space charged neutralized plasma at a kinetic temperature T. (Uniform plasma temperature $T_{ions} = T_{electrons}$) Current sheath, I_0, surrounding the plasma 	<ol style="list-style-type: none"> v/γ unrestricted Space charge neutralization in hot current carrying plasma Uniform current density 	<ol style="list-style-type: none"> v/γ unrestricted Space charge neutrality Partial current neutralization: Arbitrary distribution of net current over the beam channel $\int_0^{r_b} \vec{j}_{net} \cdot d\vec{A} = (1-f_m) I_{pr}$
Conclusions	<ol style="list-style-type: none"> No current neutralization $\frac{\langle \beta_{\perp}^2 \rangle}{\langle \beta_{\parallel} \rangle^2} = v/\gamma$	$I_0^2 = 2NKT$ $N = \text{total \# particles / unit length}$ <p>If sheath contains only electrons at current I_0,</p> $\frac{\langle \beta_{\perp}^2 \rangle}{\langle \beta_{\parallel} \rangle^2} = \frac{v}{2\gamma} \left(\frac{r_n}{1 - \frac{r_n^2}{r_b^2}} \right)^2$	$\frac{\langle \beta_{\perp}^2 \rangle}{\langle \beta_{\parallel} \rangle^2} = v/\gamma$ <p>If ion temperature $T_i = 0$</p>	<ol style="list-style-type: none"> Transverse temperature contributed only by primary electrons: $T_{ions} = T_{plasma electrons} \approx 0$ $\frac{\langle \beta_{\perp}^2 \rangle}{\langle \beta_{\parallel} \rangle^2} = \frac{v/\gamma(1-f_m)^2}{\langle \beta_{\parallel} \rangle^2} = (v/\gamma)_{net} (1-f_m)$
				$\text{Note: } v = \frac{I_{pr} \text{ (amp)}}{17 \times 10^3 \langle \beta_{\parallel} \rangle}$

where j_z is the net current density and B_θ is the magnetic field at a radius r .

From Ampere's law:

$$\begin{aligned} (\vec{\nabla} \times \vec{B})_z &= 4\pi j_z \\ B_\theta &= \frac{4\pi}{r} \int_0^r r' j_z(r') dr' \end{aligned}$$

then

$$P = P(r=0) - \int_0^r j_z(r') \frac{4\pi}{r'} \left[\int_0^{r'} r'' j_z(r'') dr'' \right] dr' \quad (6)$$

At the beam edge, $P = 0$, which implies

$$P(r=0) = P_0 = \int_0^{r_b} j_z(r') \frac{4\pi}{r'} \left[\int_0^{r'} r'' j_z(r'') dr'' \right] dr' \quad (7)$$

To evaluate the radial dependence of the transverse pressure, the net current density must be known. However, the average pressure can be evaluated independently of the particular net current distribution:

$$\langle P \rangle = \frac{1}{\pi r_b^2} \int_0^{r_b} 2\pi r P(r) dr \quad (8)$$

Integration by parts gives:

$$\langle P \rangle = \frac{I_{net}^2}{2\pi r_b^2} \quad (9)$$

where

$$I_{\text{net}} = 2\pi \int_0^{r_b} j_z(r) r dr$$

The average pressure and total net current can also be expressed in terms of $\langle v_{\perp}^2 \rangle$ and $\langle v_{\parallel} \rangle$, where the brackets indicate averages over all the primary beam electrons:

$$\langle P \rangle = \frac{N}{\pi r_b^2} \frac{1}{2} \gamma^m \langle v_{\perp}^2 \rangle$$

$$I_{\text{net}} = N \frac{e}{c} \langle v_{\parallel} \rangle (1 - f_m)^*$$

N = # primary electrons/unit beam length

Substitution of these relations into Equation (9) yields:

$$\frac{\langle \beta_{\perp}^2 \rangle}{\langle \beta_{\parallel} \rangle^2} = \frac{v}{\gamma} (1 - f_m)^2 \equiv \left(\frac{v}{\gamma} \right)_{\text{net}} (1 - f_m), \text{ where } v = \frac{Ne^2}{mc^2} \quad (10)$$

When $f_m = 0$ (i.e., no current neutralization) Equation (10) reduces to Spitzer's result. On the other hand, when current neutralization occurs in the beam channel, the ratio of transverse to longitudinal energy is reduced by the factor $(1 - f_m)^2$. Use of Equation (10) depends on the measurement of net current flowing only through the cross sectional area defined by the primary beam, i.e., the beam must "fill" the area over which the net current is monitored.

* Units of all equations involving charge and current in this section are emu, with the charge expressed in esu ($e/c = \text{emu unit of charge}$). These units are consistent with Lawson's and Spitzer's notation.

It should be noted that equation 10 is not sufficient to define the ratio of transverse to longitudinal energy, since the parameter v contains the quantity $\langle \beta_{\parallel} \rangle$. Beginning with the definition of v as Ne^2/mc^2 and substituting

$$N = I_{\text{primary}} \left(\frac{c^2}{e} \right) \frac{1}{\langle \beta_{\parallel} \rangle} \quad \text{we find:}$$

$$v = I_{\text{primary}} \left(\frac{e}{mc^2} \right) \frac{1}{\langle \beta_{\parallel} \rangle} = \frac{I_{\text{primary}} \text{ (amps)}}{17,000 \langle \beta_{\parallel} \rangle}$$

Substitution of this expression for v into equation (10) gives:

$$\frac{\langle \beta_{\perp}^2 \rangle}{\langle \beta_{\parallel} \rangle^2} = \frac{I_{\text{pr}}}{17 \times 10^3} (1-f_m)^2 \frac{1}{\langle \beta_{\parallel} \rangle \gamma} \quad (10a)$$

A second independent relation between β_{\perp} and β_{\parallel} is:

$$\langle \beta_{\perp}^2 \rangle + \langle \beta_{\parallel}^2 \rangle = \langle \beta^2 \rangle$$

One further assumption is a small variance in β_{\parallel} , i.e.

$$\langle \beta_{\parallel}^2 \rangle - \langle \beta_{\parallel} \rangle^2 \approx 0$$

The physical meaning of this assumption is that the primary electron trajectories are sufficiently "turbulent" that electrons of equal energy comprising a given segment of the beam arrive at the target location at the same time (i.e. β_{\parallel} for any electron in that portion of the beam is equal to $\langle \beta_{\parallel} \rangle$ for all the electrons

in that portion). Time of flight measurements for various portions support this assumption. (The oscillatory structure of the bremsstrahlung pulse produced at the anode is preserved after transport for lengths up to four meters).

The above energy conservation relation can then be written:

$$\frac{\langle \beta_{\perp}^2 \rangle}{\langle \beta_{\parallel} \rangle^2} = \frac{\langle \beta \rangle^2}{\langle \beta_{\parallel} \rangle^2} - 1$$

Equating this result with the other expression for $\langle \beta_{\perp}^2 \rangle / \langle \beta_{\parallel} \rangle^2$ (Equation 10a) gives a quadratic equation for $\langle \beta_{\parallel} \rangle$:

$$\langle \beta_{\parallel} \rangle^2 + \langle \beta_{\parallel} \rangle \frac{(1-f_m)^2}{\gamma} \frac{I_{pr}}{17 \times 10^3} - \langle \beta \rangle^2 = 0$$

The solution is

$$\langle \beta_{\parallel} \rangle = \frac{I_{pr}}{17 \times 10^3} \frac{(1-f_m)^2}{2\gamma} \left[\sqrt{1 + \left[\frac{34 \times 10^3 \beta \gamma}{I_{pr} (1-f_m)^2} \right]^2} - 1 \right]$$

Equation 10 then becomes:

$$\frac{\langle \beta_{\perp}^2 \rangle}{\langle \beta_{\parallel} \rangle^2} = \frac{2}{\sqrt{\left[\frac{34 \times 10^3 \beta \gamma}{I_{pr} (\text{amp}) (1-f_m)^2} \right]^2 + 1} - 1} \quad (11)$$

Hence knowledge of I_{primary} , I_{net} , and the electron energy allows calculation of the ratio of transverse to longitudinal energy by this model.

Currently three separate experimental results indicate the existence of primary electron transverse velocity components. As reported earlier (Reference 2) the results were consistent with $\tan \theta \approx \sqrt{(v/\gamma)_{\text{net}}}$, although the previous experiments were not sufficiently defined to indicate which expression [$\tan \theta \approx \sqrt{(v/\gamma)_{\text{net}}}$ or Equation (11)] is more correct.

The first indication of transverse energy was found in our inability to predict measured electron deposition profiles (using electron energy spectra defined by the voltage and current monitors) when we assumed normal incidence ($\theta = 0^\circ$) at the dosimeter. Two examples of these observations are given in Figures 9 and 10. Note that the calculated deposition ($\theta = 0^\circ$) is lower near the front surface and higher at moderate depths into the material. Calculations assuming a single angle of incidence for all beam electrons agree better with the measured deposition profiles.

Another indication of transverse velocity is the time of flight data shown in Figure 11. Observations were made (Reference 2) of the time-resolved bremsstrahlung production in high Z targets placed at different transport lengths. Oscillations inherent in voltage and current waveforms allowed time of flight measurements of various portions of the beam as well as the beam front. The bulk of the beam propagated at velocities slower than expected for zero transverse temperature.

The most sensitive measurements of transverse energy to date, at least in terms of accurate definition of electron beam parameters, has been the observation of electron number deposition versus depth in aluminum and subsequent comparison to Monte Carlo calculations of this electron deposition. The data in Figure 12 generated as part of a recent program funded by Sandia, Livermore

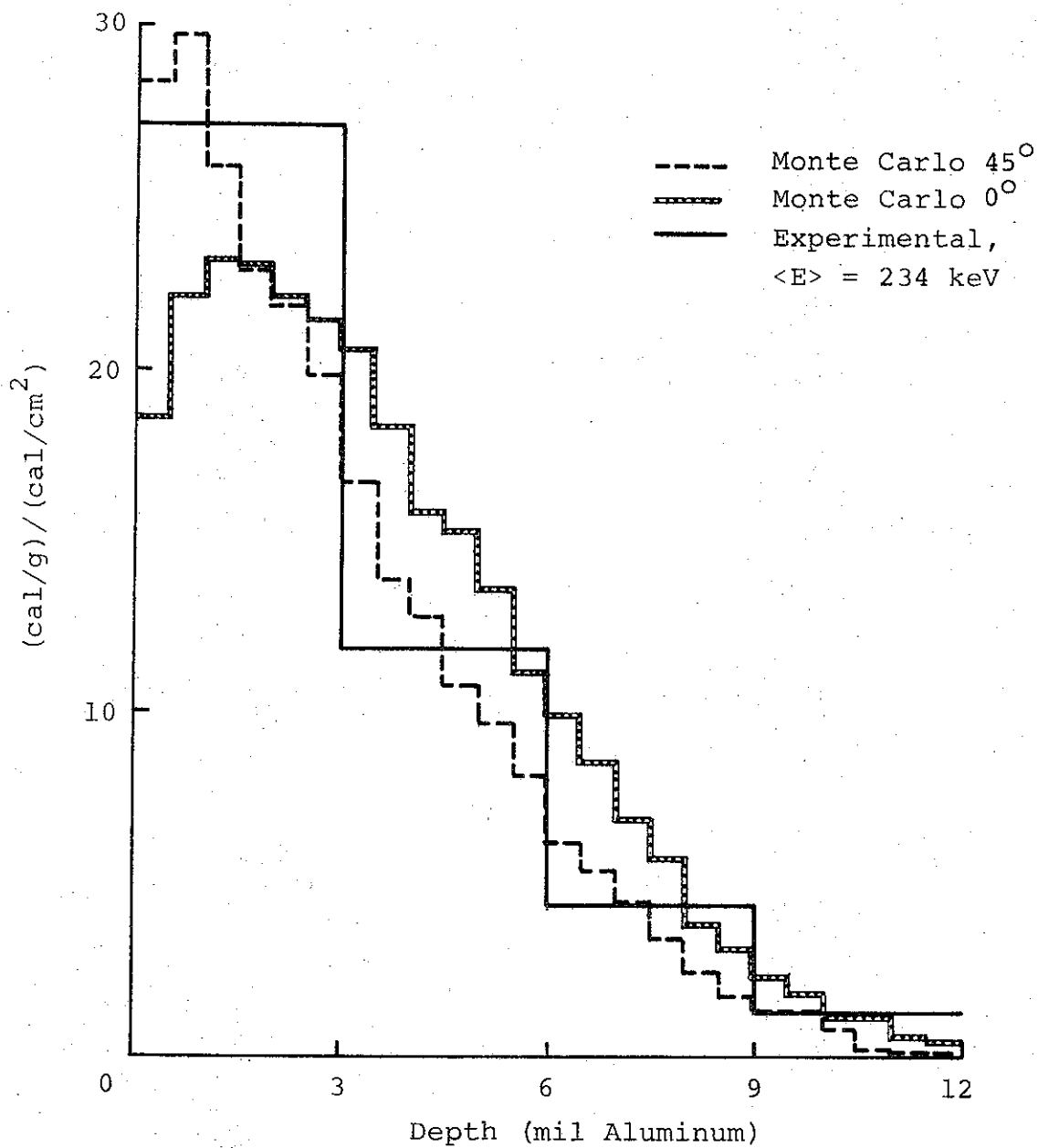


FIGURE 9. CALCULATED AND MEASURED ELECTRON DEPOSITION PROFILES IN ALUMINUM, MEAN ELECTRON ENERGY = 234 keV

7567

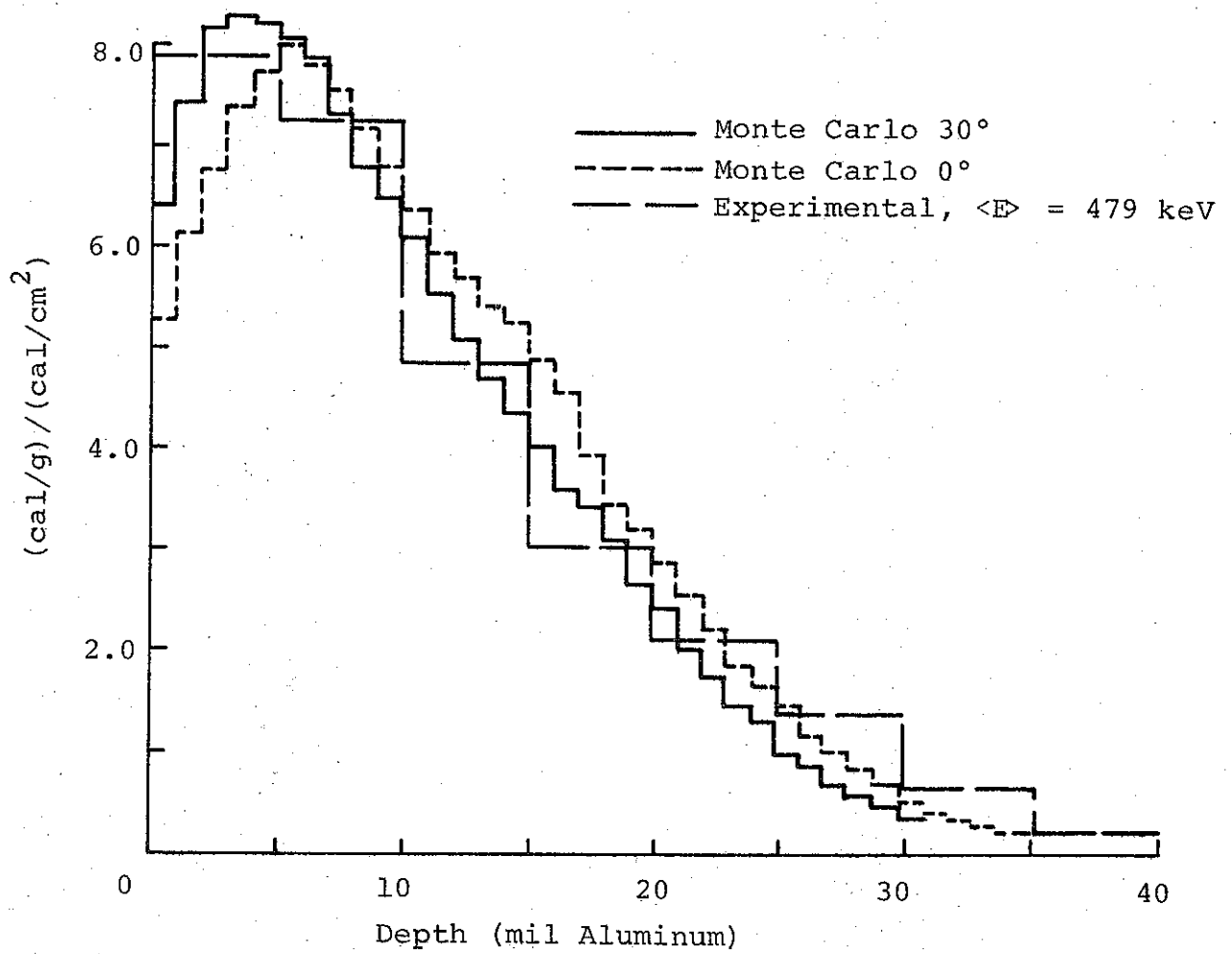


FIGURE 10 CALCULATED AND MEASURED ELECTRON DEPOSITION PROFILES IN ALUMINUM, MEAN ELECTRON ENERGY = 479 keV

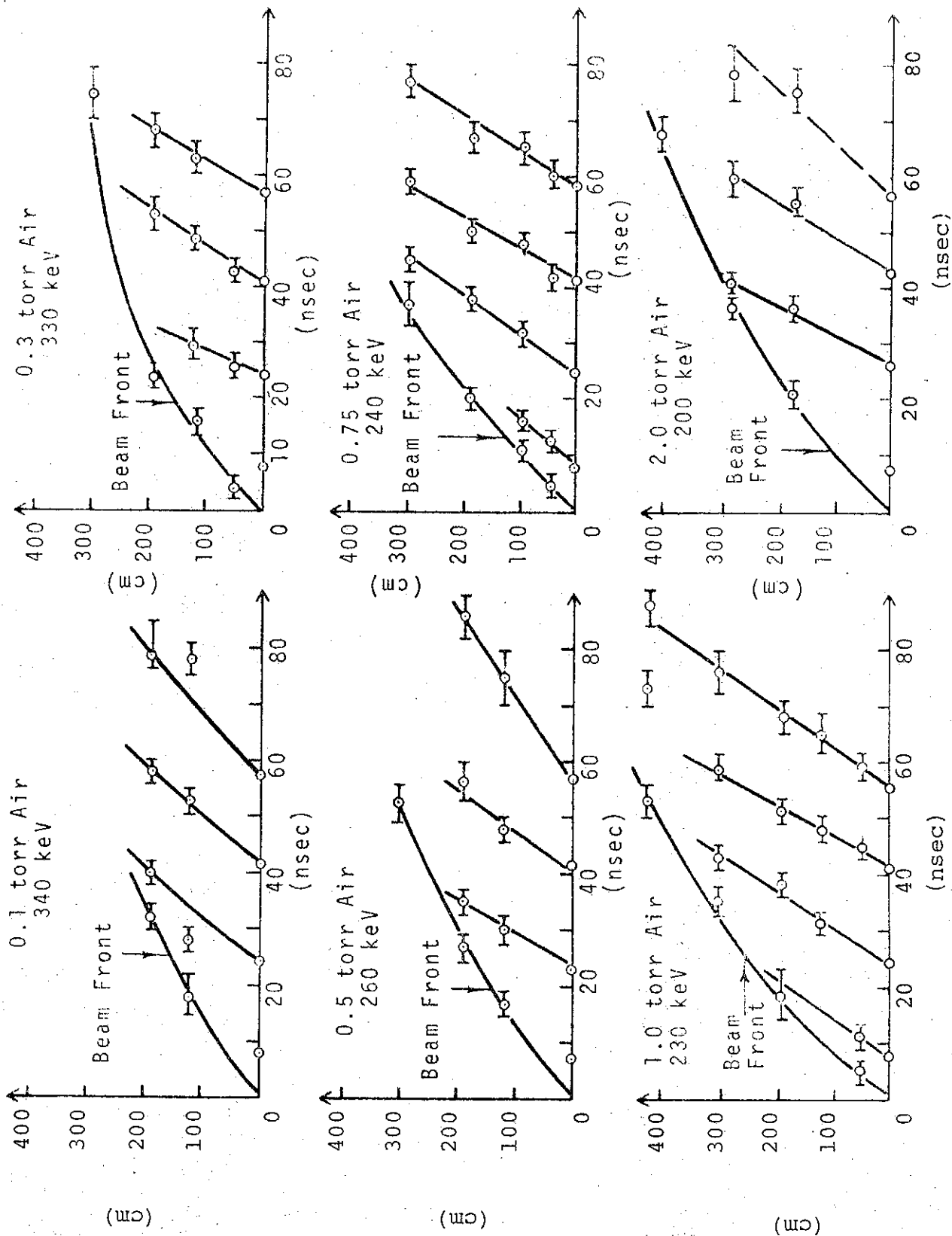


FIGURE 11. BEAM TIME OF FLIGHT DATA

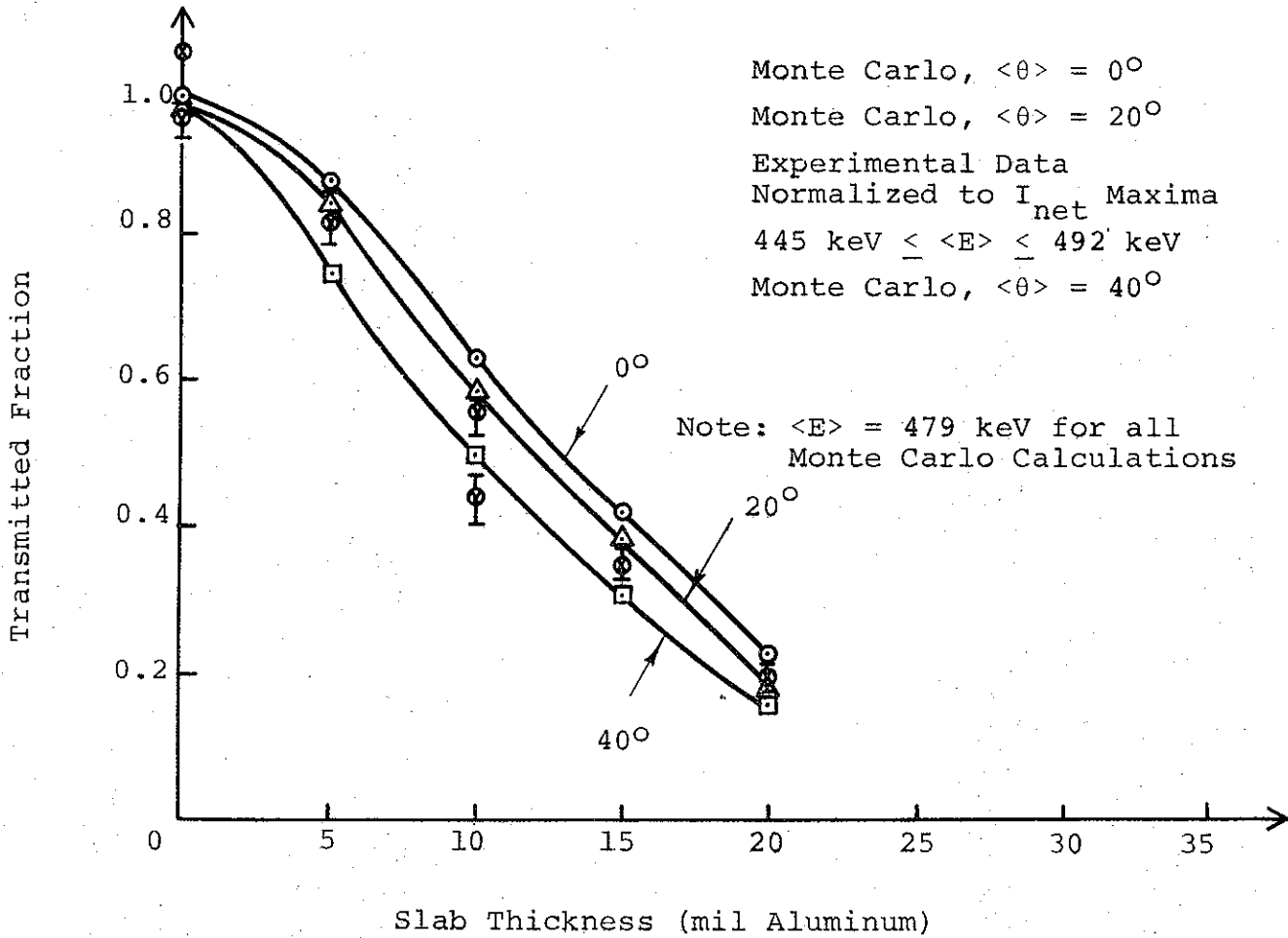


FIGURE 12. ELECTRON NUMBER DEPOSITION IN ALUMINUM

(Reference 14) determined the mean angle of electron incidence at the target location. Relevant parameters (averaged over the FWHM pulse duration) were:

$$\begin{aligned} \langle E \rangle &= 480 \text{ keV} \\ \langle \beta \gamma \rangle &= 1.64 \\ (1-f_m) &= 0.6 \\ I_{pr} &= 25 \text{ KA} \end{aligned}$$

The electron number transmission measurements (Figure 12) show $\langle \theta \rangle = 30^\circ \pm 5^\circ$ in good agreement with the prediction of Equation 11:

$$\frac{\langle \beta_{\perp}^2 \rangle}{\langle \beta_{\parallel} \rangle^2} = 0.38, \text{ or } \langle \theta \rangle = \tan^{-1} \sqrt{\frac{\langle \beta_{\perp}^2 \rangle}{\langle \beta_{\parallel} \rangle^2}} = 31^\circ.$$

Note that the electron energy deposition vs depth data presented in Figure 10 is also consistent with this mean angle of electron incidence.

A more recent test of this model was afforded by data collected as part of a contract from Lockheed Missiles and Space Company (Reference 15). Electron beam parameters are given below:

$$\begin{aligned} \langle E \rangle &= 240 \text{ keV} \\ \langle \beta \gamma \rangle &= 1.08 \\ (1-f_m) &= 0.9 \\ I &= 45 \text{ KA} \end{aligned}$$

Number transmission data is given in Figure 13 and compared to Monte Carlo calculations of expected electron number transmission for three different mean angles of incidence, 50° , 60° , and 70° . Experimental data show $\langle \theta \rangle = 63 \pm 5^\circ$ in excellent agreement with the prediction of Equation 11:

$$\frac{\langle \beta_{\perp}^2 \rangle}{\langle \beta_{\parallel} \rangle^2} = 4.75, \text{ or } \langle \theta \rangle = \tan^{-1} \sqrt{\frac{\langle \beta_{\perp}^2 \rangle}{\langle \beta_{\parallel} \rangle^2}} = 65^\circ$$

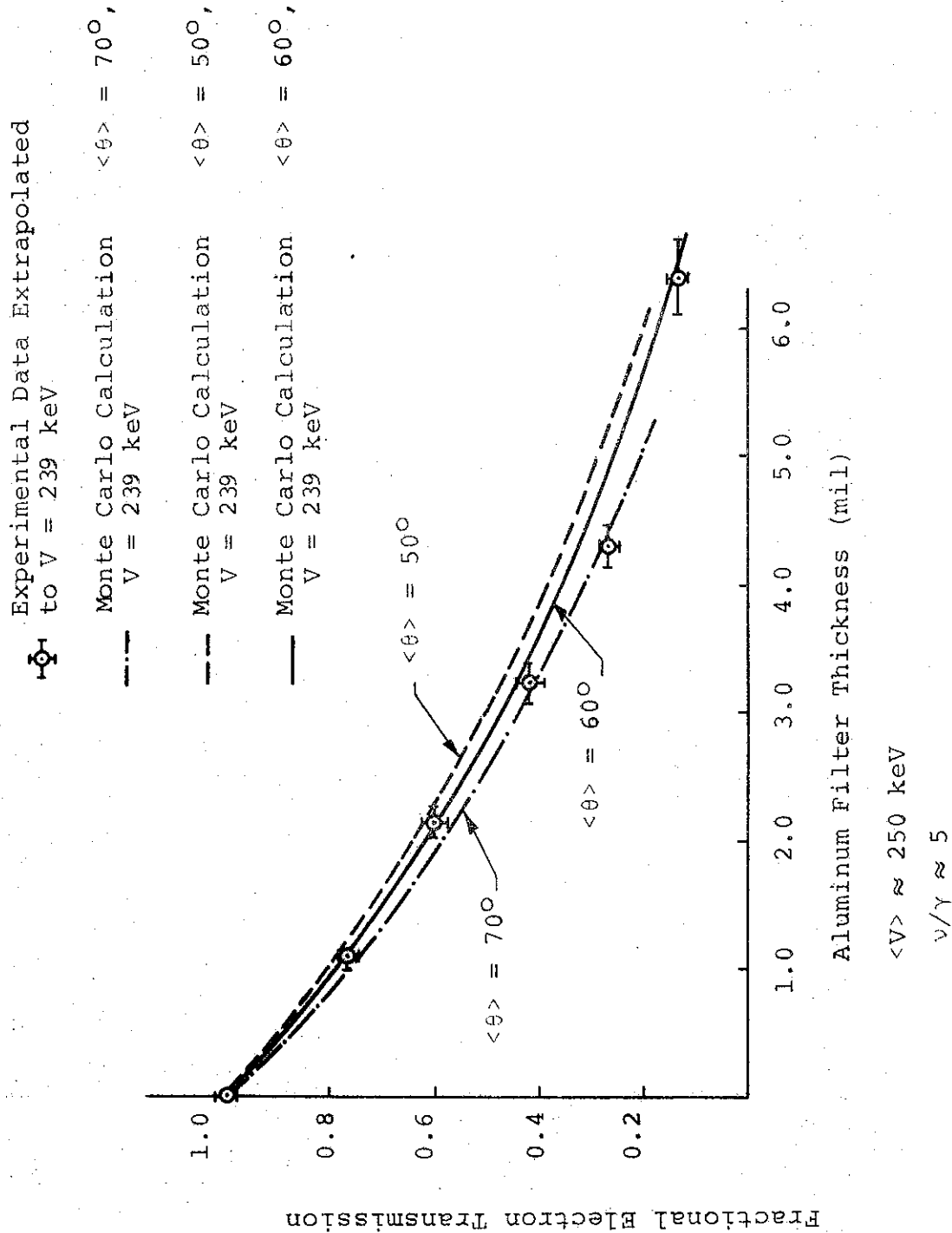


FIGURE 13. ELECTRON TRANSMISSION DATA IN ALUMINUM, $\langle E \rangle \approx$ keV

Since the parameters γ , I_{primary} , and $(1-f_m)$ in Equation 11 are varying with time during the beam pulse it is obvious that a more complete comparison with experimental data would require allowance for a time dependent ratio of transverse to longitudinal electron energy. However the fact remains that one can estimate, to a good approximation the electron energy deposition profile and number transmission profile from the magnetic pressure balance theory using the time averaged values of γ , I_{primary} , and $(1-f_m)$.

Future tests of this model will be possible at both extremes of high and low transverse electron temperature. In particular: high current, low energy ($\langle E \rangle = 100$ keV) electron beams should show even larger transverse temperatures at pressures where current neutralization is minimal. At the other extreme, beams transported in a pre-ionized channel containing enough secondary electrons to completely current neutralize the beam should contain very little transverse energy. In order to obtain efficient beam transport with pre-ionization the diode geometry would have to be designed to prevent pinching or the creation of large transverse electron temperature in the anode-cathode gap.

In summary, substantial transverse energy components exist in high v/γ electron streams and the actual ratio of transverse to longitudinal energy depends on both v/γ and the degree of current neutralization in the beam channel ($I_{\text{net}} = (1-f_m) I_{\text{pr}}$, where f_m = current neutralization factor). The best data available (number transmission versus depth) is consistent with the result of a magnetic pressure balance calculation which predicts:

$$\frac{\langle \beta_{\perp}^2 \rangle}{\langle \beta_{\parallel}^2 \rangle} = \frac{2}{\sqrt{\left(\frac{34 \times 10^3 \beta \gamma}{I_{\text{primary}} (\text{amp}) (1-f_m)^2} \right)^2 + 1} - 1}$$

D. BEAM ENERGY LOSS

Since many of the features of beam current neutralization in the 0.75 Torr pressure range have been explained, an investigation of the mechanisms which can degrade the total beam energy may now be made. Development of beam-handling capabilities necessitates understanding the mechanisms responsible for observed propagation loss.

Energy loss mechanisms relevant to the beams under study are:

- a. Energy loss due to induced longitudinal electric fields, E_z
- b. Dissipative energy loss due to finite plasma conductivity, $(\vec{J} \cdot \vec{E} \text{ loss})$
- c. Radiated loss due to electron acceleration
- d. Loss due to ionization of the background gas
- e. Other losses (radio frequency radiation and energetic ion production)
- f. Loss due to transverse energy

Loss due to transverse energy dominates all others.

1. Energy Loss Due To Induced Longitudinal Electric Fields E_z

The changing net current within the guide tube radius establishes a changing azimuthal magnetic field, resulting in an induced longitudinal electric field E_z . This effect is most pronounced before gas breakdown, when the net current equals the rapidly rising primary current. Assuming radially uniform primary current, $E_z = 10^{-7} (\partial I_{\text{net}} / \partial t)$ (mks) before breakdown (Reference 2, p. 43). At 0.75 Torr, for example, we have measured $E_z = 3.4 \times 10^3$ V/cm, 10 cm from the anode.

After breakdown the net current changes relatively slowly and is a function of radius. For an order-of-magnitude calculation the net current is considered constant in $r < r_n$ after breakdown (and equal to the primary current there at breakdown), so that $\partial I_{\text{net}}/\partial t \neq 0$ results from a changing net current in $r_n < r < r_b$ only. Using $\vec{\nabla} \times \vec{E} = -\partial \vec{B}/\partial t$ and a rectangular Stoke's Law path in the r, z plane,

$$E_z = -10^{-7} \frac{d I_{\text{net}}}{dt} \left[1 - \frac{\ln (r_b^2/r_n^2)}{(r_b^2/r_n^2 - 1)} \right], \quad r \leq r_n$$

Note that E_z is constant over the beam for radii less than r_n and the magnitude of E_z is equal to the results for a radially uniform $d I_{\text{net}}/dt$ ($E_z = 10^{-7} d I_{\text{net}}/dt$) reduced by a geometric factor which depends on the sheath thickness. The geometric factor is tabulated below:

$\frac{r_b}{r_n}$	$\frac{E_z}{10^{-7} \frac{\partial I_{\text{net}}}{\partial t}}$
10	0.998
2	0.538
1.41	0.307
1.22	0.190
1.12	0.108
1.05	0.066

The diffusion phenomenon previously described indicates that (r_b/r_n) is a function of distance behind the beam front, until this ratio is no longer meaningful, i.e., the current "sheath" becomes ill-defined. After breakdown (when Equation 6 is applicable) $\partial I_{\text{net}}/\partial t$ is typically one order of magnitude smaller than that prior to breakdown. Thus we find that just after breakdown E_z can be 10^{-2} (or less) times its pre-breakdown value, or about 30 volts/cm. Subsequently it appears that it might approach its pre-breakdown value. If this were the case, however,

our beam timing data would indicate the deceleration of various segments of the beam. No such deceleration is observed, suggesting that the sheath thickness remains small; the diffusion process does not have sufficient time, at 0.75 Torr, to cause a major change in the plasma current profile. This deduction is substantiated by our independent measurements of the characteristic diffusion time $kA\sigma (\equiv \mu_0 \sigma r_b^2/4)$, giving $kA\sigma \approx 200-300$ nsec. After only 50 nsec our beams begin to shut off, a period considerably shorter than the diffusion time.

E_z before breakdown is large, however, and has a profound effect on electrons at the beam front. It is the cause of beam front deceleration (Reference 2, p. 43). As described earlier, beam timing measurements show less beam front deceleration with increasing pressure. Recent data supports further the contention that this is due to shorter beam fronts at higher pressures. Table IV gives $\partial I_{net}/\partial t$ at the beam front ($\propto E_z$) and the breakdown time t_b at 10 and 49 cm from the anode for each of five pressures.

TABLE IV

CURRENT RISE AND BREAKDOWN TIMES

Guide Length	0.31T		0.5T		0.755T		1.0T		1.85T	
	dI/dt kA/nsec	t_b nsec	dI/dt kA/nsec	t_b nsec	dI/dt kA/nsec	t_b nsec	dI/dt kA/nsec	t_b nsec	dI/dt kA/nsec	t_b nsec
10 cm	6.14	7.0	6.75	4.0	3.34	2.6	3.92	2.5	~4.17	~.66
49 cm	2.38	6.5	2.1	3.7	2.16	2.15	4.91	3.0	~6.45	~2.0

Beam energy loss due to radial blowoff caused by electrostatic fields at the extreme beam front and due to E_z is calculable. At a particular pressure, a tangent to the beam front z versus t curve can

be drawn from the origin; this line is the z versus t curve of the beam front if radial blowoff and longitudinal deceleration can be avoided. At a given distance, time delay caused by these processes can be read. Primary current waveforms have been measured at various positions; hence, the size as well as duration of the lost beam front current can be reconstructed, and together with voltage monitor records, the corresponding energy loss can be estimated.

At 0.75 Torr this calculation gives an upper estimate of 10 calories of beam front energy lost as the beam front travels from 14 to 182 cm from the anode. This is one-seventh the total energy loss observed over this distance. Although this is not a negligible fraction, it points out that beam front loss phenomena are not of prime importance in this pressure regime.

2. Dissipative Energy Loss Due to Finite Plasma Conductivity ($\vec{J} \cdot \vec{E}$ loss)

The resistive energy loss in the plasma can be calculated readily. Measurements of the exponential decay times of plasma currents with wall shunts give 2500 mhos/meter for the plasma conductivity. From primary and net current waveforms at 0.75 Torr, the average plasma current over the beam pulse is ~ 20 kA. The energy dissipated per unit volume per second is $J_{pl}^2/\sigma = 2.57 \times 10^{11}$ joule \cdot M⁻³ \cdot sec⁻¹. For a 1-1/4 in. diameter guide pipe 1 meter long, the total dissipated energy for an 80-nsec pulse is 3.87 cal, negligible compared with the total beam energy of ~ 150 cal at 10 cm from the anode, at 0.75 Torr.

3. Energy Radiated Due to Electron Accelerations

Our model of transverse energy containment makes it relevant to estimate the energy which electrons lose in the form of synchrotron

radiation due to radial accelerations near the guide tube wall. Analytical calculations are possible but inferences from our beam timing data are sufficient to indicate that electrons throughout the bulk of the beam are not observed to decelerate. The z versus t curves for various portions of the beam, with the exception of the beam front, are lines of constant slope, direct evidence that synchrotron radiation losses are small or negligible.

Bremsstrahlung is due to longitudinal deceleration resulting from the induced longitudinal electric fields E_z . This mechanism is well documented, however, and Reference 16 gives 1.661×10^{-3} as the fraction of total electron energy converted to radiation when a 250-keV electron is completely stopped by air. For our case, this is an upper limit and is clearly negligible.

4. Energy Loss Due to Ionization of the Background Gas

The difficult problem of determining the extent of background gas ionization has not been undertaken in this program. The table below shows the energy needed to ionize every atom of nitrogen in a 1-1/4 in. diameter, 50-cm-long beam channel at 0.5 Torr. The table makes it clear that heavy ionization could account for a significant portion of beam energy loss.

<u>Level of Ionization</u>	<u>Total Energy Necessary (cal)</u>
1	8.6
2	25.6
3	53.8
4	99.5
5	157.2

In order to estimate the extent of ionization, the calculation below places a definite upper limit on the number density of secondaries produced.

At 0.75 Torr air, the density of background gas molecules is $\rho = 1.95 \times 10^{16}/\text{cm}^3$, so that the typical distance between molecules is $\rho^{-1/3} = 3.75 \times 10^{-5}$ cm. If this is the distance over which E_z can accelerate secondaries before they are stopped (and then reaccelerated, etc.), we will arrive at an upper limit for the number density of secondaries needed to account for the observed plasma currents.

Assuming that the accelerating field in the beam after breakdown is 100 V/cm (somewhat larger than estimated earlier) the lower bound on the highest energy a plasma electron can reach is $eE_z \rho^{-1/3} = 2.68 \times 10^{-4}$ eV, corresponding to a velocity of 9.71×10^3 m/sec. At 0.75 Torr plasma currents on the order of 20 kA occur within 20 nsec after breakdown, or $J_{pl} = I_{pl}/\pi r_n^2 = 2.9 \times 10^7$ A/m². This yields an upper limit to the secondary electron number density of

$$\frac{J_{pl}}{\text{ev}} = 1.87 \times 10^{16} \text{ electrons/cm}^3$$

and a ratio of secondary electron density to background gas atom density of $n_{pl}/2\rho = 0.48$ (atom number density = 2 molecule number density). We conclude, therefore, that only a small fraction of the gas atoms will undergo multiple ionization, representing a beam energy loss of less than 10 calories.

5. Other Losses

Other losses include the energy of the radio frequency wave generated by the beam and the energy transferred to accelerated ions. No exact estimates have been made of the energy in the r.f. fields but according to the following argument any such radiation would be small. The power radiated by an accelerated electron is

$$P \approx \frac{2}{3} \frac{e^2}{m^2 c^3} \left(\frac{dp}{dt} \right)^2_{\text{linear accelerations}} + \frac{2}{3} \frac{e^2}{m^2 c^3} \gamma^2 \left(\frac{dp}{dt} \right)^2_{\text{circular accelerations}}$$

Circular accelerations dominate the loss. An upper estimate of this contribution can be obtained by assuming that every electron turns constantly with a 0.5-cm radius of curvature. The total energy radiated by all electrons is then < 1.0 erg (2.4×10^{-8} cal).

Estimates of energy transferred to ions (Reference 17) indicate $\approx 0.1\%$ of the beam energy is lost by this process.

6. Loss Due to Electron Transverse Energy

Measurements of the fluence distribution at the anode (Reference 1) indicate that at $\langle E \rangle = 250$ keV, approximately 300 calories are injected into a 1.25-in. diameter guide pipe. However, as Table V shows, at pressures > 0.5 Torr large amounts of this energy are lost before the beam propagates even 10 cm. Primary currents no higher than 75 kA are measured at 10 cm, although injected currents reach 135 kA. Since energy loss from mechanisms other than transverse energy loss probably amounts to no more than 25 calories in a 1-meter-long, 1-1/4-in. diameter pipe, it can not be responsible for these large losses over short distances. Even more gradual losses incurred as the beam moves from 10 to 200 centimeters from the anode are at least half due to transverse energy loss, as seen in previously reported beam transport curves, reproduced here in Figures 14 and 15. The process of transverse loss may now be described.

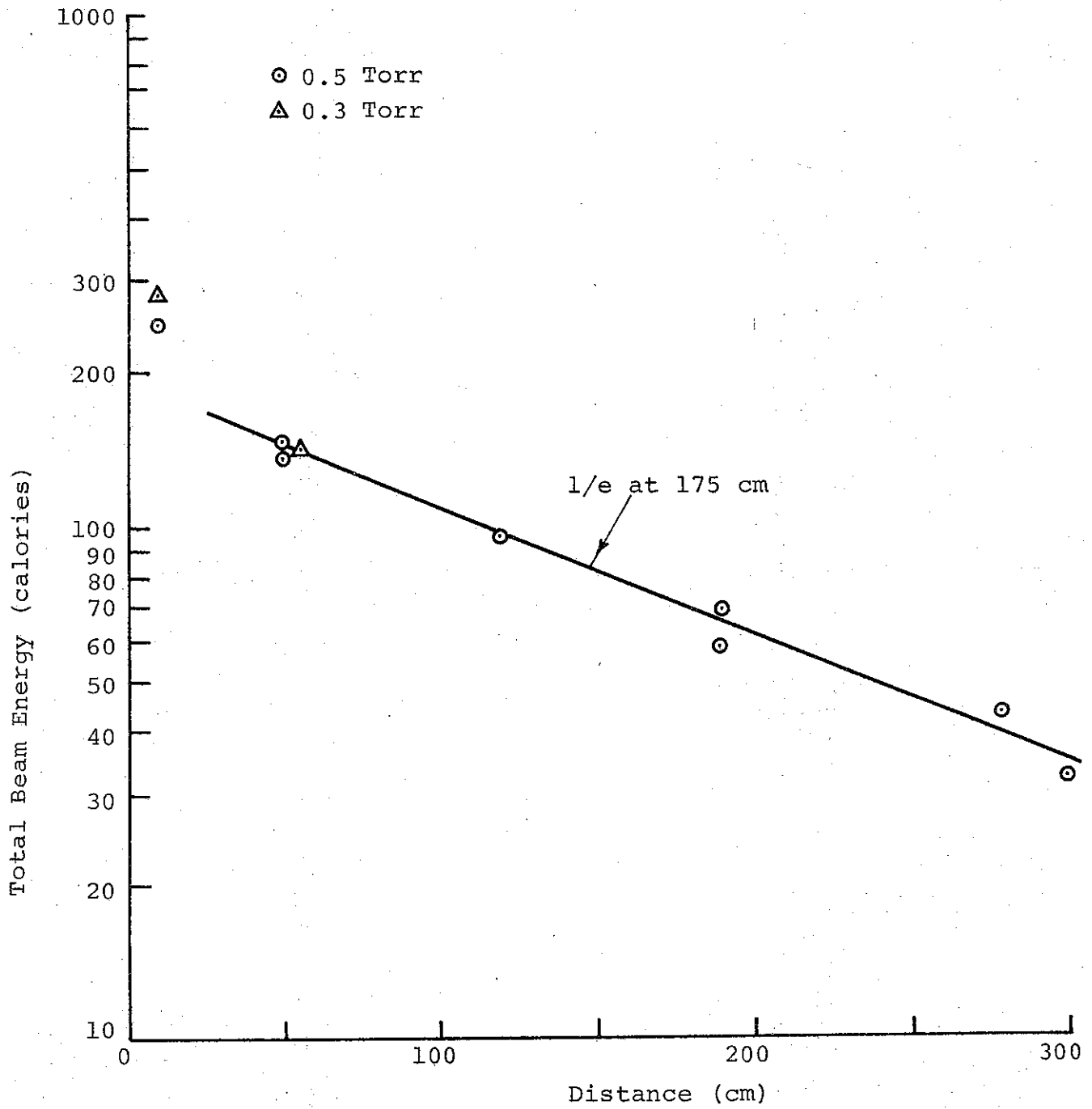


FIGURE 14. TOTAL CALORIES VERSUS PATH LENGTH IN 1-1/4-in. PIPE (0.5 and 0.3 Torr ~ 350 keV)

5805

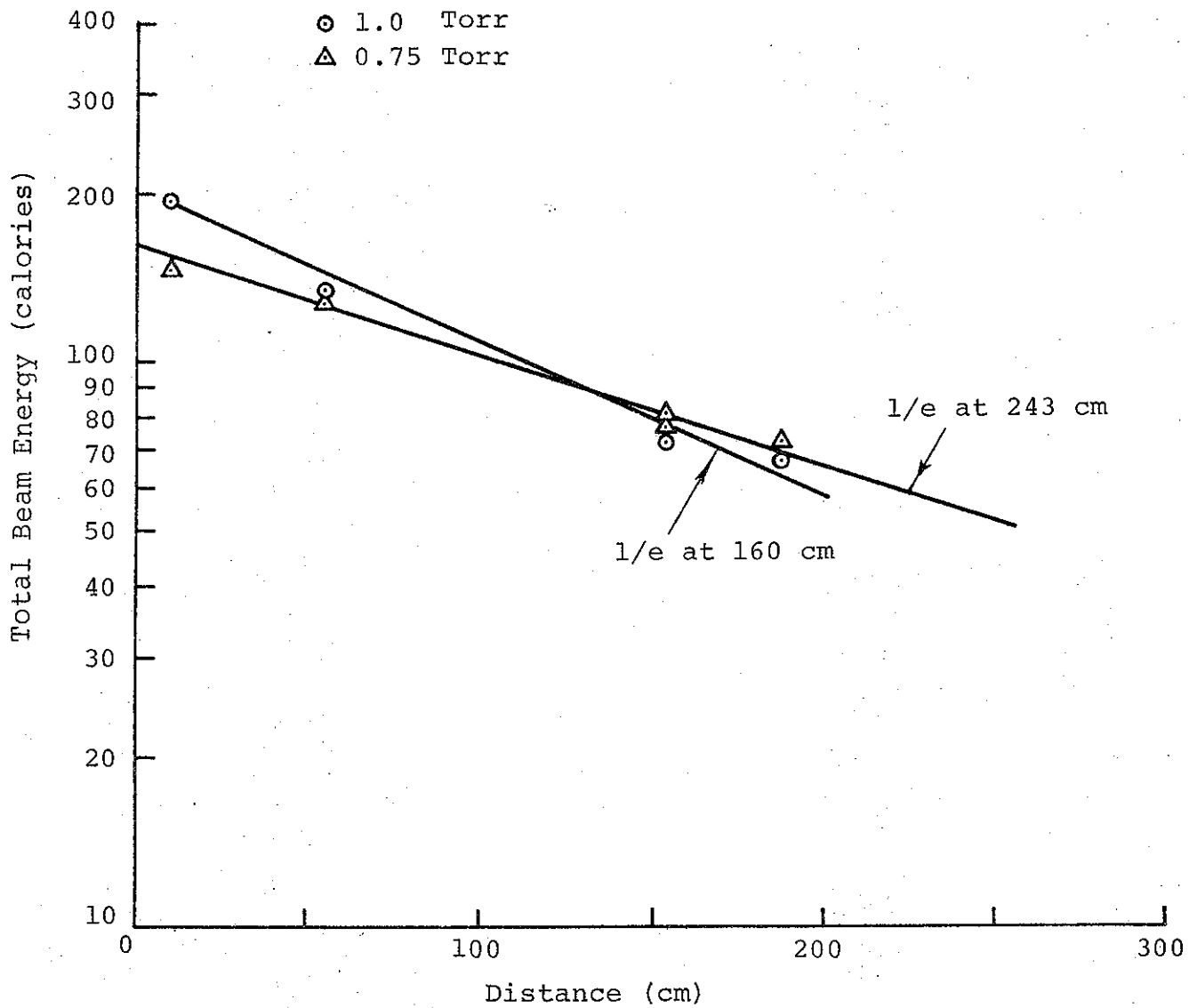


FIGURE 15. TOTAL CALORIES VERSUS PATH LENGTH IN
 1-1/4-in. PIPE (0.75 AND 1.0 Torr ~ 250 keV)

TABLE V
CORRELATION BETWEEN NET CURRENT AND
EARLY LOSS FOR VARIOUS PRESSURES

Pressure (Torr)	Beam Energy Injected (calories)	Beam Energy at 10 cm (calories)	Net Current at Breakdown, 10 cm (kAmps)	Beam Energy at 100 cm (calories)
0.3	≈ 300	282	43	~ 66
0.5	300	249	32	106
0.75	300	143	13	103
1.0	300	196	15	108

The beam transverse energy comes from two sources, transverse motion generated by magnetic collapse of the beam in the diode and transverse motion created by beam self-pinch in the drift chamber. As mentioned in part C of this section, containment of a high transverse temperature beam requires a high net beam current. The degree of net current in the beam channel is effectively frozen at the value of primary current existing at the gas breakdown time. Thus if I_{net} is limited to a low value by rapid gas breakdown (in this case, at pressures > 0.5 Torr) high transverse temperature portions of the beam, injected at later times, cannot be contained and are lost to the guide pipe walls. This loss should be greatest at the pressure which gives the lowest net current, 0.75 Torr. Table V clearly shows the large short-length energy loss which occurs at this pressure and indicates more efficient containment at 0.3 Torr where large net currents are measured.

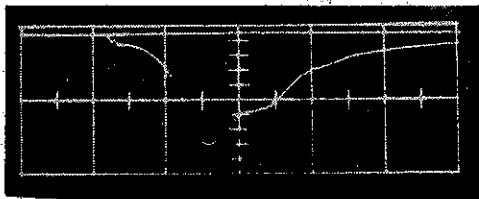
In addition, the changes observed in primary current waveform suggest that transverse energy loss depends on the value of net current. A consistent early time difference between

primary currents at 0.5 and 0.75 Torr, 10 cm from the anode, has been noted (Reference 2). These waveforms are presented in Figure 16. At the higher pressure (0.75 Torr), significantly more primary beam degradation has occurred early in the beam. Corresponding net current measurements (Figure 17, 18, 19) show that the net current (and hence the magnetic field which contains transverse energy) is lower at 0.75 Torr than at 0.5 Torr.

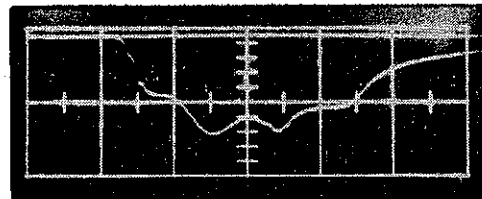
At distances greater than 10 cm transverse energy loss is sharply reduced because most of the high-energy transverse components have already escaped, though the loss of transverse energy is still relatively important. Because of the loss at short lengths of high transverse energy components, the beam quickly comes close to attaining transverse equilibrium, with the containment level set by the existing net current-magnetic field configuration. However, the early pressure-dependent loss of significant numbers of electrons due to transverse energy changes both the net current density and the electron transverse energy spectrum. Thus both the magnetic field and the transverse pressure can undergo continual change and re-adjustment as the beam propagates.

More importantly, the beam front changes as it propagates, resulting in the continual change at the value of the net current at breakdown.* This causes the level of the entire net current waveform to vary in a complex manner as the beam propagates. Figures 17 through 21 show simultaneously monitored net current waveforms at 10, 49, 98, and 182 cm for various pressures.

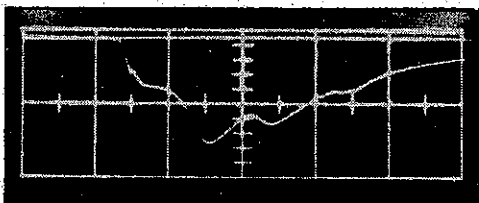
* As the beam propagates $\partial I_{pr}/\partial t$ ($\partial I_{pr}/\partial t = \partial I_{net}/\partial t$ before breakdown) changes. This has already been documented in the section on energy loss due to E_z , so that the field which initiates breakdown changes. Hence the time t_b needed for breakdown to occur also varies with distance. Since t_b is not simply related to $\partial I_{net}/\partial t$, the value of I_{net} at breakdown fluctuates also.



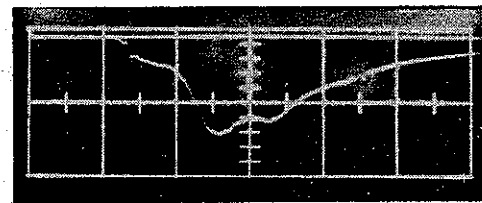
0.75 Torr



0.5 Torr



0.5 Torr



0.75 Torr

FIGURE 16. PRIMARY ELECTRON BEAM CURRENT WAVEFORMS MEASURED WITH FARADAY CUP 14 CM FROM ANODE (Vertical Scales are 57.8 kA/div, Horizontal Scales are 20 nsec/div.)

Time-axis phasing of the curves is such that for each waveform the interval from $t = 0$ to the curve's starting point is the amount of beam front that has been lost. Hence, the manner in which the net current changes at a point fixed in the beam frame can be seen by comparing the intersections of the curves with a line $t = \text{constant}$.

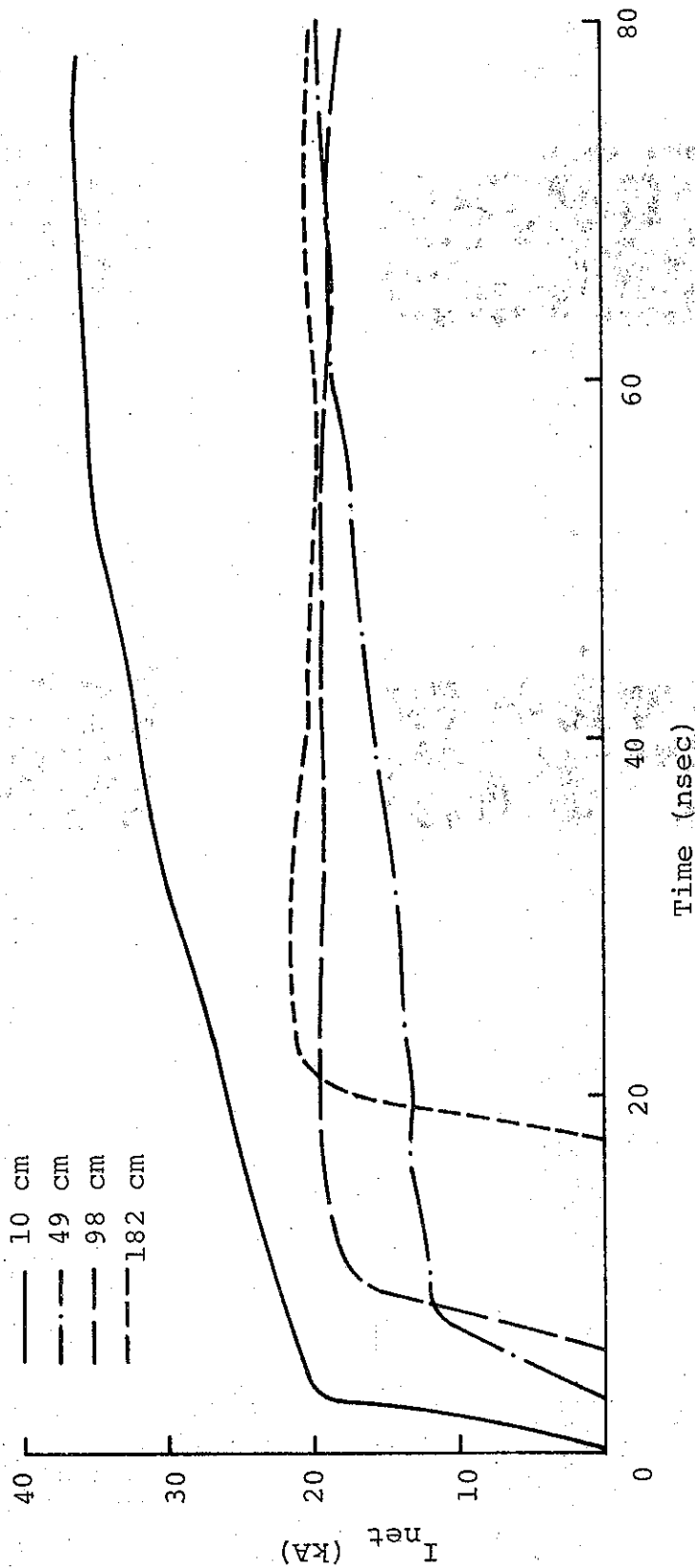


FIGURE 17. I_{net} VERSUS TIME AT VARIOUS DISTANCES IN 1-1/4-in. GUIDE PIPE 0.5 Torr, $\langle E \rangle = 321$ keV SIMULTANEOUSLY MONITORED WAVEFORMS

7551

Time-axis phasing of the curves is such that for each waveform the interval from $t = 0$ to the curve's starting point is the amount of beam front that has been lost. Hence, the manner in which the net current changes at a point fixed in the beam frame can be seen by comparing the intersections of the curves with a line $t = \text{constant}$.

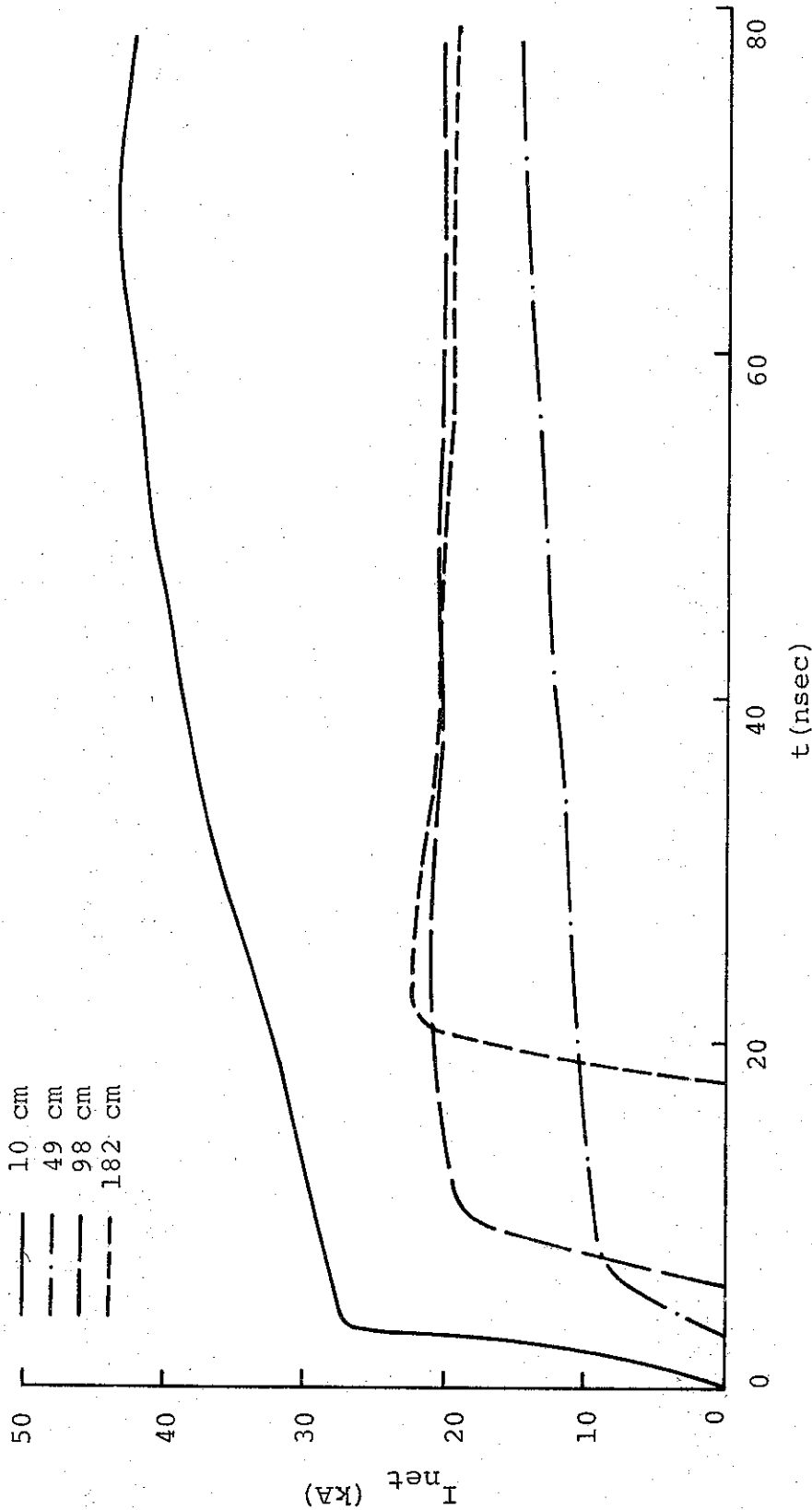


FIGURE 18. I_{net} VERSUS TIME AT VARIOUS DISTANCES IN 1-1/4-in. GUIDE PIPE 0.5 Torr, $\langle E \rangle = 266$ keV SIMULTANEOUSLY MONITORED WAVEFORMS

Time-axis phasing of the curves is such that for each waveform the interval from $t = 0$ to the curve's starting point is the amount of beam front that has been lost. Hence, the manner in which the net current changes at a point fixed in the beam frame can be seen by comparing the intersections of the curves with a line $t = \text{constant}$.

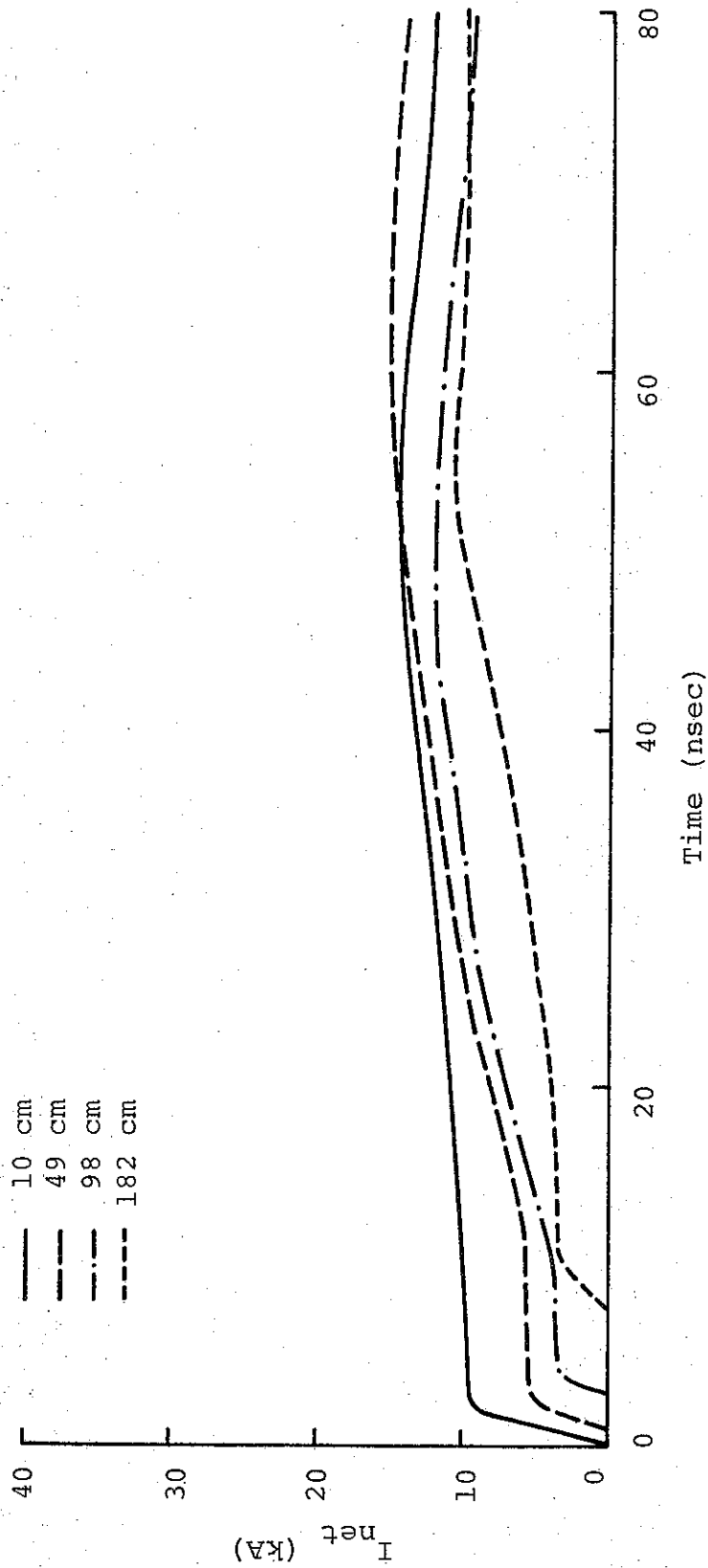


FIGURE 19. I_{net} VERSUS TIME AT VARIOUS DISTANCES IN 1-1/4-in. GUIDE PIPE 0.755 Torr, $\langle E \rangle = 221$ keV SIMULTANEOUSLY MONITORED WAVEFORMS

Time-axis phasing of the curves is such that for each waveform the interval from $t = 0$ to the curve's starting point is the amount of beam front that has been lost. Hence, the manner in which the net current changes at a point fixed in the beam frame can be seen by comparing the intersections of the curves with a line $t = \text{constant}$.

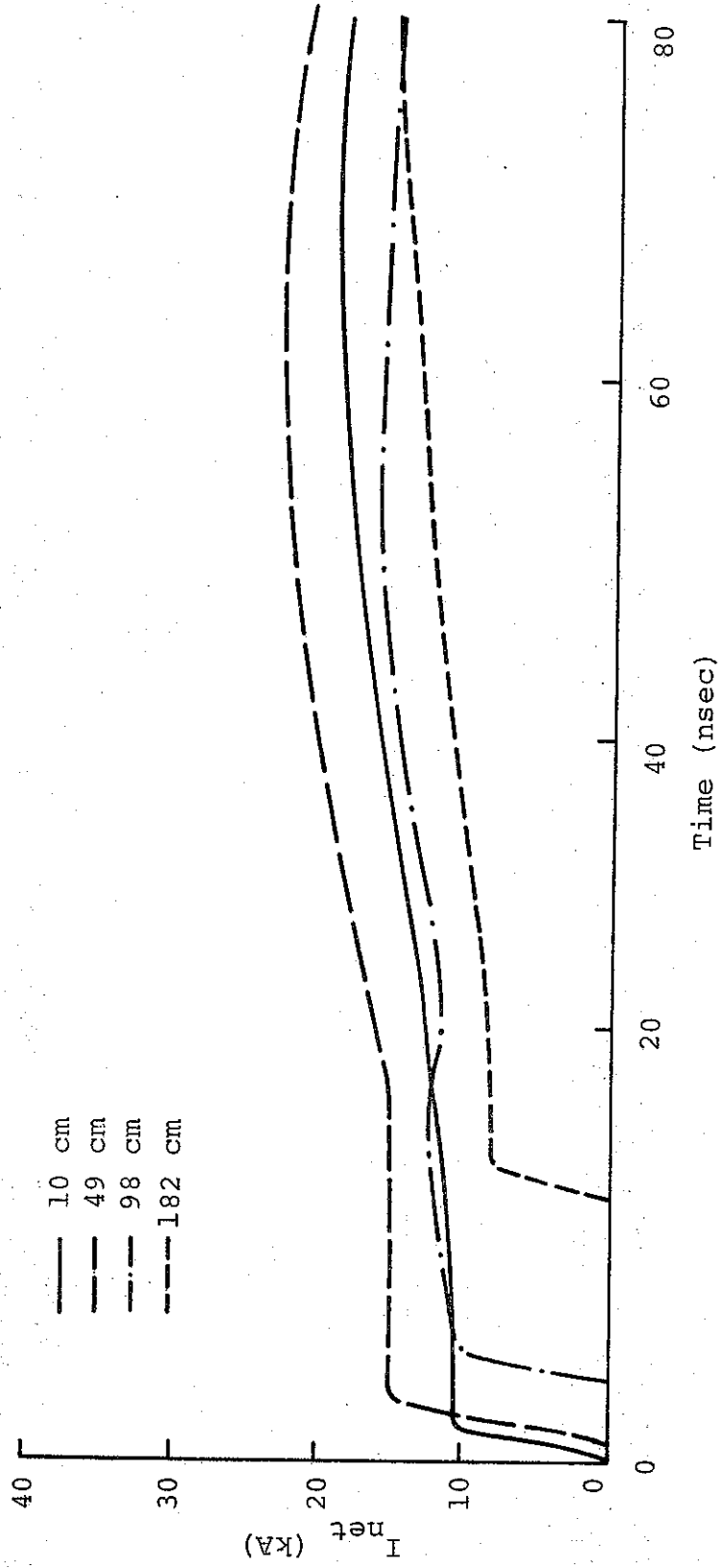


FIGURE 20. I_{net} VERSUS TIME AT VARIOUS DISTANCES IN 1-1/4-in. GUIDE PIPE 1.0 Torr, $\langle E \rangle = 243$ keV SIMULTANEOUSLY MONITORED WAVEFORMS

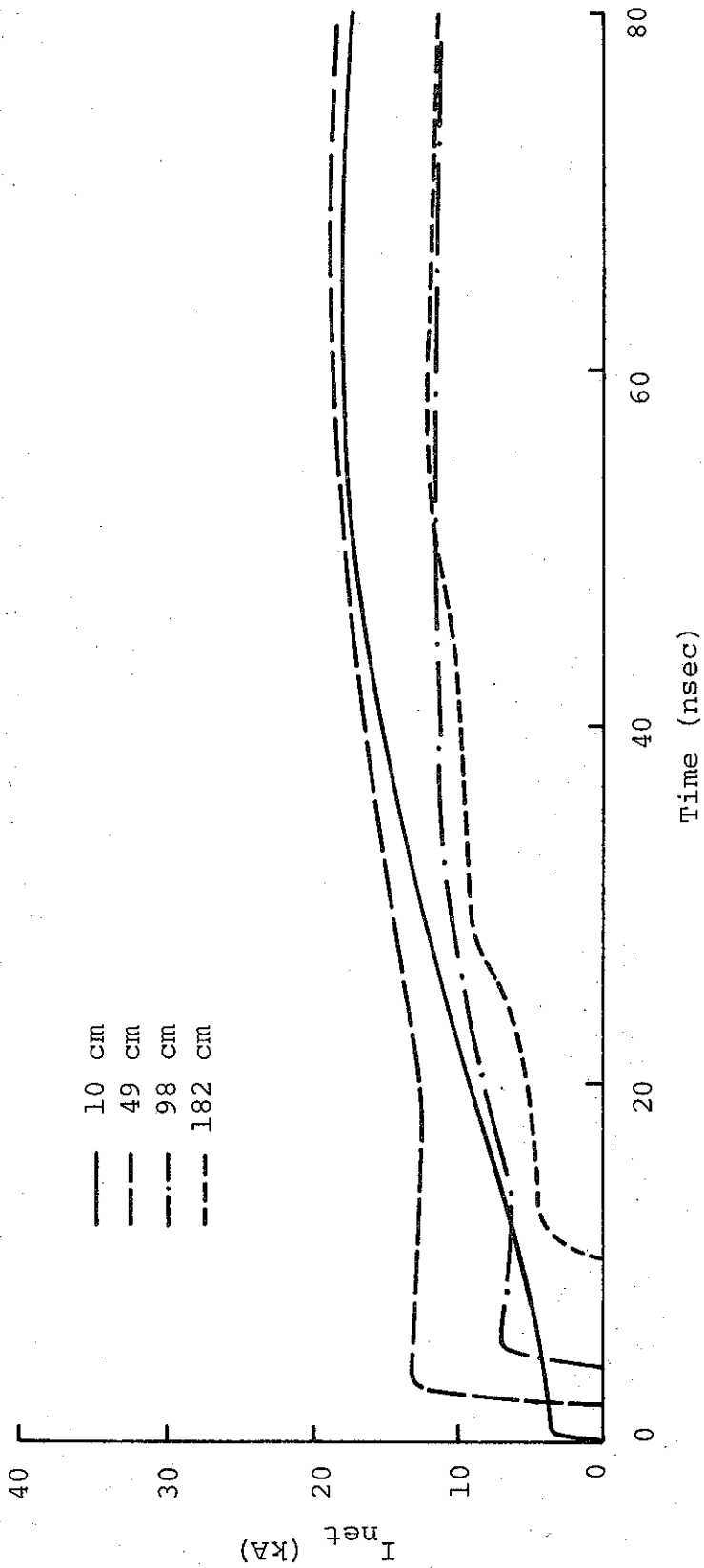


FIGURE 21. I_{net} VERSUS TIME AT VARIOUS DISTANCES IN 1-1/4-in. GUIDE PIPE 1.85 Torr, $\langle E \rangle = 217$ keV SIMULTANEOUSLY MONITORED WAVEFORMS

Because of the continual variation of net current level, equilibrium may never be reached for transverse energy containment, with the containing magnetic fields changing independently of local transverse energy (although transverse loss may be zero at moments when the "correct" field exists). Hence, electrons can be lost to the walls continuously.

Although an analytical treatment has not been undertaken because of the complexity of the problem, three independent types of experimental data support these ideas. Already cited here (and in Reference 2) is the comparison between primary current waveforms at 10 cm at 0.5 and 0.75 Torr (Figure 16). Transmission measurements at 12 cm are also reported in Reference 2 (pp. 48-51). These indicate the lower mean path angle for electrons traveling in the beam at 0.75 Torr as compared with 0.5 Torr, leading to the inference that in traveling 12 cm, less transverse energy remains at 0.75 Torr than at 0.5 Torr. This is because the fields associated with the beam at the higher pressure are relatively less capable of containing transverse energy. Finally, net current waveforms recently obtained (Figures 17-21) show characteristic differences in waveform at the different pressures. That these differences are, in fact, characteristic of pressure is apparent from the reproducibility of waveform shape at equal distances for the two 0.5 Torr shots. This supports our contentions that net current levels change in a complex manner as the beam propagates, and that the pattern of these changes is due to the gas pressure, i.e., to the specifics of the beam-plasma interaction.

The compatibility of these ideas with the measured transport curves is demonstrated in Figures 14 and 15. These curves are represented as exponentials, which are straight lines on the semi-log graphs. It is important to note that since the number

of data points is small and the spacing of the points is coarse, statistical variation in the data rules out the possibility of detecting structure in the curves. It is expected that an appropriately large number of data points would reveal structure, which could be compared directly with data such as in Figures 17 through 21 to give a firm experimental foundation to the ideas presented here.

E. NEW DATA AND INTERPRETATION

In addition to the ion-detection work and multiple cathode study discussed in Section IV and V, data generated since publication of the interim report (Reference 2) concerns the net and primary current waveforms at different transport lengths in a 1-1/4-in. copper guide pipe. The data, given in Figures 22 and 23, cover several values of energy and v/γ at injection and a range of pressures from 250 μ to 1.85 Torr. The waveforms for each shot were monitored simultaneously.

1. Current Neutralization

Breakdown time data for air were presented in Figure 3 at 10 cm from the anode and were in fair agreement with pulsed-dc breakdown studies. At longer lengths, however, breakdown occurs more rapidly. Figure 24 shows this behavior at 0.75 Torr, where we see greater departure from the Felsenthal and Proud curve at greater transport lengths. This trend suggests that some ionization of the background gas at long lengths may occur prior to beam front arrival, resulting in a decreased breakdown time. Possible causes of such pre-ionization include the effects of rf fields, recombination light, and de-excitation emission. These travel at the speed of light and at sufficient distances from the anode can ionize the background gas prior to the arrival of the electron beam. This hypothesis could be partially tested by comparing net current waveforms for shots with and without thin aluminized mylar

R8031

TYPICAL PRIMARY CURRENT AT 0 cm:

$\langle E \rangle \approx 550 \text{ keV}, v/\gamma \approx 5$



$\sim 97 \text{ kA/cm}$

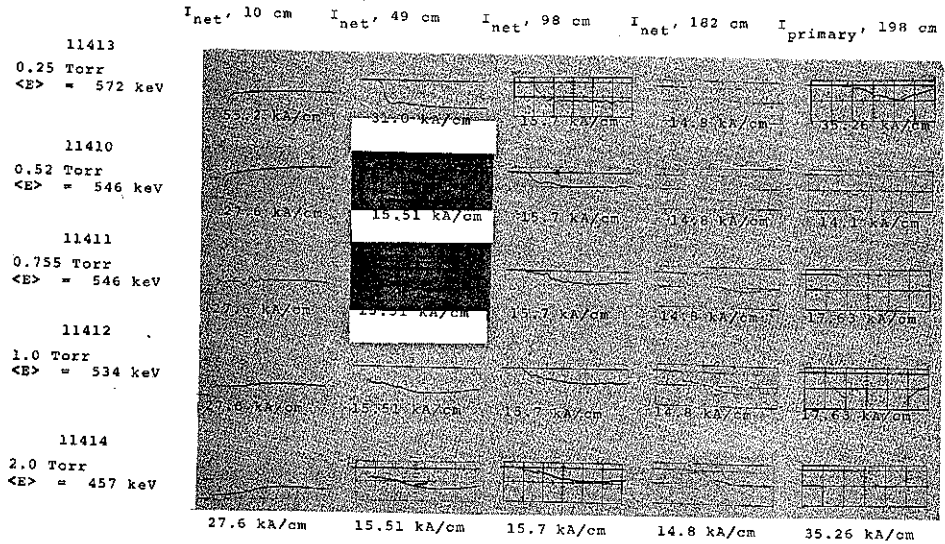


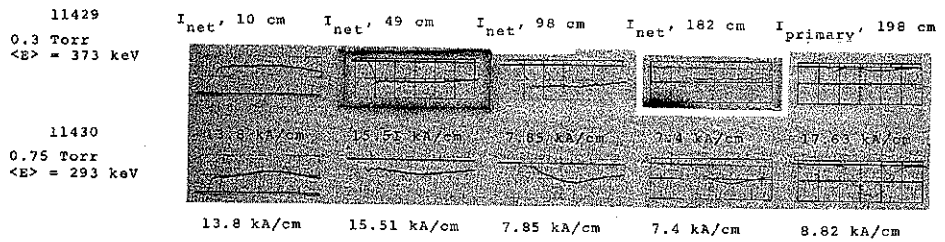
FIGURE 22. NET AND PRIMARY CURRENT WAVEFORMS

TYPICAL PRIMARY CURRENT AT 0 cm:

$\langle E \rangle \approx 350 \text{ keV}, v/\gamma \approx 2$



$\sim 120 \text{ kA/cm}$

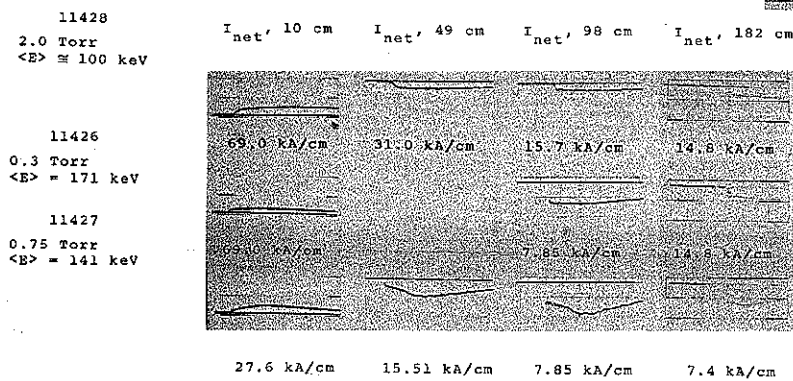


TYPICAL PRIMARY CURRENT AT 0 cm:

$\langle E \rangle < 200 \text{ keV}, v/\gamma \approx 17$



$\sim 169 \text{ kA/cm}$



NET AND PRIMARY CURRENT WAVEFORMS,
SIMULTANEOUSLY MONITORED FOR EACH SHOT

$\langle E \rangle \approx 250 \text{ keV}$, $v/\gamma \approx 12$

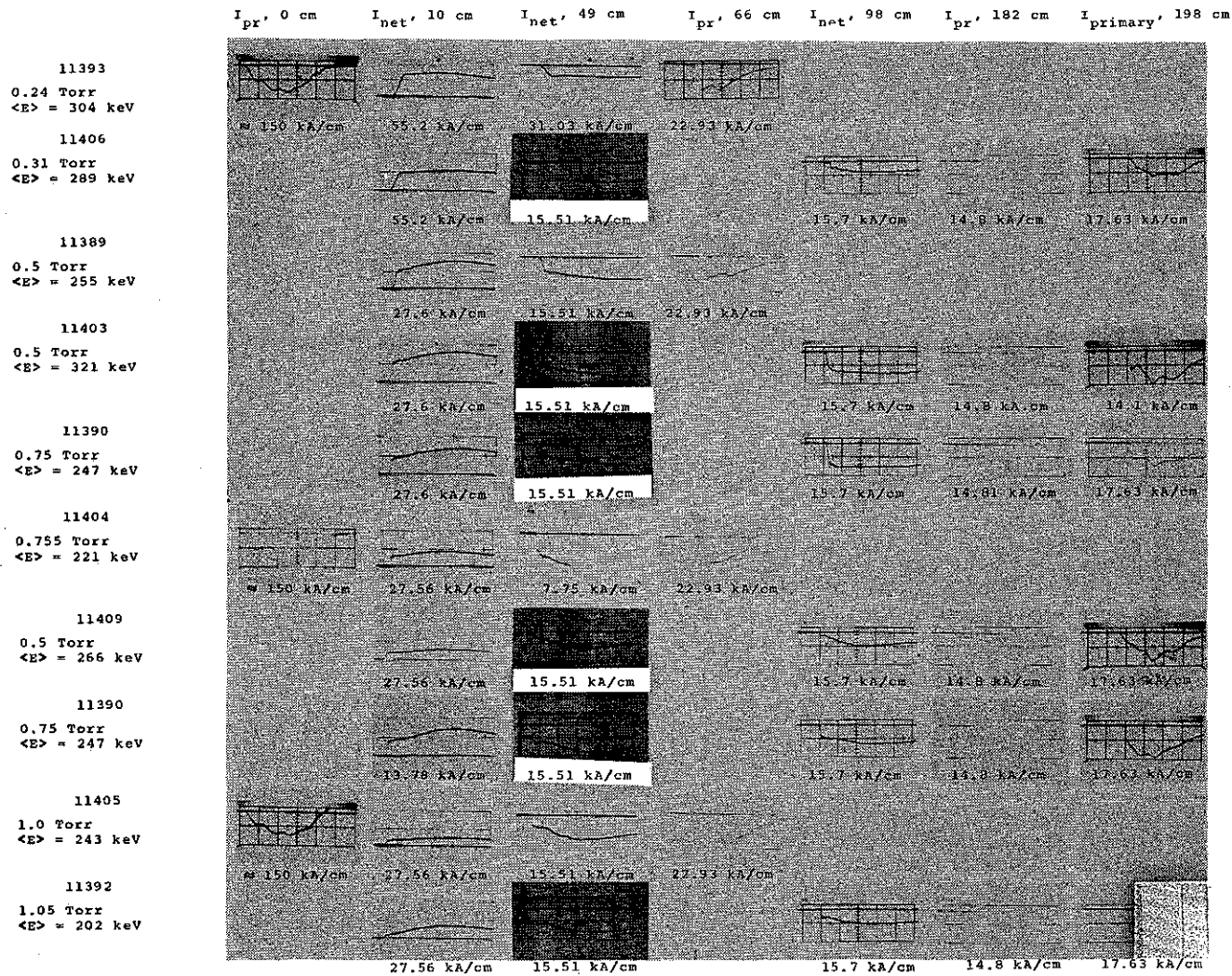


FIGURE 23. NET AND PRIMARY CURRENT WAVEFORMS

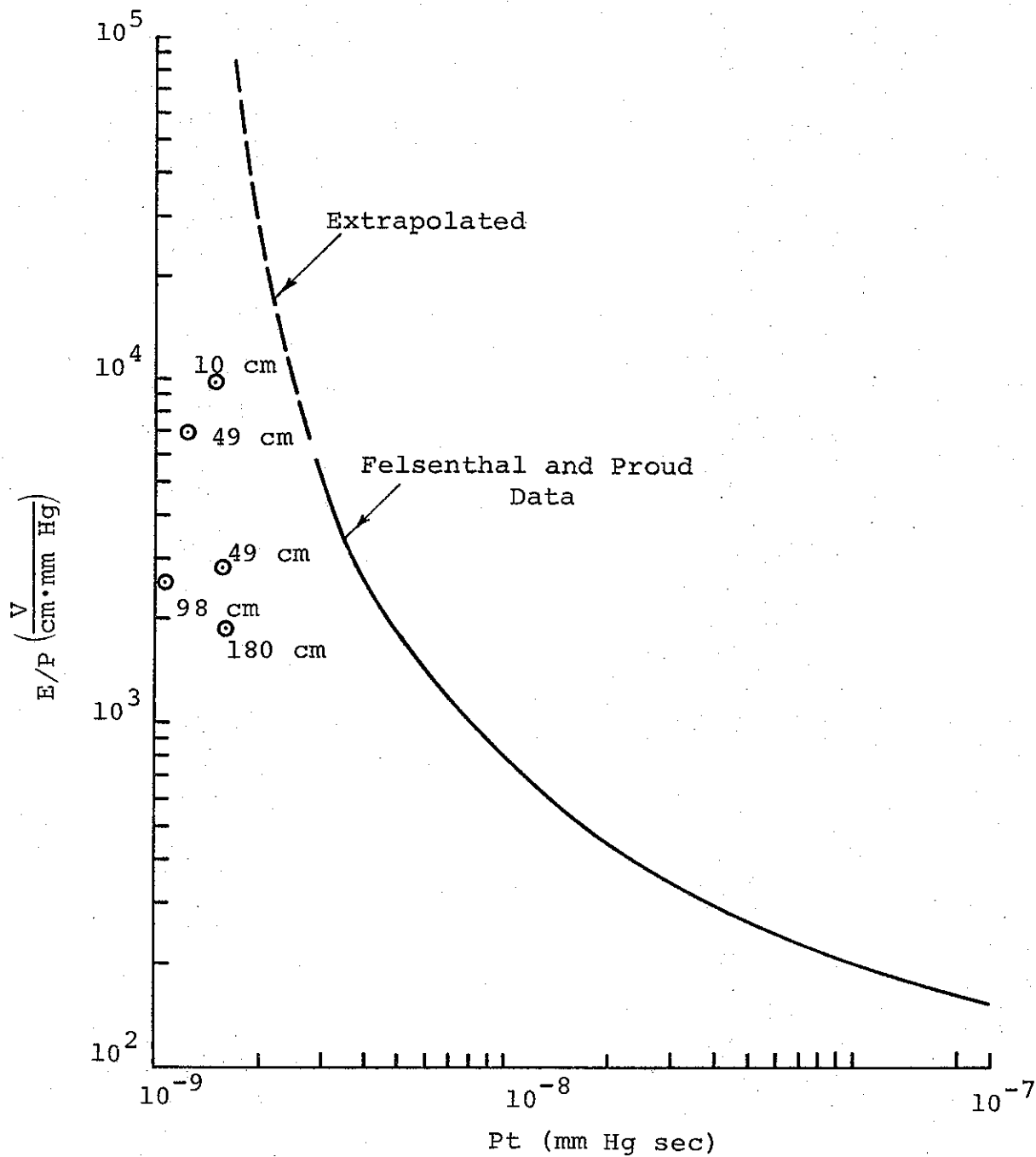


FIGURE 24. BREAKDOWN DATA AT DIFFERENT LENGTHS 0.75 Torr

diaphragms placed at intervals along the guide pipe. Another interesting observation is the late onset of current neutralization seen occasionally at long transport lengths (e.g., Shot 11411 in Figure 23). This, of course, occurs only when E_z is not high enough to cause avalanche breakdown at early times.

The overall waveform reproducibility of the net current data is quite good, as seen by comparing the corresponding waveforms of Shots 11389, 11403, and 11409 in Figure 22. As suggested in part A of this section, net current waveforms assume more nearly constant values after breakdown at lower pressures (Shots 11393 and 11406). Data indicate that parameters such as dI/dt at the beam front, t_b , and $I_{net}(t_b)$ change as a function of transport length. Section D employs these observations to account qualitatively for the continual loss of transverse energy components in the beam.

2. Timing Measurements

The simultaneous monitoring of net and primary current waveforms (Figures 17 and 18) permitted more refined measurements of beam front distance versus time. These records are presented in Figures 25 through 32. The graphs agree fairly well with the relevant curves presented in Reference 2; in making the comparison, it should be noted that each of those curves was generated with one data point per shot, while each of the present curves was measured with one shot.

Of the interesting features arising from these new data, most obvious is the fact that the curves do not intercept the time axis at the same point.* However, the discussion in part A

* Zero time, $t = 0$, is measured in each graph from the time at which that shot's voltage monitor record shows voltage turn-on. This is not necessarily the moment of current initiation. Hence, we would not expect the z versus t curves to intercept the t -axis at $t = 0$.

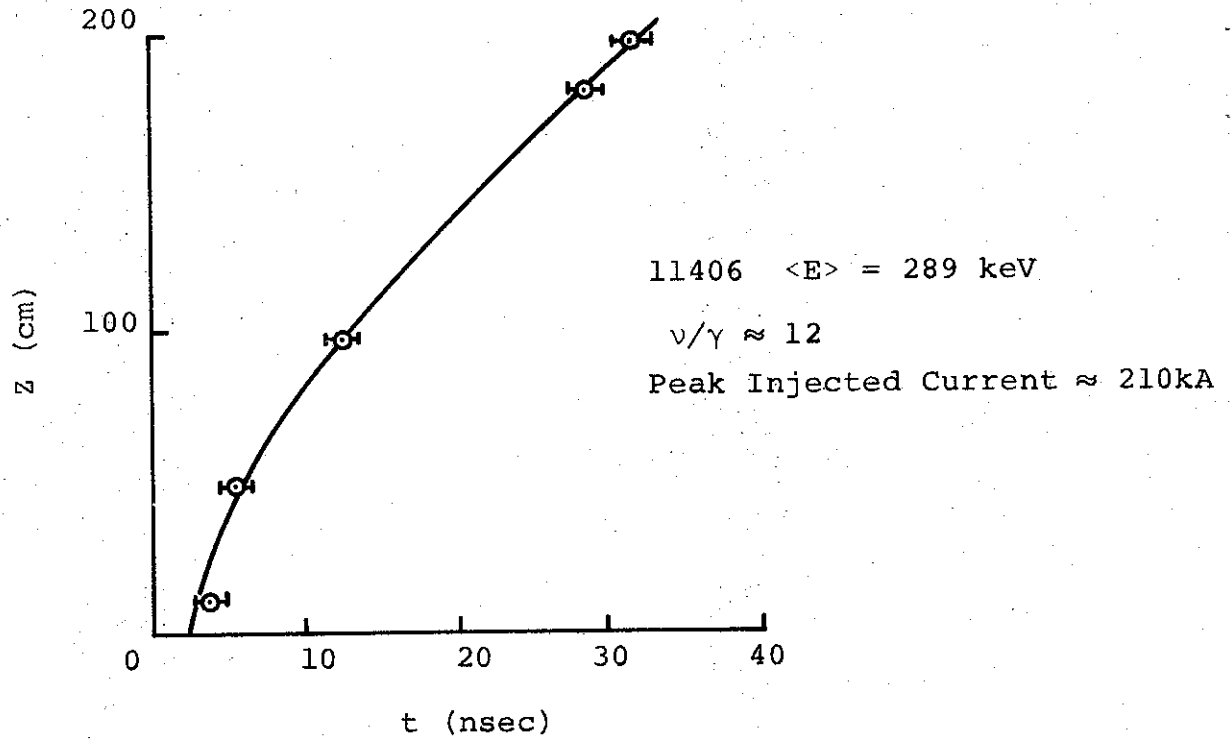


FIGURE 25. BEAM FRONT DISTANCE VERSUS TIME, 0.31 Torr

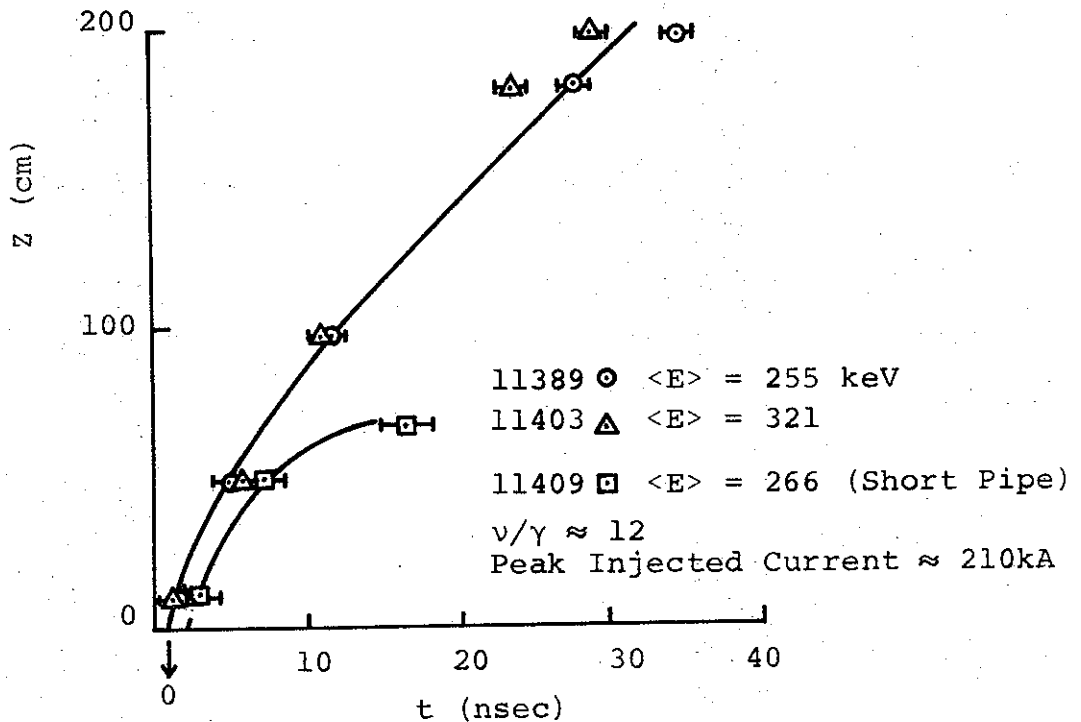


FIGURE 26. BEAM FRONT DISTANCE VERSUS TIME, 0.5 Torr

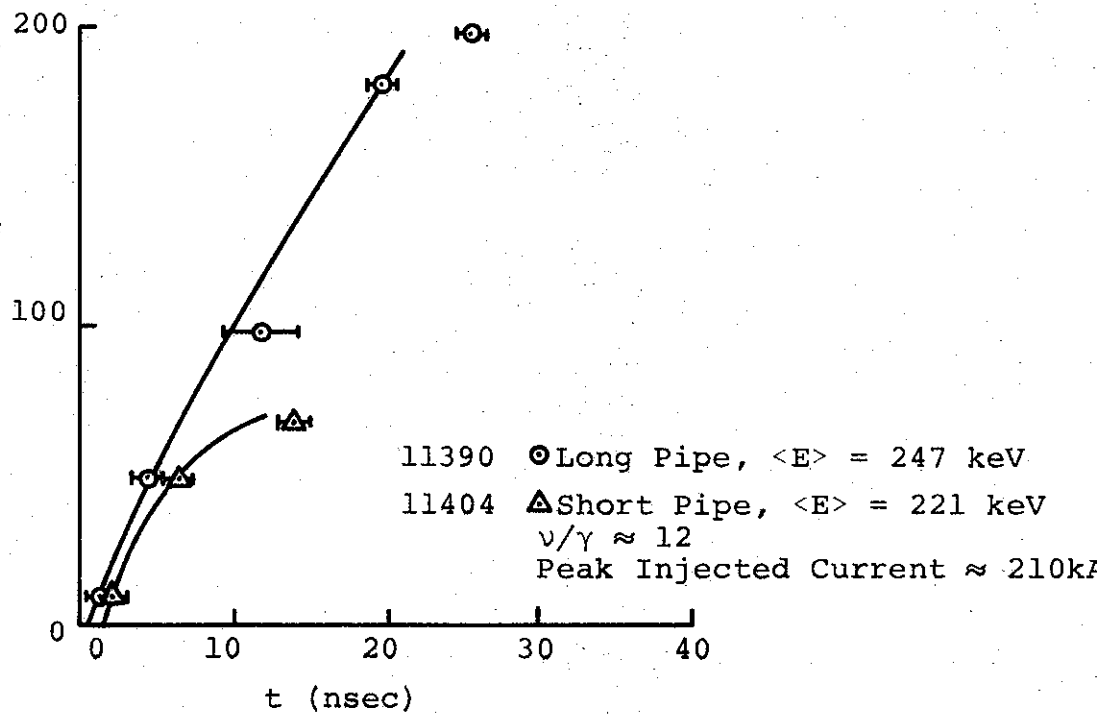


FIGURE 27. BEAM FRONT DISTANCE VERSUS TIME, 0.755 Torr

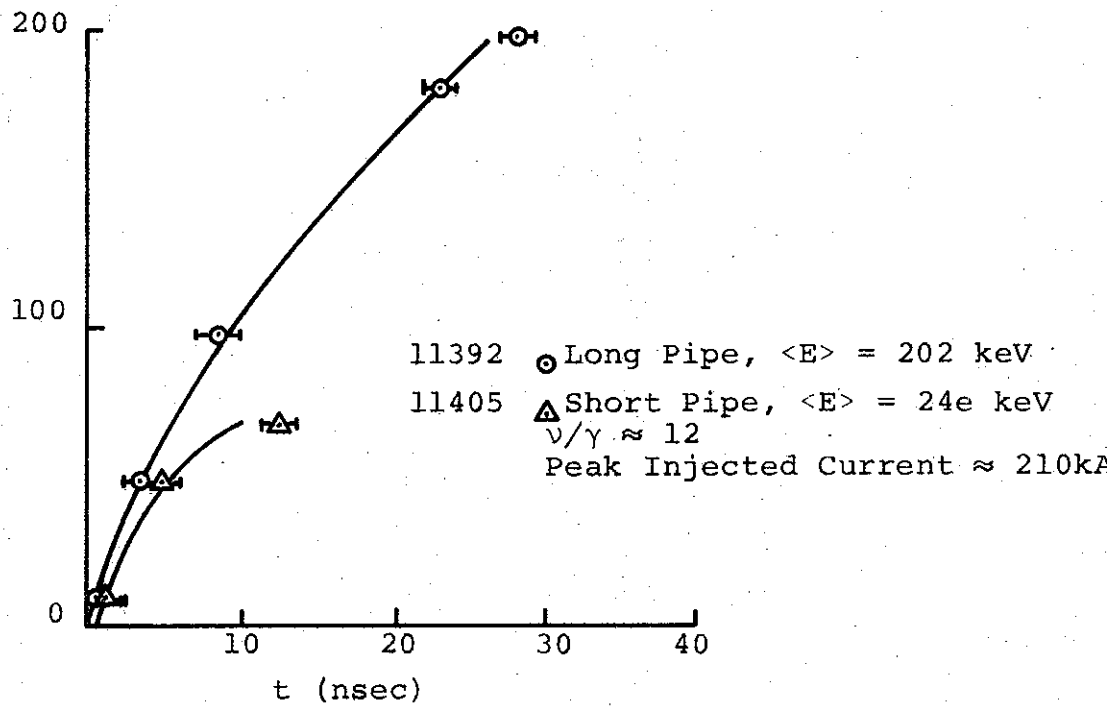


FIGURE 28. BEAM FRONT DISTANCE VERSUS TIME, 1.0 Torr

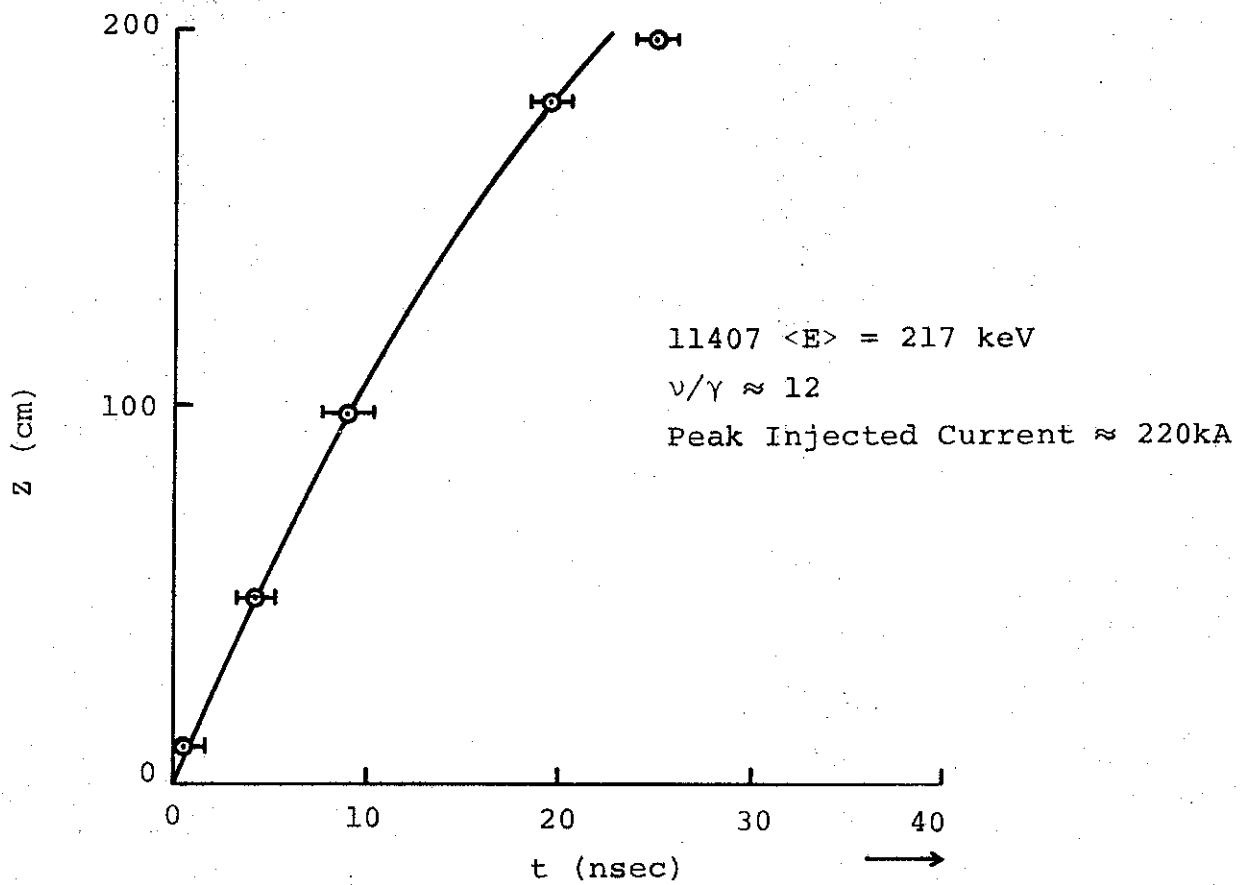


FIGURE 29 . BEAM FRONT DISTANCE VERSUS TIME

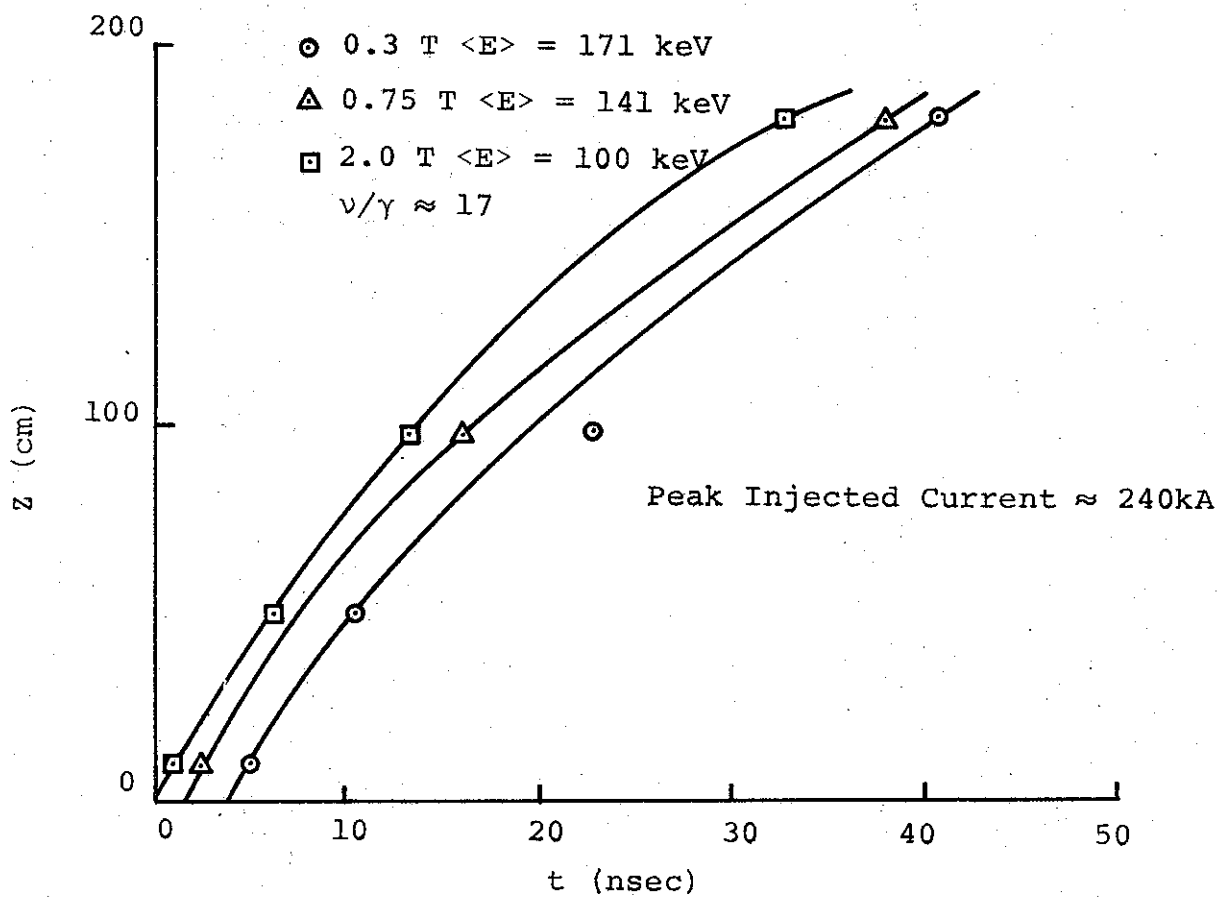


FIGURE 30. BEAM FRONT DISTANCE VERSUS TIME

- 0.25 T $\langle E \rangle = 572$ keV $v/\gamma \approx 3$
- △ 0.52 T $\langle E \rangle = 546$ keV
- ◇ 0.755 T $\langle E \rangle = 546$ keV Peak Injected
- 0.99 T $\langle E \rangle = 534$ keV Current ≈ 100 kA
- ▽ 2.0 T $\langle E \rangle = 457$ keV

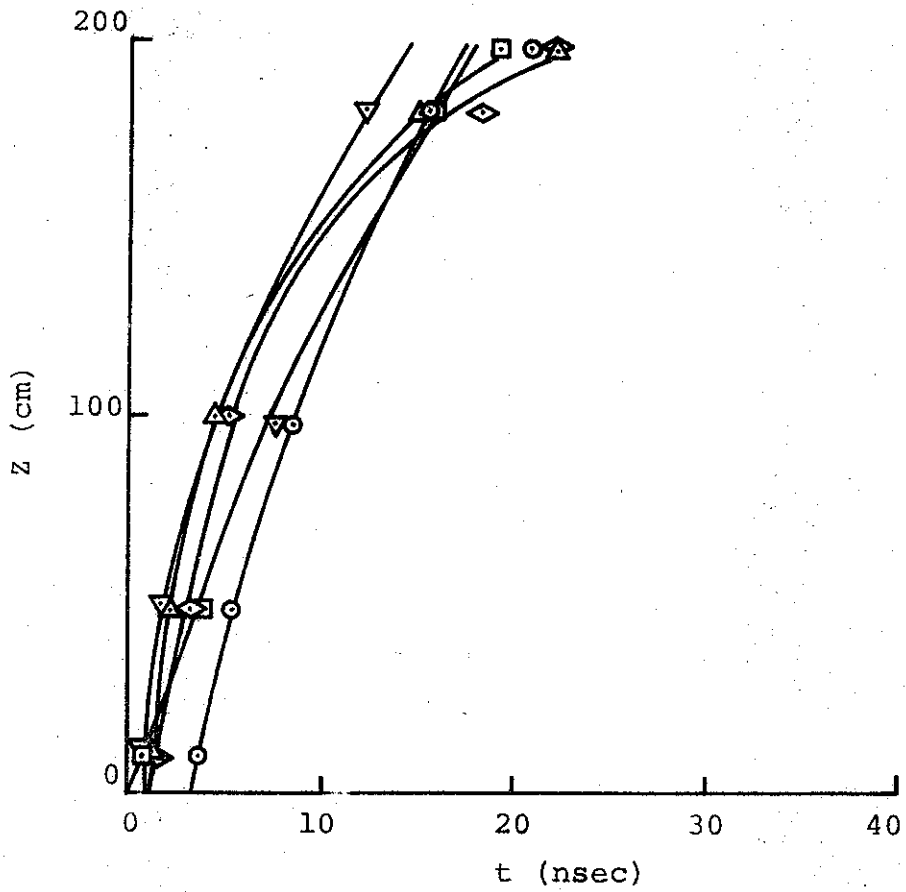


FIGURE 31. BEAM FRONT DISTANCE VERSUS TIME

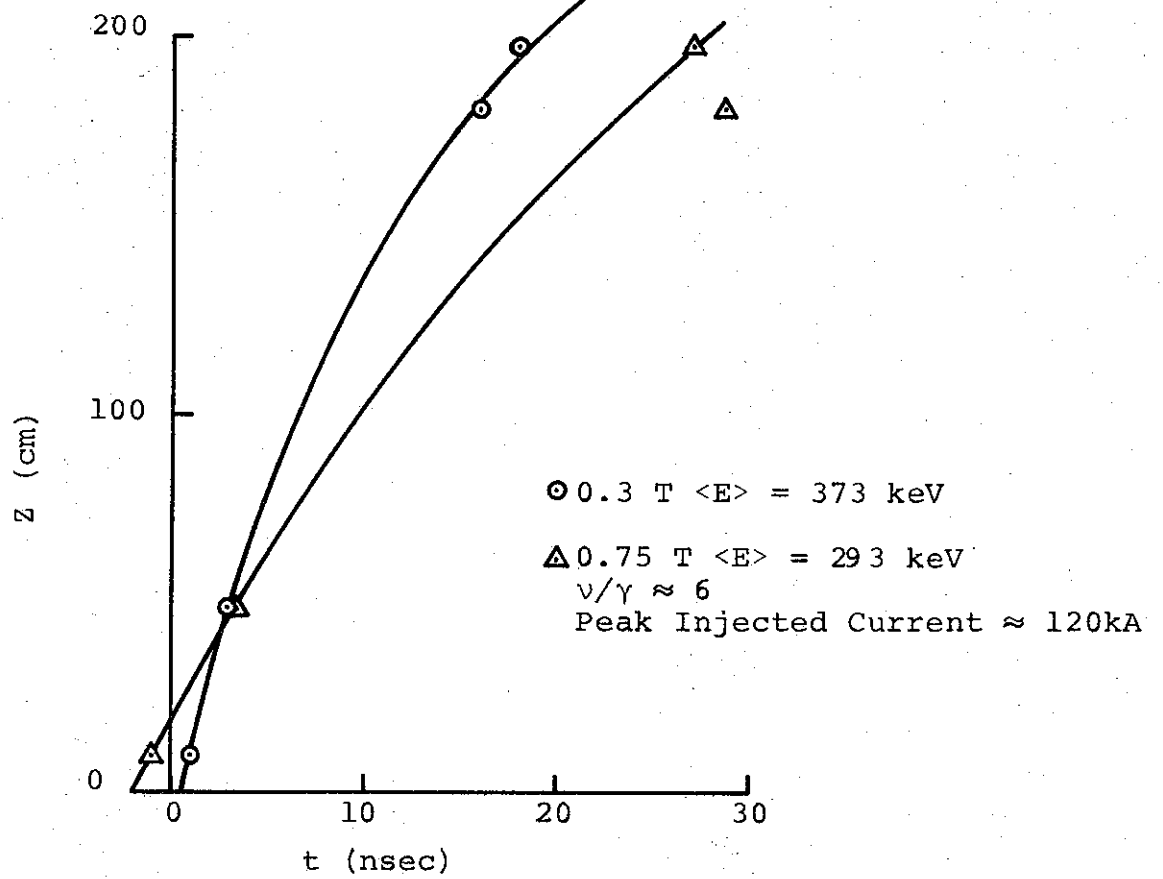


FIGURE 32. BEAM FRONT DISTANCE VERSUS TIME

of this section suggests that delays can be caused by failure of the beam to propagate until charge neutralization is achieved, a process which culminates sooner with increasing pressure. This is precisely the effect demonstrated by these timing curves.

Another aspect of the curves appears to demonstrate the importance of z-axis boundary conditions (end effects). Timing measurements for Shots 11389, 11390, and 11392, in Figures 26, 27, and 28, respectively, were obtained with the beam channel end cap (the Faraday cup) at 66 cm, while the accompanying curves in those figures were obtained with the end cap at 198 cm. The timing curves for short and long guide pipes show a consistent difference, suggesting that the interaction of the beam with its own rf field can be important in a finite-length cavity.

3. Primary Current Degradation with Distance

The discussion in Section D of the relationship between net current and electron loss due to transverse energy can be illustrated qualitatively by some of the net and primary current waveforms of Figure 22.

Consider the waveforms of I_{net} at 182 cm and the corresponding I_{pr} waveforms (at 198 cm) of Shots 11404 and 11409. I_{net} of shot 11409 reaches its maximum value very early in the pulse, requiring less than 5 ns to do so, resulting in a primary current which retains about as many electrons early in the pulse as at later times. Shot 11404, on the other hand, exhibits a relatively low net current early in the pulse. This is reflected in the primary current waveform for the shot, which is considerably degraded at early times, increasing slowly (compared with Shot 11409) to its maximum value.

The measurements presented here demonstrate the complexity of the neutralization process when viewed in detail. They suggest that precursor radiation and end effects play an important role in determining the precise time dependence of the effects. The coupled nature of background gas properties, the electromagnetic fields in the guide geometry, and the modulation of the primary beam has become evident. Although the gross effects that govern energy transport and current neutralization are well understood, the detailed results presented in this subsection present a considerable challenge to future workers in this field.

SECTION IV ION ACCELERATION STUDY

A. GENERAL DISCUSSION

Interest in using the possible collective effects of a high-current relativistic electron stream to accelerate ions has been widespread in the past few years. Initial interest was stimulated by reports of Soviet efforts, principally under Veksler and later by Sarantsev (References 18 and 19). Until recently, the electron ring approach attracted most of the attention both in this country (under the Lawrence Radiation Laboratory's Electron Ring Program) and in the Soviet Union at Dubna. In 1967, however, A.A. Plyutto and others in the Soviet Union reported experiments which suggest an alternative to the electron ring approach (Reference 20). Similar measurements were reported in this country by Graybill and Uglum of Ion Physics (Reference 17). Essentially, these experiments suggest a direct utilization of the electron beam as an acceleration device.

The collective effect processes in general offer attractive economical solutions to the current accelerator cost curves, with interesting possibilities for extremely high energy proton accelerators (in the 1000-GeV region), energetic heavy ion sources for new element production and biophysical studies, and accelerators of the "factory" variety for the copious production of fast neutrons, isotopes, etc. This accounts for the considerable interest in the field.

Collective effect processes in a propagating electron beam are also interesting because of the influences such beam-ion interactions might have on the beam. Furthermore, the accelerated ions may conceivably give information about regions in the beam inaccessible to present diagnostic techniques.

These exciting possibilities prompted the preliminary study reported here. An initial goal was to observe accelerated ions under electron beam conditions differing from either Plyutto, et al, or Graybill and Uglum. With this approach we felt we could better appraise the problems and plan a more extensive study.

Before discussing our work, let us briefly review the results of work by Plyutto et al, and by Graybill and Uglum.

Plyutto et al, reported observing 4 to 5 MeV protons and 15 to 20 MeV carbon ions accelerated by a 200- 300-keV electron beam. The number of protons observed per pulse was about 10^{11} - 10^{12} . The ions were momentum analyzed with a mass spectrometer and it was noted that maximum carbon ion energies apparently did not depend on the multiplicity of the charge.

Graybill and Uglum reported observing 5-MeV protons accelerated by a 1.3-MeV, 40-kA electron beam. Proton flux per pulse was approximately 10^{13} particles. They also reported observing particles with somewhat lower velocities when firing in deuterium, helium and nitrogen gas, equivalent to 5-MeV deuterons, 9-MeV helium ions, and 20-MeV nitrogen ions. The ions were analyzed by time of flight between two Faraday cup positions. In both measurements, the accelerating mechanism was uncertain.

B. EXPERIMENTAL ARRANGEMENT

1. General Description

The primary electron beam used in this experiment was produced by the 730 Pulserad. The electron beam propagated through a gas-filled drift chamber and entered a vacuum region where the electrons

were removed by space charge effects and a sweeping magnet. The ions, with considerably more momentum, continued down the pipe and were detected by Rogowski coils and Faraday screens. Time-of-flight information was then available between two screens.

2. Primary Electron Beam

The primary electron beam usually ran at 600 keV and 150 kA peak tube current. A representative injected current waveform is shown in Figure 33. The diode configuration consisted of a 3-in. outer diameter, 2-in. inner diameter hollow needle cathode, and a 0.00025-in. aluminized mylar anode. Anode-to-cathode spacing was 6 mm with a pressure of 1.8×10^{-4} mm Hg in the diode.

Following transmission through the anode the electron beam was transported 58 cm in a 3-in.-diameter copper pipe in the drift chamber. The pipe was solid except for the last 15 cm which were of copper mesh to allow time-integrated photographs near the vacuum drift region. An open shutter photograph of this region is shown in Figure 34. The beam then passed through a 1.9-cm graphite aperture and entered the vacuum region.

3. Vacuum Drift Region

This area was evacuated with a 15-cm diffusion pump. A sweeping magnet with a nominal $\int B \cdot dl$ of 8 kg/cm was positioned 8 cm behind the entry aperture. The ions, which generally have momenta two orders of magnitude higher than the electron momenta, escape this region only slightly deflected and entered a 3.2-cm-diameter copper pipe maintained at the same pressure. A Rogowski coil and Faraday cup assembly were placed immediately following the magnet with the Faraday cup 10.3 cm behind the coil. Alternatively, a pair of Faraday screens 30 cm apart could be positioned behind the magnet, with the first

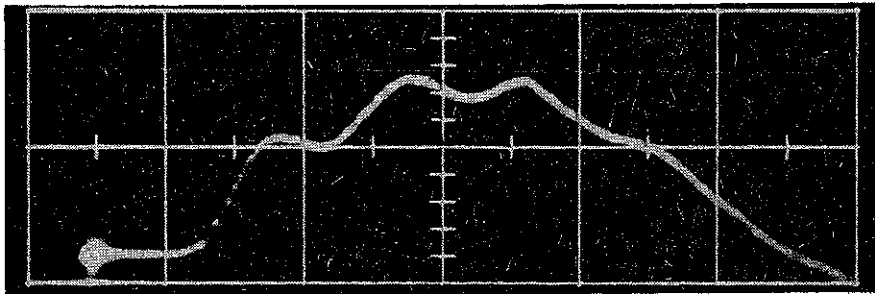


FIGURE 33. PRIMARY ELECTRON BEAM CURRENT WAVEFORM, 120 kA/cm, 20 nsec/cm (This is the Injected Current for the Ion Detection Experiment.)

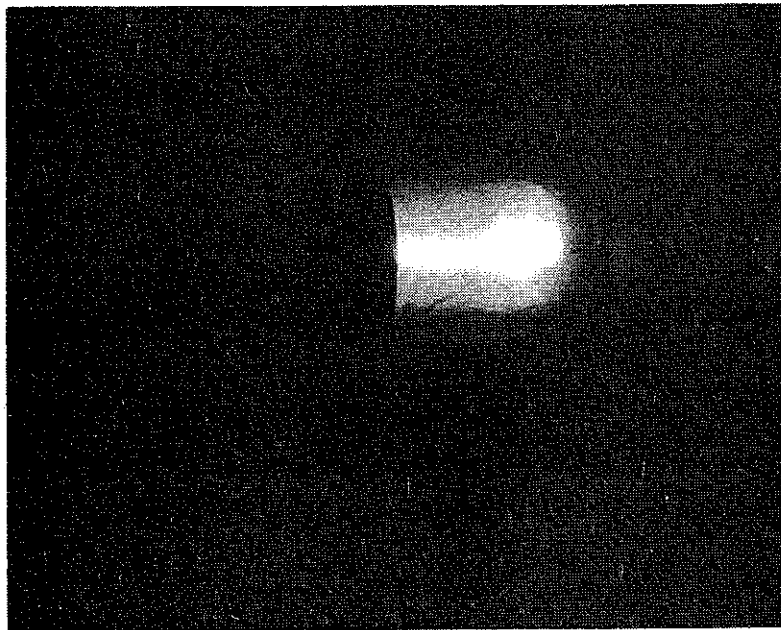


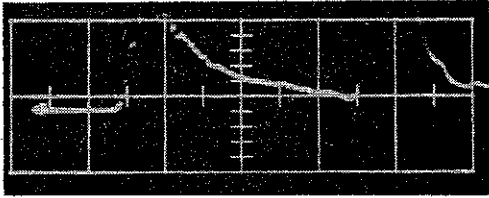
FIGURE 34. OPEN-SHUTTER PHOTOGRAPH OF ELECTRON BEAM ENTERING ION DETECTION APPARATUS. (Propagation is from Left to Right. Drift Chamber Contained Air at 150 μ for this Shot.)

screen 82.5 cm from the anode. The screens were 3.7 cm in diameter and consisted simply of 28 gauge copper mesh, 12 lines/cm. Each screen was placed directly on-axis and was connected directly to the inner cable of a 50-ohm coax.

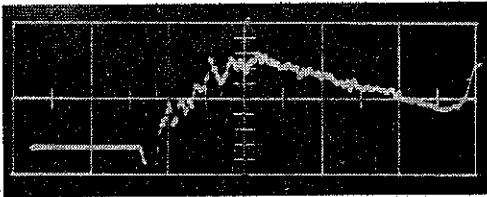
Typical ion current traces are shown in Figure 35. The second screen appears to be detecting electrons scattered out of the first screen and arriving just ahead of the ion pulse. This would explain the altered shape of the ion waveform produced by the second screen. A calculation of the maximum energy imparted to an electron from a proton or heavy ion with the observed velocity is consistent with the time of arrival of the precursor negative dip in the signal from that screen. The time of flight pipe terminated in a copper disk Faraday cup 10.3 cm beyond the second screen.

C. RESULTS AND COMMENTS

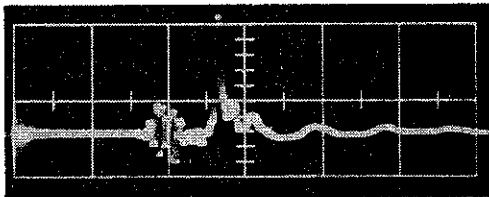
A list of shots with time-of-flight information and equivalent ion energies is presented in Table VI. The β 's given are at the leading edge of the pulse and are typically 0.11. The pulse peak generally has a β of 0.089, and the pulses contain about 10^{11} - 10^{12} particles. One of several aspects of our data suggesting further investigation is the multiple bunching of ion pulses. Figure 35 shows two ion current pulses detected by the screens and by the Faraday cup, indicating as many as five ion bunches. The waveforms obtained with the screens differ from those monitored with the Faraday cup; this difference remains unexplained. The bunches observed here have successively smaller momenta. Modulation of the electron beam current with sharp dI/dt pulses (Figure 33) suggests a possible correlation between the observed electron and ion beam structures.



(a) Screen 1
 Signals for
 a 200 μ Helium
 Shot, 0.93 A/cm



(b) Screen 2
 Signals for
 a 200 μ Helium
 Shot, 0.93 A/cm



(c) Faraday Cup
 Signal from a
 145 μ Air Shot,
 6.3 A/cm

FIGURE 35. POSITIVE ION CURRENT WAVEFORMS (All Traces are 20 nsec/cm.)

TABLE VI
MEASURED ION ENERGIES

Shot	Gas	Pressure (Microns)	β_{Max} for First Pulse (V/C)	E_{Max} Gas Ions (MeV)	E_{Max} Protons (MeV)
11806	Air	50	0.106 ± 0.008	78.8	5.40
11808	Air	150	0.107 ± 0.008	80.0	5.45
11809	Air	150	0.114 ± 0.008	91.8	6.20
11810	He	180	0.122 ± 0.008	28.1	7.95
11811	He	180	0.118 ± 0.008	26.5	6.75

Assuming that (1) ion acceleration takes place over a short distance, at a distance X_0 from the first screen, and (2) the ions travel unaccelerated to the screen at the measured β , then we can use the measured β 's of the first and second pulses (β_1 and β_2) and their separation in time of arrival at screen one, d , to calculate X_0 :

$$X_0 = (d - \Delta) \left(\frac{\beta_1 \beta_2}{\beta_1 - \beta_2} \right) c$$

where Δ is an appropriate separation time at the anode. If one assumes that Δ is the separation in dI/dt peaks (electron beam modulations) at the diode, then X_0 is 80 ± 8 cm for screen one.

A similar calculation for screen two yields 110 ± 9 cm. The actual distances of screen one and two from the anode window are 82.5 and 112.5 cm, respectively. Apparently the observed acceleration is related to beam entry into the gas-filled region and not to some acceleration effect dependent upon propagation through the gas region. Further, since the β for ions in helium is essentially the same as in nitrogen (similar to the data of Graybill and Uglum) an unlikely stripping of ions to the same Z/m ratio would be required.

A more reasonable explanation is that the ions are in fact protons, and that the acceleration process locally selects particles with the highest value of Z/m . Unfortunately, no measurement exists which indicates the ion type, except for the range measurements indicating protons in connection with the hydrogen shots of Graybill and Uglum.

Let us review the following: (a) the ion acceleration process appears to occur near the anode, (b) there is as yet no evidence for ion type, (c) there appears to be no strong dependence on electron beam current as suggested by Graybill and Uglum; particle β 's of 0.10 to 0.12 were obtained by us at 600 keV and 160 kA and by Graybill and Uglum at 1.3 MeV and 40 kA. Future experiments should be directed toward ion identification and momentum resolution, preferably time-resolved, and toward developing an understanding of the acceleration process.

SECTION V

MULTIPLE CATHODE FEASIBILITY STUDY

Until now multiple cathode techniques have received only a limited amount of experimental study. Impetus for such work at Physics International stems from our requirements to provide relatively low fluences over large areas for certain applications. Another possible development would be the ability to carry out many material response experiments on one machine pulse. The results of brief, internally funded experiments are presented here for their broader implications to high v/γ diode applications.

It has been impossible to achieve low, but uniform, fluences over large areas due to beam pinching in high v/γ diodes and generation of large transverse energy components. An obvious solution is to prevent pinch in the diode and to generate a large diffuse beam at the anode. Of several techniques suggested by C. Martin and D. Forster of the AWRE, Reference 21, one of the most promising appears to be the use of multiple cathodes.

An explanation of requirements for threshold of pinch formation will be given before discussing the specifics of the geometry used in these experiments. This is derived from a qualitative argument by Friedlander, Hechtel and Jory (Reference 22) and confirmed experimentally by J. J. Clark et al Reference 23. The critical current above which diode pinch is predicted is given by

$$I_{\text{critical}} \text{ (Amps)} = 8500 \beta \gamma r/d,$$

where r is the cathode radius and d is the anode-cathode distance.

On the other hand, the average diode current is given by

$$\langle I \rangle \approx \frac{\langle V \rangle}{K}^{3/2} r^2/d^2$$

with K varying during a pulse but having an average value fairly insensitive to diode geometry. If one chooses an electron energy of 400 Kev, to avoid pinch r/d must be less than 2.5 and the average current less than 32 kA, a severe restriction. If, however, we use several individual cathodes, each magnetically isolated from the others, and each carrying less than the critical current, then no such limit on the total current would exist. Questions to be answered then are: (1) Can several cathodes be used in one diode structure with sufficiently reproducible emission from each cathode to equally subdivide the machine current, and (2) can effective magnetic isolation be accomplished using metallic partitions between the cathodes?

The cathode configuration used (Figure 36) has separate circular partitions extending from the anode plane to within 2 cm of the cathode holder. Figure 37 shows the cathode and anode holder arrangement as seen from the drift chamber.

The experiments consisted of measuring the separate cathode output in carbon calorimeters placed adjacent to the anode, allowing the seven beams to drift freely in the drift chamber, and propagating each of the beams in separate guide pipes to the target area.

The shots were performed at a mean electron energy of ≈ 700 keV with 2-cm-diameter individual cathodes held 1 cm from the anode. There was no observation of any tendency for multiple beam interaction in

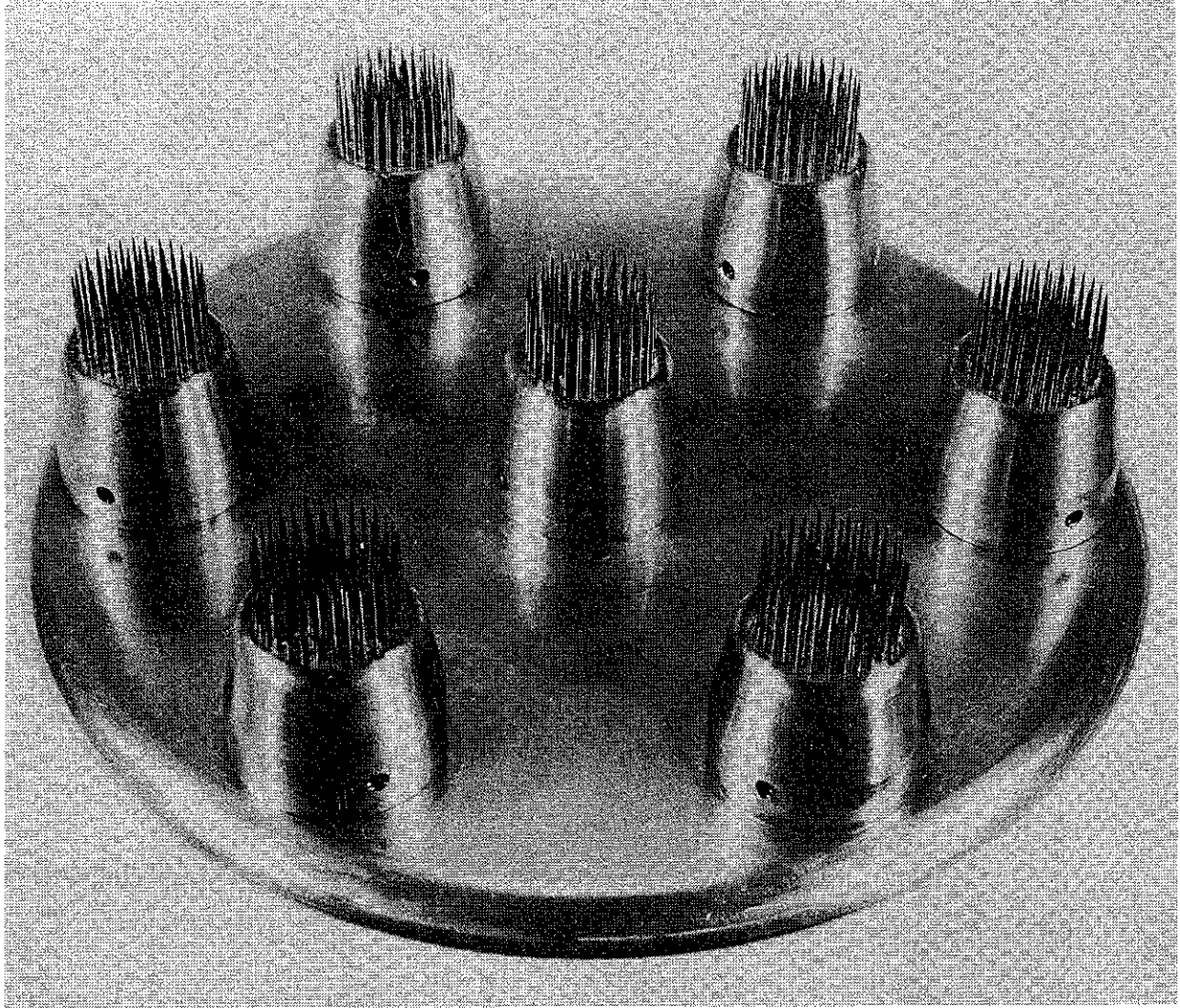


FIGURE 36. MULTIPLE CATHODE CONFIGURATION

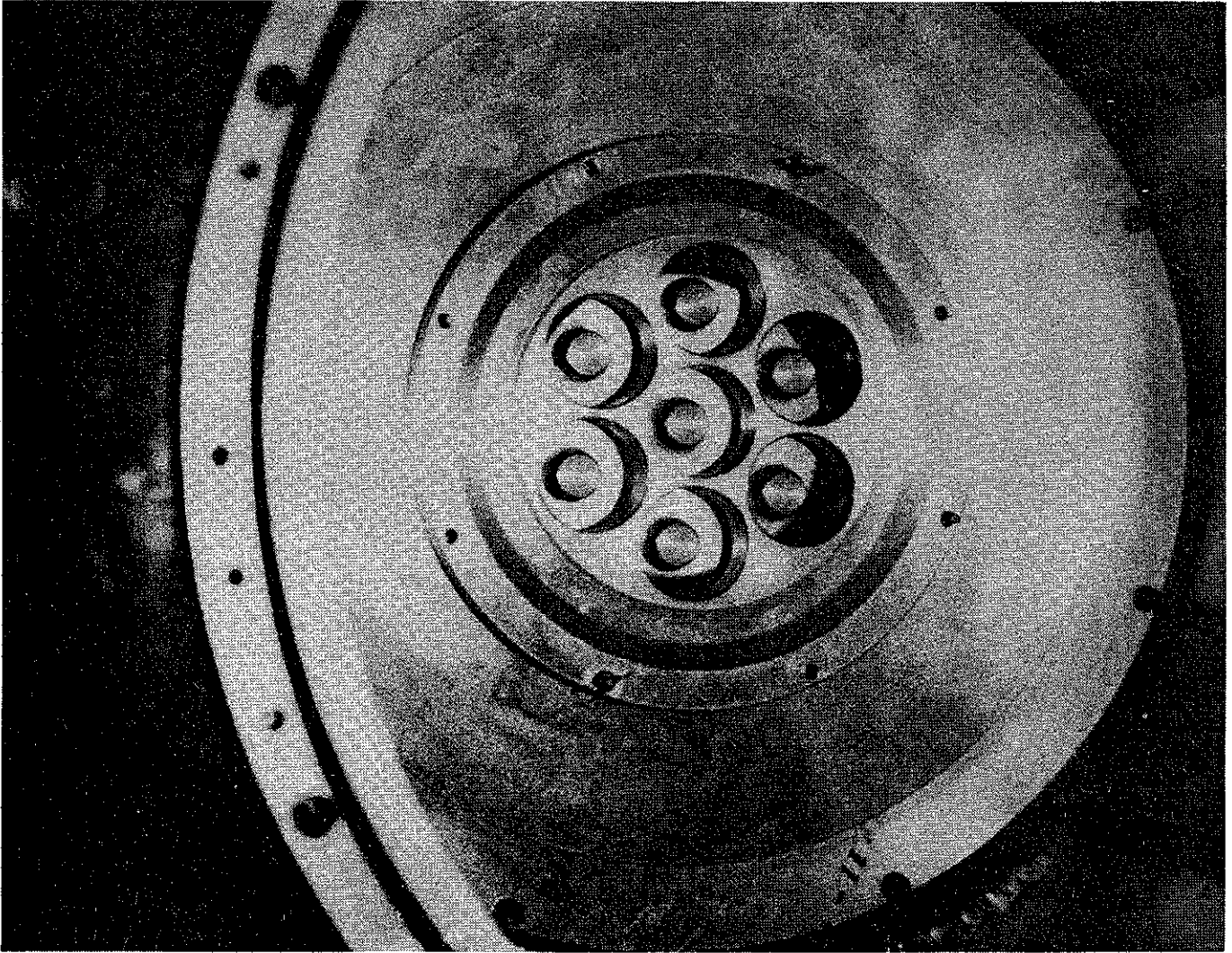


FIGURE 37. MULTIPLE CATHODES AND ANODE HOLDER WITH
MAGNETIC ISOLATION

the diode. The anode was stretched over the separate partitions, (Figure 38) and each beam spot was located centrally within its partition. The calorimetry data showed that total beam energies from each of the cathodes to be equal within a $\pm 10\%$ range. In addition, the consistent trend from the high to low current cathodes may have resulted from slight variations in the individual anode-cathode gaps. Despite the brevity of this work, it demonstrated conclusively that multiple cathodes and magnetic isolation can be used to generate several (in this case seven) beams of correspondingly lower currents.

The implications and applications of this work are discussed further in the next section. It would be desirable to transport each individual beam and to combine them in a suitable manner at the target area. Use of separate beam guides or transport of the multiple beams in one guide are suggested. Figure 39 shows the effect of magnetic attraction of the seven beams injected into the drift chamber without individual guide pipes. The resulting combination of the beams ~ 20 cm from the anode was characterized by a rapid subsequent divergence of the beam electrons in a non-uniform pattern. The degree of power concentration or beam mixing at the focus was not determined nor has the question of beam combination been answered. Successful transport of each beam in a separate conducting guide was demonstrated and this suggests further development of this diode configuration.



FIGURE 38. ANODE USED WITH MULTIPLE CATHODES

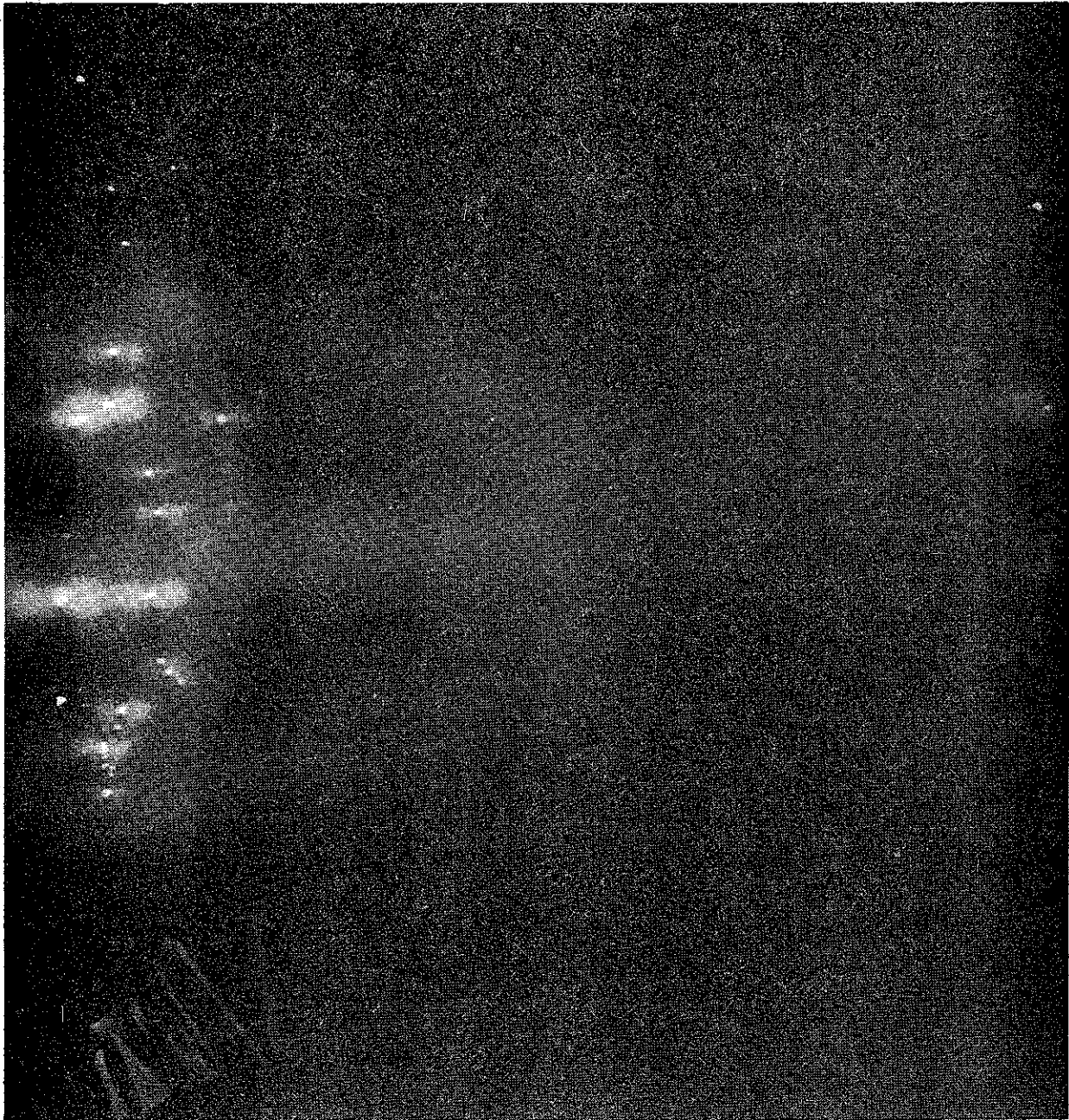


FIGURE 39. OPEN-SHUTTER PHOTOGRAPH OF SEVEN CONVERGING BEAMS

SECTION VI

CONCLUSION

Under the present DASA contract, high v/γ beam diagnosis and control has been improved considerably. The utility of high v/γ beams has been demonstrated amply and the precision of our knowledge of the beam parameters enhanced. We have not succeeded in providing a capability of efficiently transporting high v/γ beams over several meters (losses are observed to reduce (v/γ) primary to a value ≤ 1 after several meters even at the optimum transport gas pressure), but we have, however, investigated mechanisms contributing to transport losses and have suggested techniques to achieve the stated goal. Such a capability will be applied to the eventual development of ultra high v/γ pulsers, responding to the desirability of a modular approach to pulsers, producing and transporting many separate synchronized beams to be combined at the target region.

Discussing these features in view of this report, we note first that there are always intrinsic restrictions on the minimum inductance possible in tube design; a few nanohenries appears to be a reasonable lower limit. Diode impedance would have to be at least a few tenths of an ohm to keep the current rise time ($\tau = L/R$) acceptably small, providing a severe restriction on the currents obtainable from a sub-MeV pulser. Multiple modules eliminate this restriction, since L/R for each module are within workable limits.

Even if current risetime were not a problem, a practical limit to the minimum diode impedance exists. Since the impedance is proportional to $(d/r)^2$ a low-impedance diode must have a large radius, r , and/or a small anode cathode-anode spacing, d . Large-diameter cathodes suffer from alignment problems and necessitate using large area thin anodes which can bow from the pressure differential

between the diode and drift chamber. Small cathode anode gaps are undesirable because shorting of the diode early in the beam pulse is caused by the plasma created in the diode. Secondly, we have shown that two important loss mechanisms are related to the absolute magnitude of the current generated in a particular diode and transported in a beam. Erosion of the beam front over long transport lengths was demonstrated. This occurred because both space charge and inductive fields at the beam front increased as the beam current increased. Creation of transverse energy components in the diode, presumably the fraction of transverse energy increasing with (v/γ) diode, was also mentioned. Since containment of the transverse energy requires large magnetic fields (large net currents) in the drift region we see that the requirements for transport conflict. To contain the transverse energy components a small degree of current neutralization is required, but this results in large beam front erosion losses. An obvious solution is minimizing the transverse energy by using many low v/γ diodes, or even further, subdividing these diodes with multiple, magnetically isolated cathodes, then preventing beam front erosion by pre-ionization. Another possible technique utilizes trapped magnetic fields in a pre-ionized plasma, achievable with a linear pinch, to contain the injected transverse energy of a beam which is itself current neutralized. This particular scheme would also be improved by minimizing the transverse energy components of the beam, again suggesting multiple beams. Future work should investigate the use of pre-ionization, and the effects of magnetic guide fields trapped in the plasma.

Minimal work on the final question of beam combining, using beam splitting and combining in conducting pipes, indicates that this process will not be easy. One might argue that the regions near the beam fronts which are not space charge neutralized will repel each

other, and that the magnetic fields of space charge neutralized portions will be trapped in the plasma, preventing the required flux re-linking. Although this seems likely, further experimentation must verify it. Here pre-ionization should be particularly useful in providing for rapid space charge and current neutralization. Trapped fields could also be used to concentrate several transported beams. Our conclusion is that minimization of beam transverse energy through multiple diode or even multiple cathode developments, and pre-ionization of the beam channel and possible use of trapped fields, will be required to accomplish the development of ultra-high current pulsers.

Another important conclusion is that sizable transverse energy components exist in these beams and must be accounted for in their utilization to material response experiments. Only by including the effect of non-normal incidence in energy deposition calculations, have we been able to achieve agreement between our predictions and measurements.

The conclusions of Graybill and Uglum (Reference 17) that beams can be used to produce energetic ions were confirmed, but we have no evidence as yet concerning the nature of the ions. Further knowledge of this process might improve understanding of the complex process occurring near the beam front and perhaps would lead to applications in other areas of physics. Such a conclusion awaits further efforts.

Much still needs to be learned about high v/γ beams. The effects of finite boundary conditions, precursor radiation, and the details of the radial distribution of currents in pipes and cones, are still only partially understood. Nevertheless, sufficient physical

phenomena are now understood to allow extrapolation concerning the requirements for future machines. The actual evolution of these machines and the development of the suggested techniques will provide effective tests of these ideas.

REFERENCES

1. G. Yonas and P. Spence, "Experimental Investigation of High v/γ Electron Beam Transport", DASA 2175 (October, 1968).
2. G. Yonas, P. Spence, D. Pellinen, B. Ecker, and S. Heurlin, "Dynamic Effects of High v/γ Beam Plasma Interactions", DASA 2296 (April, 1969).
3. J. Creedon, "Pressure Dependence of the Pinched Electron Beam Mode", PIIR-16-67, Physics International Co., San Leandro, Calif. (March, 1967).
4. H. F. Rugge, L. Behrmann, W. T. Link, G. R. Murray, and S. A. Zwick, "Electron Beam Investigations", BSD-TR-67-102 (SFRD) (1967).
5. J. D. Lawson, "Perveance and the Bennett Pinch Relation in Partially Neutralized Electron Beams", J. Electron 5, 146 (1958).
6. N. Rostoker, "Relativistic Beam Theory", DASIAC Special Report 80, 23 (September, 1968).
7. S. Putnam, "Experimental and Theoretical Electron Beam Research", PIQR-105-3, Physics International Co., San Leandro, Calif. (February, 1969).
8. S. Putnam, PIQR-105-4, Physics International Co., San Leandro, Calif. (to be published).
9. P. Felsenthal and J. M. Proud, "Nanosecond-Pulse Breakdown in Gases", Phys. Rev. 139, A1796 (September, 1965).
10. S. Putnam, Physics International Co., San Leandro, Calif. (private communication).
11. J. D. Lawson, "On the Classification of Electron Streams", J. Nucl. Energy, Part C: Plasma Physics 1, 31-35 (1959).
12. R. F. Post, "Controlled Fusion Research", Rev. Mod. Phys. 28, 338 (1956).
13. L. Spitzer, Jr., Physics of Fully Ionized Gases (Interscience Publishers, Inc., N. Y., 1956), p. 42.
14. P. Spence, G. Yonas, and J. Case, "Electron Beam Tests of Several Materials Using Quartz Pressure Transducers", (PIFR-153, Physics International Co., San Leandro, Calif. (May, 1969).
15. P. Spence, G. Yonas, and A. Lutze, "Generation, Control and Diagnosis of High Energy Density Electron Beams", PITR-205-1 Oct. 1969.

16. M. Berger and S. Seltzer, "Tables of Energy Losses and Ranges of Electrons and Positrons", NASA SP-3012.
17. S. E. Graybill, J. R. Uglum, "Observation of Energetic Ions from a Beam-Generated Plasma", Ion Physics Corp. Report, 903 TR-355 (1969).
18. V. I. Veksler, *Atomnaya Energiya* 2, 247 (1957).
19. V. I. Veksler, V. P. Sarantsev, A. G. Bonch-Osmolovsky, G. V. Dolbilov, G. A. Ivanov, I. N. Ivanov, M. L. Iovnovitch, I. V. Kozhukhov, S. B. Kusnetsov, V. G. Makhan'kov, E. A. Perel'shtein, V. P. Rashevsky, K. A. Reshetnikova, N. B. Rubin, S. B. Rubin, P. I. Ryl'tsev, O. I. Yarkovoi, "Collective Linear Acceleration of Ions", Proceedings of the Sixth International Conference on High Energy Accelerators, Cambridge Electron Accelerator CEAL-2000, p. 289 (1967).
20. A. A. Plyutto, P. E. Belensov, E. D. Karop, G. P. Mkheidze, V. N. Ryzhlov, K. V. Suldaze, S. M. Temehin, "Acceleration of Ions in Electron Beams", *JETP Letters* 6, 61 (1967).
21. C. Martin and D. Forster, "Control of Energy Deposition over Large Area Samples", SSWA/DWF/6812/108, AWRE (January 1969).
22. F. Friedlander, R. Hechtel, and H. Jory, "Megavolt-Megampere Electron Gun Study", Varian Associates, Palo Alto, Calif. (1968).
23. J. J. Clark, M. Ury, M. G. Andrew, D. A. Hammer, and S. Linke, "High Current Relativistic Electron Beam Accelerators at Cornell University", 10th Symposium on Electron, Ion, and Laser Beam Technology, May 21-23, 1969, NBS, Gaithersburg, Maryland.